STUDIES ON FILM COOLING IN ROCKET COMBUSTION CHAMBERS

A thesis submitted
in partial fulfillment for the degree of

Doctor of Philosophy

by

SHINE S. R.

Department of Aerospace Engineering

INDIAN INSTITUTE OF SPACE SCIENCE AND TECHNOLOGY

Thiruvananthapuram - 695547

April 2013

CERTIFICATE

This is to certify that the thesis titled **STUDIES ON FILM COOLING IN ROCKET COMBUSTION CHAMBERS**, submitted by **Mr. Shine S. R.**, to the Indian Institute of Space Science and Technology, Thiruvananthapuram, for the award of the degree of **Doctor of Philosophy**, is a bona fide record of the research work done by him under our supervision. The contents of this thesis, in full or in parts, have not been submitted to any other Institute or University for the award of any degree or diploma.

Dr. B. N. Suresh
Supervisor
Former director, IIST

Dr. S. Sunil Kumar,
Co-Supervisor
Head, Thermal Engineering Division, LPSC

Place: Thiruvananthapuram
Date: April 2013

DECLARATION

I declare that this thesis titled **STUDIES ON FILM COOLING IN ROCKET COMBUSTION CHAMBERS** submitted in fulfillment of the Degree of Doctor of Philosophy is a record of original work carried out by me under the supervision of **Dr. B. N. Suresh and Dr. S. Sunil Kumar**, and has not formed the basis for the award of any degree, diploma, associateship, fellowship or other titles in this or any other Institution or University of higher learning. In keeping with the ethical practice in reporting scientific information, due acknowledgments have been made wherever the findings of others have been cited.

Shine S R

SC09D002

Place: Thiruvananthapuram

Date: April 2013

ACKNOWLEDGEMENTS

Completion of this dissertation would not have been possible for me without the guidance and help from my advisors, colleagues, friends and family and I would like to thank all of them here.

My grateful appreciation goes to my research advisor Dr. S. Sunil Kumar for his encouragement during the tough times, insightful arguments during the easy times and important lessons all the time. For all this and much else besides, I am grateful to him.

Dr. B. N. Suresh had kick-started my work in the early days and I am grateful for his vision and advice. His continuing guidance and support throughout this research work is greatly appreciated.

I am grateful to Shri. N. K. Gupta, Prof. Satish Dhawan Professor at LPSC for his helpful comments and guidance in my work.

I also acknowledge the multitude of discussions I had with Prof. Kurien Issac, Head, Department of Aerospace Engineering, which were invaluable to me.

I want to thank Prof. A. Salih, for his helpful comments and guidance in my work. He also created and made available a thesis style file to be used in conjunction with LaTeX and made my job easier. It is an honour to have him as a colleague.

My friends and colleagues at the Indian Institute of Space and Technology deserve my heartiest appreciation and thanks for their encouragement and support, both in the institute and outside it. I am proud and happy to have been surrounded by such intellectually stimulating and fun loving people all through these years. Our daily academic and social conversations over tea were the highlight of many a frustrating day! I would like to acknowledge especially Dr. S. Anup, Dr. M. Deepu, Dr. V. Aravind and Prof. Sam Zachariah for their continuous encouragement and laughter in the most tense of times. I would also like to thank Shri. Jophy Peter of LPSC for his assistance with the instrumentation in the test rigs.

Last, but not the least, I have many thanks to my family. In particular, I thank my wife, Reshmi, for her incredible support and love. I would like to express my appreciation to my son Navaneeth and my daughter Nanditha, who relinquished untold amount of time with their father. Finally, I wish to thank my parents for all their support and blessings which have made me what I am today.

Shine S. R.

ABSTRACT

Film cooling is applied extensively to surfaces that are exposed to hot combustion gases. A review of literature revealed that studies on film cooling process have concentrated mainly on film cooling applied to gas turbine airfoils. In this study, an extensive program of work has been undertaken to understand the gaseous and liquid film cooling process applicable to rocket combustion chambers. The film cooling performance of various gaseous and liquid coolant injector configurations are investigated experimentally. Measurements using coolant injector orifices of straight and compound angles in two orientations are obtained for the gaseous coolant. Tangential and compound angle orientations are examined for the liquid coolant. The data is analysed based on film cooling effectiveness and film uniformity calculations at different blowing ratios. Beyond the fundamental importance of these analyses, the gaseous film cooling data sets are used to validate computational models developed using CFD. The computational models are used to document all of the pertinent flow physics and heat transfer characteristics associated with the film cooling flow field.

Experimental results showed that in case of gaseous coolant injection, compound angle holes produced better film cooling performance compared to straight holes. However, increasing tangential angle of the compound injector did not improve the performance and in-fact led to a rise in wall temperature. It is observed from the numerical simulations that at higher tangential angles, better distribution of coolant around the circumference is offset by the increased heat transfer coefficients created by the secondary flow structures downstream of injection. A local maximum value for Nusselt number is observed in the regions where the flow reversal occurs. Conjugate wall cooling simulation with highly conductive walls showed reversed heat transfer from the surface to the gas in the nearby injection regimes. The analysis shows that highly conductive wall is not a proper choice for film cooling applications. In case of liquid film injection, compound angle holes produced higher performance only in the neighbourhood of injection.

A thorough analysis of the liquid film cooling process is carried out in the present work incorporating all associated phenomenon as is currently understood. The interfacial mass and energy balance is discussed in detail, together with the phenomenon of coolant transpiration, free-stream turbulence, film instability and the entrainment of the liquid by the gas stream. The limitations of the existing analyses are noted, and a new correlation procedure is suggested that is applicable to rocket combustion chambers operating at subcritical conditions. The results of this study show that the effect of coolant entrainment is significant. Therefore a numerical model is developed

to investigate the liquid-gas interface characteristics and the associated entrainment mechanisms. Simulation results indicate that the disturbance waves are present at the liquid-gas interface for coolant flows above a critical value and these waves are formed after a finite distance from the inlet. The distance toward the wave inception point increased with the increase of momentum flux ratio. The coolant film thickness and the disturbance wave characteristics are not much affected by the changes in pipe diameter. Analysis indicates that the disturbance are dynamic, continuously growing and eventually the wave crests are sheared off by the incoming gas phase causing entrainment. It is also observed that the turbulent flow features in the gas core have strong effects on the interfacial waves.

Together, the results of this study have enhanced the understanding of the film cooling process applicable to rocket combustion chambers and have laid the groundwork for higher effective film coolant injector orientations.

TABLE OF CONTENTS

LIST OF TABLES

LIST OF FIGURES

ABBREVIATIONS

AW	Adiabatic Wall
CFD	Computational Fluid Dynamics
EDM	Electrical Discharge Machining
MFR	Mass Flow Ratio of Liquid Coolant to Mainstream Gas
RNG	Renormalization Group
SSME	Space Shuttle Main Engine
TEG	Turbine Exhaust Gas
TR	Ratio of Coolant Temperature to Core Gas Temperature
VOF	Volume of Fluid

NOTATION

A	Area of crossection, m^2
c	Specific heat, $J\ kg^{-1}\ K^{-1}$
c_p	Constant pressure specific heat, $J\ kg^{-1}\ K^{-1}$
c_v	Constant volume specific heat, $J\ kg^{-1}\ K^{-1}$
D	Film cooling test section inside diameter, *mm*
D_1	Approach section inside diameter, *mm*
d	Coolant hole diameter, *mm*
E	Entrainment fraction, dimensionless
E_m	Maximum entrainment fraction, dimensionless
f	Fanning friction factor, dimensionless
$\dot{G}$	Mass flux rate, $kg\ m^{-2}\ s^{-1}$
H	Step height, $(D - D_1)/2$, mm
h	Heat transfer coefficient, $W\ m^{-2}\ K^{-1}$
h_{fg}	Enthalpy of vaporization, $J\ kg^{-1}$
I	Momentum flux ratio between the coolant and mainstream, $V_c^2\rho_c/V_g^2\rho_g$
KE	Kinetic energy, *W*
k	Thermal conductivity, $W\ m^{-1}\ K^{-1}$
L_c	Liquid film cooled length, *m*
$\mathcal{M}$	Molecular weight, *kg*
M	Blowing ratio/Mass flux ratio between the coolant and mainstream, $V_c\rho_c/V_g\rho_g$
$\dot{m}$	Mass flow rate, $kg\ s^{-1}$
$\dot{m}_{film}$	Film evaporation per area, $kg\ m^{-2}\ s^{-1}$
Nu	Nusselt number
P	Pressure, $N\ m^{-2}$
P_e	Perimeter, m

Pr	Prandtl number
$\dot{Q}$	Heat transfer rate, *W*
q	Heat flux, $W\,m^{-2}$
R	Radius of combustion chamber, *m*
Re	Reynolds number
r	Distance in the radial direction, *m*
St	Schmidt number
St	Stanton number
s_e	Equivalent slot width, *m*
T	Temperature, *K*
Tu	Turbulence intensity, percentage
t	Time, *s*
u	Velocity in the axial direction, $m\ s^{-1}$
V	Average velocity, $m\ s^{-1}$
v	Velocity in the radial direction, $m\ s^{-1}$
x	Axial distance from the coolant injection point, *m*
We	Weber number
w	Injection slot width, mm
w_l	Distance toward the wave inception point
x	Axial distance measured from the coolant injection point, *mm*
δ	Thickness of coolant film, *mm*
Φ	Enthalpy of stream, *W*
ϕ	Film cooling effectiveness based on inside surface temperature of the test section
β	Included angle between two coolant holes,$^\circ$
γ	azimuthal angle, $^\circ$
η	Film cooling effectiveness based on outside surface temperature of the test section
η_{exp}	Experimental film cooling effectiveness based on outside surface temperature of the test section
η_{comp}	Computational film cooling effectiveness based on outside surface temperature of the test section

$\overline{\overline{\eta}}$	Spatially averaged effectiveness
λ	Darcy friction factor
μ	Dynamic viscosity, $kg\ m^{-1}\ s^{-1}$
μ_t	Turbulent viscosity
ρ	Density, $kg\ m^{-3}$
σ	Surface tension, $N\ m^{-1}$
τ	Shear stress, $N\ m^{-2}$
ψ	tangential angle, $^\circ$

Subscripts

c	Coolant
conj	Conjugate
conv	Convective
f	Film
g	Hot gas flow
i	Liquid-vapour interface
inj	Injection
int	Solid-liquid interface
l	Liquid
m	Mixture
o	Dry wall condition
out	Outside surface
rad	Radiative
sat	Saturated
tot	Total
v	Vapour
w	Wall
wave	Wave

Over scores

.	Per unit time

CHAPTER 1

INTRODUCTION

1.1 Background and Motivation

Rocket engines used for space missions encompass a wide spectrum of performance and structural requirements. Thrust levels may vary from a few newtons to many thousands of newtons, with burning time from fraction of a second to hours. In all these engines, the energy released by the propellants must be contained inside the thrust chamber and accelerated through the nozzle to extract the thrust. The thrust chamber and the adjacent ducts must be protected from the enormous heat that is being released in the thrust chamber. The basic thermal design requirements are low equilibrium wall temperature, zero or minimum erosion in the combustion chamber and minimum soak back temperature to nearby components.

Thrust chamber cooling methods developed to meet these requirements either separately or in combination include regenerative cooling, film cooling, transpiration cooling, ablative cooling, radiation cooling, heat sink cooling and dump cooling. Regenerative cooling is accomplished by flowing high-velocity coolant through channels along the hot chamber wall to convectively cool the hot thrust chamber. The coolant with the heat input from the hot thrust chamber is then discharged into the injector and utilized as a propellant. Film cooling provides protection from excessive heat by introducing a thin film of coolant through orifices around the injector periphery or in the chamber wall near the injector or chamber throat region. Transpiration cooling, which is considered a special case of film cooling provides gaseous or liquid coolant through the porous chamber liner wall at a rate sufficient to maintain the chamber hot gas wall to the desired temperature. With ablative cooling, combustion gas-side wall material is successively sacrificed by melting, vaporization and chemical changes to dissipate heat. A radiation cooled chamber transmits the heat from its outer surface, chamber or nozzle extension. In heat sink cooling method, endothermic materials and

metals capable of absorbing large amounts of heat through phase change process, are impregnated into porous refractory wall materials or used to back up the walls as an insulator as well as a heat sink. In dump cooling, the coolant is poured through cooling channels inside the liner material and is dumped overboard at the end of the nozzle skirt through sonic outlets, or is injected into the nozzle at a specific expansion ratio and used as a film coolant for the downstream part of the nozzle section. Coulbert (1964) has shown that cooling methods such as radiation, ablative and heat sink are efficient when applied to low thrust and short run chambers (Fig. 1.1). Huzel and Hwang (1992) and Arnold et al. (2010) have compared different cooling systems for short and long duration liquid rocket engines and observed that (i) ablative cooling and heat sink methods are used for short duration systems with a limited operating time of about two minutes, and (ii) low heat flux areas of liquid rocket engines such as nozzle extensions are cooled by radiation cooling method.

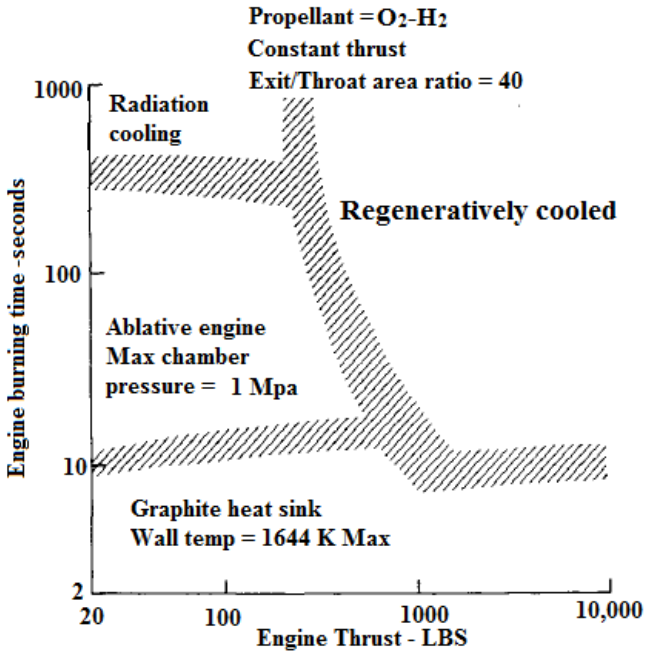

Figure 1.1: Thrust vs. burning time envelopes for minimum weight space engines- Reproduced from Coulbert (1964)

Present rocket engines are subjected to hot-gas temperatures of the order of 3500 K with combustion-chamber pressures exceeding 18 MPa such as in the SSME, (19 MPa) or in the RD-170 (24.8 MPa) leading to local wall heat flux densities of more

than 100 MW/m^2 which has to be maintained within the allowable temperature limits by the cooling system of the engine. Extremely high heat flux levels and temperature gradients are present not only in the immediate vicinity of the injector head, but also in the region of nozzle throat section. The non-dimensional wall-heat load distribution in the nozzle throat section for a typical LOX/H2 rocket engine with a chamber pressure $\approx$ 12 MPa and a propellant mixture ratio of 7 is calculated by Arnold et al. (2009b) and is shown in Fig. 1.2. It is seen that the maximum heat flux occurs in the close

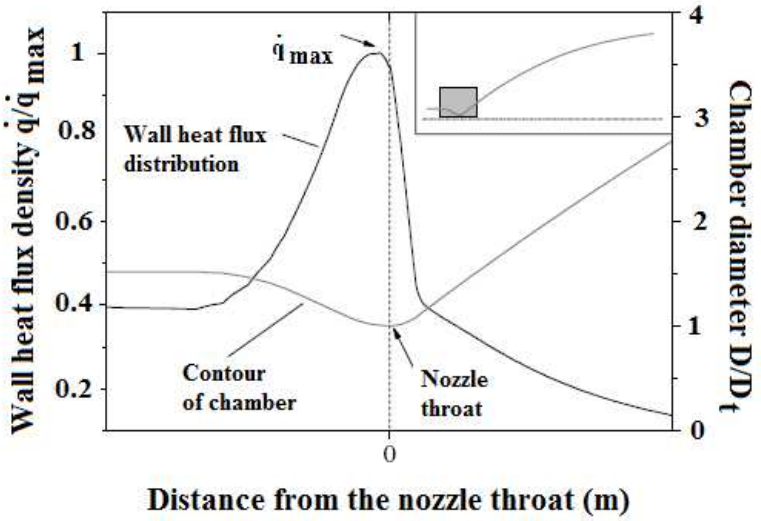

Figure 1.2: Calculated wall heat flux distribution in the nozzle throat section- Reproduced from Arnold et al. (2009b)

proximity to nozzle throat, and an effective cooling of the throat area is crucial for enhanced reliability and lifetime. Regenerative cooling is the standard cooling system for almost all modern main stage, booster, and upper stage engines (Huzel and Hwang, 1992). The best technology for high-pressure engines or expander-cycle engines is regenerative cooling because it does not affect the general performance of the engine. However, it is very demanding in turbopump power. Improvements in regenerative cooling performance could only be accomplished by an increased Reynolds number of the propellant inside the cooling channels. This will give better heat transfer from the wall to the coolant, but turbopumps and turbines are heavily loaded because of the pressure drop in cooling channels, which results in limitations of engine lifetime, reliability, and safety margins. Cooling channel geometry design has to account for the

thermal blockage caused by the high heat fluxes and the comparatively drastic change in the fluid properties such as heat capacity, density and viscosity at high pressures and temperatures. It is now well established that the regenerative cooling is to be augmented with an additional cooling technique in high heat flux regions for better performance of high thrust combustion chambers.

Different film cooling techniques have been developed in the past to reduce regenerative cooling load and propellant requirements. It is found that all these methods lead to reduced wall temperatures. Currently, engines like SSME, F-1, J-2, RS-27, Vulcain 2, RD-171 and RD-180 use film cooling technique. For gas-generator cycle engines, the turbine exhaust gas (TEG) is used as dump coolant to gain engine performance by using lower dump mass flow. Several existing open-cycle rocket engines have TEG delivered to the nozzle, including the F1 engine (Warren and Langer, 1989) and J2 engine (Vilja et al., 1993) of the United States and the upgraded LE5 engine (Kim, 1991) of Japan. There are no apparent limitations on cooling capability, time, or chamber pressure with film cooling. However, if one of the propellants (usually fuel) or an inert fluid is used as a coolant at the nozzle throat, there is a performance penalty (specific impulse loss). A film of liquid or gas flow through rocket nozzle throat with a temperature different from core gases can result in performance losses (Campbell et al., 1963). Analysis by Coulbert (1964) revealed that a typical performance loss due to film cooling is proportional to the quantity of coolant flow.

Regenerative cooling in combination with film cooling is presently considered as an efficient method to guarantee a safe operation for long duration of engines with higher heat flux densities. This technique is applied in F-1, J-2, RS-27 and Vulcain-2 engines. Schematic of Vulcain 2 engine employed with regenerative cooling augmented by film cooling along the inside wall of a nozzle extension is shown in Fig. 1.3. In Vulcain-2 engine, the combustion chamber wall film cooling has been employed from the injector face plate down to the nozzle throat section. The overall dump cooled nozzle extension used on Vulcain-1 has been replaced by a completely new nozzle design that provides for dump coolant injection at an area ratio of 29.2 and turbine gas film cooling injection at an area ratio of 32. This provides gaseous film cooled nozzle and enables Vulcain-2 to deliver a specific impulse of 429 sec. Presently

film cooling technique is applied to nearly all of the external surfaces associated with the airfoils (Bogard and Thole, 2006). Though, it is employed in all of today's aircraft turbine engines and in many power-generation turbine engines, the underlying phenomenon is complex and hence it is difficult to predict.

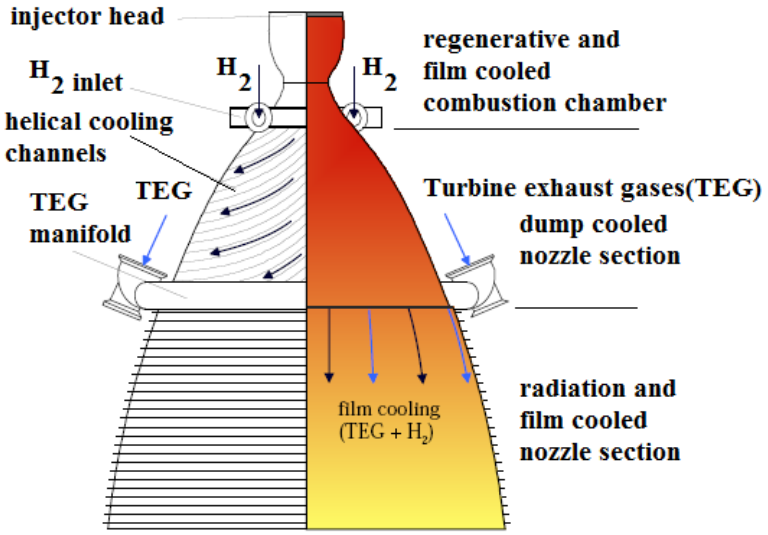

Figure 1.3: Cooling design of combustion chamber and nozzle of Vulcain 2 engine

Film cooling of combustion chambers will play a major role in the development of future highly reusable and booster rocket engines as this technique can increase the chamber life by reducing the thermal stresses. Efficient use of the coolant films is critical because of the associated specific impulse reduction. Among the vast literatures related to film cooling, majority of the work focuses on gaseous film cooling associated with airfoils. These factors have been a major motivation for undertaking this research work. Therefore, the main objective of this work is to conduct a detailed study of the gaseous and liquid film cooling process applicable to rocket combustion chambers. The work focuses on the experimental investigation of the performance of various gaseous and liquid film cooling injector configurations. Another objective is the analytical investigation of the liquid film cooling process to understand the various physical phenomenon involved and to develop a correlation procedure for calculating the liquid film cooled length. Numerical simulations are also envisaged to understand

the behaviour and development of gaseous and liquid films in the near chamber wall environment.

1.2 The Film Cooling Problem

The mechanism by which film cooling produces a lower combustor wall temperature is considerably different from that of convective cooling. Film cooling is accomplished by interposing a layer of coolant fluid between the surface to be protected and the hot gas stream. The fluid is introduced directly into the combustion chamber through slots or holes and is directed along the walls (Fig.1.4). A typical temperature distribution from the hot combustion gases to the exterior of the chamber wall in a film cooled combustion chamber is shown in Fig. 1.5. It can be observed that the coolant film does have a thermal insulation effect and reduces the chamber wall temperature. Coolant film may be generated by injecting liquid fuel or oxidizer through wall slots or holes in the combustion chamber, or through the propellant injector. The cooling effect will persists up to the throat region in the case of a shorter combustion chamber. In a fully film-cooled design, injection points are located at incremental distances along the wall length. In liquid film cooling, the vaporized film coolant does not diffuse rapidly into the main gas stream but persists as a protective mass of vapor adjacent to the wall for an appreciable distance downstream from the terminus of the liquid film. The film coolant also forms a protective film which restricts the transport of the combustion products to the wall, thus reducing the rate of oxidation of the walls. It is observed that the film cooling thermal performance characteristics vary widely, depending upon the type of coolant being used (Morrell, 1951; Warner and Emmons, 1964). Coolant sources are usually pressure fed fuel, oxidizer, water, hydrogen, hydrocarbons or turbine exhaust gases as in the case of gas-generator engines. Hydrogen has low molecular weight and results in low cooling performance losses. Hydrocarbon fuels provide high cooling capacity because of their highly endothermic decomposition, but the performance degradation is also high. In the Vulcain engine, the film is produced using turbine exhaust gases. The exhaust gases are first collected in a torus and then re-injected into the engine nozzle at an appropriate location. This

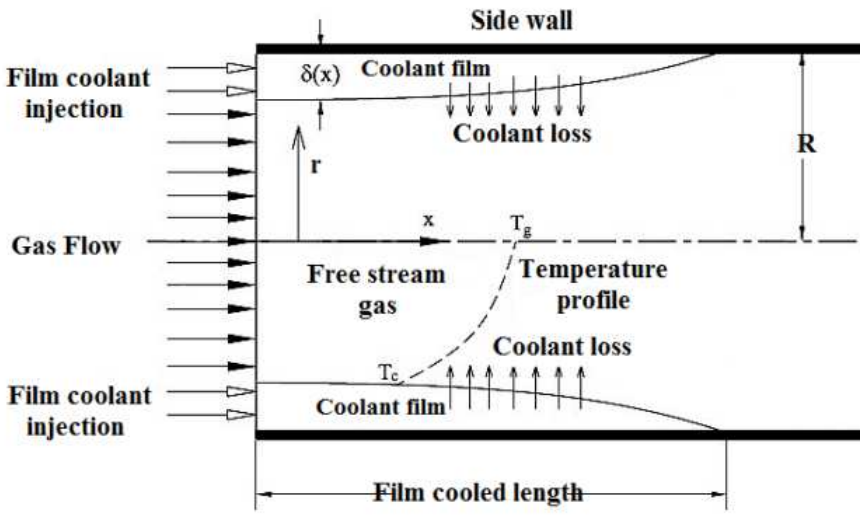

Figure 1.4: Schematic of the physical system

will lower the wall temperature through the gaseous film cooling process.

Film cooling performance is also affected by a number of flow and geometric parameters. Flow parameters that affect film cooling include the ratios of density, velocity, temperature, mass and momentum flux between coolant and mainstream, pressure gradient, free-stream Mach number and free-stream turbulence. Injection geometry parameters include the injection surface curvature, hole exit shape, hole pitch to diameter ratio, and the orientation of hole with respect to the main stream. If the coolant is liquid, the physical characteristics of the gas-liquid interface are very important. Film instability is caused by the disturbance waves at the interface and the annular entrainment of the coolant becomes critical in these environments. Excessive liquid entrainment could lead to complete removal of liquid film from contact with the chamber walls. The radiation heat transfer is also significant due to the high temperature of the combustion products. Added to it is the fact that the multiple jets might be interacting with each other and it is easy to see that a film cooling process is a very complex three-dimensional phenomena.

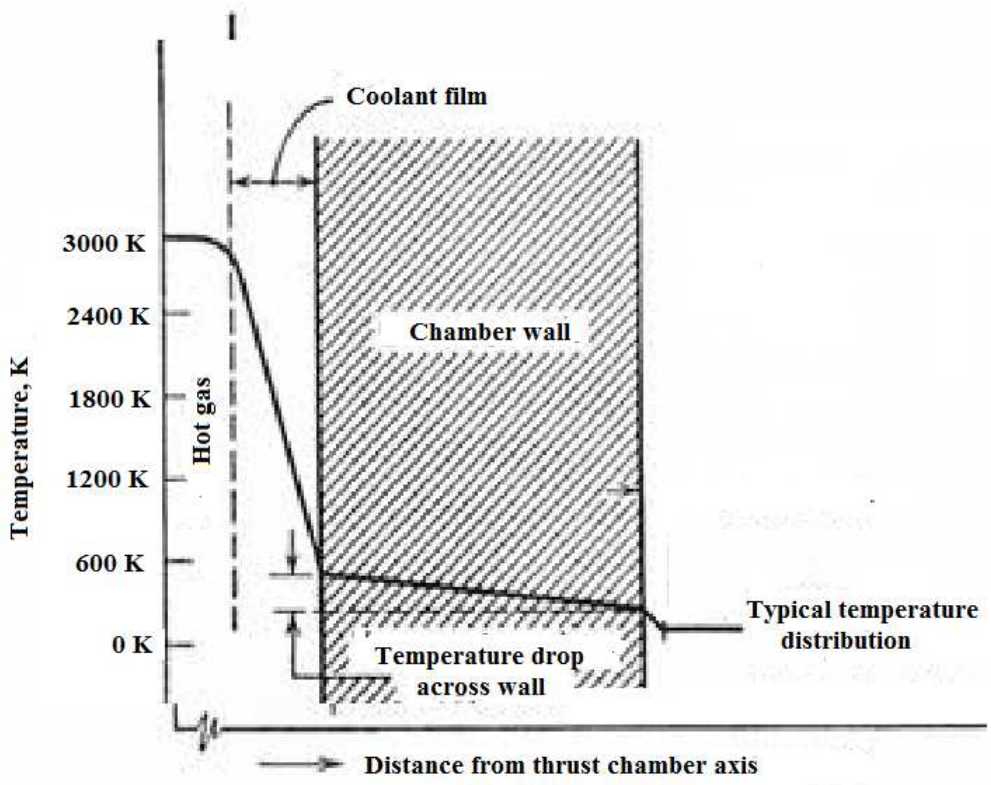

Figure 1.5: Typical temperature distribution of com bustion chamber across wall

1.3 Literature Review

Origin of film cooling studies stretch way back into history of fluid mechanics starting from the days of Reynolds and Lamb of the late 19th century (Reynolds,1876; Lamb,1982). Reynolds (1876) studied the behaviour of vortex rings, a topic closely related to the modelling of film cooling jets. The application of a fluid film for the protection of surfaces in aerospace related field is often attributed to Wieghardt (1944). He applied this technique to de-icing of aircraft wings by blowing warm air over them. Since then, there have been numerous experimental studies and several models have been developed for the prediction of film cooling effectiveness. Most of the work documented about film cooling concentrated on gaseous film cooling with relatively less work documented for liquid film cooling. A chronological literature review of some relevant studies, ranging from gaseous film-cooled to liquid film-cooled configuration is presented below.

1.3.1 Gaseous film cooling studies

Film cooling investigations over the years have concentrated mainly on gaseous film cooling applied to gas turbine airfoils followed by work on film cooling of rocket combustion chambers. Survey of current literature on airfoil film cooling shows extensive studies for coolant holes with various geometries and at various stream-wise injections. Film cooling is applied to nearly all of the external surfaces associated with the airfoils that are exposed to the hot combustion gasses such as the leading edges, main bodies, blade tips, and end walls. Though the processes are similar, the key challenges involved in rocket engine film cooling are different from that of airfoil film cooling. The main differences between the two process includes: (i) extreme heat flux, temperature and pressure conditions present in modern rocket engines, (ii) the presence of highly accelerated flows, (iii) the initial turbulent state of the coolant and core streams, (iv) the use of gaseous and liquid coolants, (v) two phase flow conditions present with liquid film cooling, (vi) surface curvature effects, (vii) the requirement of flow uniformity and wall adherence, (viii) density gradients and compressibility effects (Coolant to core stream density ratios are in the order of two or higher are typical in many engines), (ix) the effect of reactive coolant, (x) radiation effects, and (xi) unsteady flows (Unsteadiness in the core flow of a rocket engine can arise from various sources including turbulent flow in the feed lines, fluttering of pump wheel blades, vibrations of control valves, and unsteady motions in the combustion chamber and gas generator). Moreover, the film cooled length is an important parameter in the design of rocket combustion chambers. It is also to be noted that in rocket engines, film cooling is always applied in combination with other cooling methods (usually regenerative cooling). The following paragraph mainly details the gaseous film cooling studies applicable to rocket combustion chambers.

Gaseous film cooling is considered to have potential use in nuclear rockets, and high-energy liquid chemical rockets. In general, there are limited number of film cooling investigations dealing with gaseous-film cooling, applicable directly to a rocket motor. Among the earliest studies, Lucas and Golladay (1963) investigated the effects of cooling a cylindrical portion of the combustion chamber with both tangential and inward-angled slot coolant injection and cooling the nozzle with tangential injection.

In each configuration nitrogen was used as the coolant and in addition, limited data was also obtained with the cooled nozzle using propane as the coolant. It was concluded that correlations for adiabatic wall film cooling effectiveness can be employed to predict the performance associated with non-reactive, non-condensable gases. The requirement of the reactive coolant was higher than the non-reactive coolant with equivalent transport properties. Marek and Tacina (1975) employed tangential slots to inject coolant air inside a rectangular test section to study the effect of free-stream turbulence levels on film cooling effectiveness. The film cooling effectiveness decreased as much as 50% as the free-stream turbulence intensity was increased from 7 to 35%. Gau et al. (1991) conducted experiments in a film cooled circular pipe with an abrupt expansion of 2.4:1. These experiments demonstrated that the swirl in the mainstream had a significant effect on the film-cooling performance. The role of mainstream flow velocity in a film cooling duct was studied by O'Connor and Haji-Sheikhf (1992) and Kuo et al. (1996). Kuo et al.'s experimental observations revealed film cooling to be effective in subsonic flow, but not in supersonic flow. They observed bending of the injected flow stream towards the upstream direction against the incoming mainstream in the case of supersonic flow. This created a stagnation region and temperature rise in the flow field leading to negligible film cooling effect on downstream wall regions where the supersonic flow was dominant.

Investigations on film cooling on a flat plate with a slot injection in laminar supersonic flows were done by Heufer and Olivier (2008). Experimental and numerical results showed no influence of the blowing parameters on the cooling effects. The cooling effect was found to be influenced by the core gas flow conditions and was reported that the film cooling technique is highly effective under laminar flow conditions. A correlation to predict slot film-cooling efficiency of a wall jet, under conditions of variable turbulence intensity, flow and temperature was developed by Simon (1986). Dellimore et al. (2009) proposed a semi-empirical model for wall-jet film cooling to include the effects of adverse and favorable pressure gradients. The effect of gaseous film injection in duel bell nozzles was numerically studied by Martelli et al. (2009). The injection was made in the first bell through an axisymmetric slot located in the divergent section, and it was found that the expansion fan originating from inflection helps the film to better protect the wall. It was also observed that expansion

Table 1.1: Gaseous film cooling studies applicable to rocket thrust chambers

	Type of injection
Lucas and Golladay (1963)	Tangential, Inward-angled slot injection
Marek and Tacina (1975)	Tangential slots
Gau et al. (1991)	Axisymmetric slots
Kuo et al. (1996)	Slanted hole with a 30-deg inclination
Martelli et al. (2009)	Axisymmetric slots
Arnold et al. (2009b)	Tangential slots

generated by the inflection point lowered the wall recovery temperature and reduced the mixing. This allowed the film to protect the wall for a longer distance. Experiments by Arnold et al. (2009a) showed significant variations of wall temperatures due to injector design and more pronounced circumferential variations in wall temperature at higher combustion chamber pressures. Experiments were conducted in a subscale rocket combustion chamber with tangentially injected film of hydrogen. Tangential slot injection was investigated for various film-cooling parameters in the same experimental set up (Arnold et al., 2010). A modified film-cooling model for application in a combined convective and film-cooled combustion chamber with an accelerated hot gas was developed by Arnold et al. (2009b). The model was used to predict film cooling effectiveness at different combustion-chamber pressures and film blowing rates at sub-, trans-, and supersonic conditions.

The important gaseous film cooling studies and the injection hole configuration used are summarised in Table 1.1. It can be noted that there is no systematic study in literature which describes film cooling performance of straight (axi-symmetric) and compound angle (direction oblique to the mainstream direction) gaseous coolant injection inside a cylindrical geometry similar to a rocket combustion chamber. However, the effect of compound angle injection is widely studied in the case of flat and curved surfaces. A chronological review of literature on a few relevant studies, ranging from film-cooled flat surface to curved surfaces is presented below.

Among the earliest studies, Goldstein et al. (1966) used a 35° inclined axial injection hole with an initially round cross-section widened to each side by 10°. A significant increase in the film cooling effectiveness compared to cylindrical holes was

reported by him. Many studies are available for film coolant measurements over a flat plate surface with a stream-wise angle injection of 35° and with compound angle injection (Ligrani et al., 1994; Lee et al., 2002). They all reported that compound angle injection provided better lateral coverage. Sen et al. (1996) investigated the effect of three different compound angles of a circular hole and reported that compound angle with forward expansion holes had increased lateral mixing and heat transfer coefficient which further increased with increasing momentum flux. Ekkad et al. (1997) reported film cooling effectiveness for compound angle holes with relatively high turbulence intensity and found that higher density injectant tends to result in a higher film cooling effectiveness for streamwise injection, while lower density coolant results in a higher effectiveness for a large compound angle. Lee et al.'s (2002) experimental studies showed improved effectiveness at high blowing ratios for compound angle shaped holes. However, the occurrence of hot cross flow ingestion into the film hole at the hole exit plane was observed for large orientation angles. McGrath and Leylek (1998) have conducted numerical simulations for the same configurations of Sen et al. (1996) and found that the forwardly expanded holes provide substantial improvement in the film cooling performance, however, simultaneously producing undesirable cross flow ingestion into the film hole. Baheri et al.'s (2008) numerical simulations for the same configuration showed that compound angle shaped holes with trench at the exit of circular and fanshaped film holes resulted in considerably higher average effectiveness. They observed that jet lift-off was eliminated at high blowing ratios for the trenched fanshaped hole and the coolant spread more in the stream wise direction. A compound angle injection study for holes with large stream wise angle injection was done by Nasir et al. (2001). Their results showed significant variations in the film effectiveness and enhancement of local heat transfer coefficients.

Cho et al. (1999) investigated the effects of compound angle of film cooling performance of a single conical-shaped hole with orientation angles of 0°, 45° and 90°. Their results favour compound angle injection than axial injection for effective surface protection. Experimental investigations of laterally diffused and forward diffused compound angle injections were carried out by Bell et al. (2000). It was observed that the best overall protection over the widest ranges of blowing ratios, momentum flux ratios and streamwise location is provided by laterally diffused compound in-

jection followed by forward diffused compound injection. A detailed analysis of the physics of film cooling for compound angle injection with shaped holes was carried out by Brittingham and Leylek (2000). Computational results were presented on the adiabatic effectiveness and heat transfer coefficient. The study showed that the superposition of effects for compound angle cylindrical holes and stream wise shaped holes do not necessarily apply to Compound-Angle Shaped-Holes.

Maiteh and Jubran's (1999) studies showed that increasing the free-stream turbulence intensity and the presence of favourable pressure gradients in the flow was found to reduce the film cooling effectiveness for compound angle holes or combination of simple and compound angle holes. Experimental investigation of two staggered rows of compound angle holes by Jubran et al. (1997) also showed similar results. Experimental investigation of single row of diffuser shaped holes with compound angle injection was done by Dittmar et al. (2003). A strong influence of the cooling air cross flow direction was observed for all blowing ratios. Their results showed that the fan-shaped hole with a compound angle provided the highest film cooling effectiveness at high blowing ratios compared to other film holes. The film effectiveness downstream of a row of compound angle cylindrical and diffused shaped film holes were investigated by Taslim and Khanicheh (2005). The results showed that the best overall protection over widest range of blowing ratios was provided by diffuser shaped film cooling holes, particularly at high blowing ratios. Recently Ghorab (2011) showed that the film hole configurations with interior bending produced better film-cooling performances compared to other schemes in literature.

Waye and Bogard (2007) found that for mild curvature, flat plate results were sufficient to predict the effectiveness performance and that for high blowing ratio, a compound angle jet was well suited for enhanced cooling effectiveness. A detailed study that evaluated the film cooling performance on curved walls with compound angle configuration was attempted by Hung et al. (2009). The measurements showed that for concave surfaces, higher heat transfer levels induced by large flow disturbance of compound injection lead to poor overall film cooling performance especially at high blowing ratios. Compound angle injection on convex surface showed higher film cooling effectiveness at moderate and high blowing ratios. They have shown

that the film thickness and turbulence greatly increased by compound angle holes. Sivrioglu's (1991) numerical model predicted higher effectiveness values for convex surfaces compared to flat and concave surfaces. His results showed that the effect of pressure gradient on film cooling effectiveness is more important over curved surfaces than flat surfaces. Numerical investigation of the film cooling effectiveness for five different curved surfaces and a flat surface was done by Koc et al. (2006). Results showed that film-cooling effectiveness depends on the hole geometry, slope of the curved surface and blowing ratio. Numerical simulations of mist film cooling by Li and Wang (2008) showed better effectiveness for concave surfaces at nominal blowing ratios of 1.33. Michel et al. (2009) have carried out experimental and numerical study on a cooling film issuing from a multi-perforated wall of a simplified combustor.

Table 1.2 summarizes the major studies conducted for film cooling configurations involving compound-angle injection. The main qualitative observations from these studies could be summarized as follows:

- Compound-angle injection is employed to have a large coverage area of the film coolant and a broader jet profile to the core gas.
- Higher compounding angles imply greater average effectiveness due to better spread and mixing, however this difference is most noticeable at higher blowing ratios.
- Heat transfer coefficient increases with increasing momentum flux ratio and compound angle orientation.
- Coolant hole orientation and blowing ratio influence the film cooling performance of curved surfaces.

It must however be noted that there are no archival studies reported in literature that deal with this type of coolant jets for circular pipes. In addition, no investigation has been conducted concerning different tangential angles between the coolant and the core gas and their effect on film cooling performance. Obviously, more research needs to be conducted to assess the relative performance of different coolant injector configurations.

Table 1.2: Major compound angle injection studies reported

	Test surface	Main focus of the study
Goldstein et al. (1966)	Flat	Effectiveness improvement
Ligrani et al. (1994)	Flat	Effect of staggered rows of holes
Sen et al. (1996)	Flat	Effect of different angles
Ekkad et al. (1997)	Flat	Effect of turbulence intensity, Density of coolant
Jubran et al. (1997)	Flat	Effect of staggered holes
McGrath and Leylek (1998)	Flat	Effect of shape of hole
Maiteh and Jubran (1999)	Flat	Effect of turbulence intensity, Pressure gradients
Cho et al. (1999)	Flat	Conical-shaped hole with different orientation angles
Bell et al. (2000)	Flat	Effect of shape of hole
Brittingham and Leylek (2000)	Flat	Effect of shape of hole
Nasir et al. (2001)	Flat	Effect of large stream wise angle
Lee et al. (2002)	Flat	Flow visualisation, Effect of blowing ratio
Taslim and Khanicheh (2005)	Flat	Effect of shape of hole
Baheri et al. (2008)	Flat	Effect of shape of hole
Ghorab (2011)	Flat	Hybrid schemes
Waye and Bogard (2007)	Mld curvature plate	Comparison with flat plate
Sivrioglu (1991)	Curved walls	Performance evaluation
Koc et al. (2006)	Curved walls	Comparison with flat plate
Li and Wang (2008)	Curved walls	Mist film cooling
Hung et al. (2009)	Curved walls	Performance evaluation
Michel et al. (2009)	Multi-perforated wall	Performance evaluation

1.3.2 Liquid film cooling studies

Liquid film cooling process is different from that of gaseous film cooling because of the presence of phase change during the cooling process which vastly increases the cooling capacity. However, literature on liquid film cooling is quite limited compared to that of gaseous film cooling. Table 1.3 summarizes the major experimental, analytical and numerical studies conducted for liquid film cooling applicable to rocket combustion chambers. Previous experimental studies available in literature are reviewed below.

One of the first experimental studies in film cooling is done at JPL by Boden (1951). He used nine injector configurations out of which seven were oriented in the radial direction and two were drilled at an angle of 70° off the radial direction. The coolant was injected through multiple drilled holes distributed around the inner wall at one or more axial locations in the engine. An inner ring downstream of coolant injector was used to force the coolant axially before entering the engine. The data obtained was reviewed and correlated by Welsh (1961). It was observed that injection from a single axial location in the combustion chamber was the least efficient method and injection of coolant in a swirling pattern had a negligible effect on cooling performance, although the addition of a deflector plate increased the effectiveness of the coolant. Morrell (1951) had successfully conducted liquid film cooling experiments with a vertical rectangular slot injector and tangential type with slots cut at 45° to the axis. Tangential slot injection failed to improve the effectiveness. Kinney et al. (1952) used porous and jet type injectors with holes cut at an angle of 25° to the axis. No significant difference was noticed in the results with the two different coolant injectors. Abramson (1952) used annular slots inclined at 30° to the centre line of the nozzle in his internal film cooling experiments of the exhaust nozzle of a liquid ammonia-liquid oxygen rocket engine. Film cooling of the entire nozzle was achieved with film coolants such as water and anhydrous ammonia. Knuth (1954) conducted experiments with radial injector holes and determined sufficient conditions for the stability of thin liquid film flowing under the influence of high velocity turbulent gas streams. Gater et al. (1965) conducted experiments with a flat film and measured the amount of liquid that remained attached to a wall with a knife-edge capture slot. Warner and Emmons

Table 1.3: Major liquid film cooling studies applicable to rocket thrust chambers

	Nature of study	Focus of study, Injector types
Boden (1951)	Experimental	Feasiblity of films, Radial injectors
Morrell (1951)	Experimental	Feasiblity of different coolants, Vertical and Tangential slots
Kinney et al. (1952)	Experimental	Performance study, Visualisation of films, Porous and jet type
Abramson (1952)	Experimental	Cooling of nozzles, Tangential slots
Knuth (1954)	Experimental	Stability of liquid films, Radial injector
Warner and Emmons (1964)	Experimental	Feasiblity of H_2 as a coolant, Dual slot radial injector
Stechman et al. (1969)	Experimental	Propellants as coolant
Kesselring et al. (1972)	Experimental	Development of analytical model, Tangential injector
Cook and Quentmeyer (1980)	Experimental	Hydrocarbons as coolant
Volkman et al. (1990)	Experimental	Cooling of nozzle throat
Kirchberger et al. (2009)	Experimental	Kerosene as coolant
Crooco (1952)	Analytical	Analysis of evaporation of liquid film
Knuth (1954)	Analytical	Method for calculating evaporation rate of liquid film
Emmons (1962)	Analytical	Determination of the heat transfer coefficient
Gater et al. (1965)	Analytical	Analytical model including film instability and transpiration effects
Stechman et al. (1969)	Analytical	Introduced 'flow instability efficiency correction factor'
Grisson (1991)	Analytical	Incorporated transpiration, radiative heat transfer and free-stream turbulence
Yu et al. (2004)	Analytical	Swirling of the liquid film
Shembharkar and Pai (1986)	Numerical	Couette flow model
Wang and Luong (1994)	Numerical	Regeneratively cooled engine
Zhang et al. (2006)	Numerical	Coolant loss is approximated by diffusion of vapour

(1964) injected coolant radially through circumferential slots inside the combustion chamber of gaseous hydrogen-air rocket motor. He found that dual slot injection effectively reduced the quantity of coolant required to film-cool a given length of surface compared to that required when a single slot is employed.

The applicability of film cooling to rocket engines using earth-storable, space-storable and cryogenic propellant combinations were investigated by Stechman et al. (1969). In all experiments, fuel was used as film coolant. The studies showed that N_2O_4/MMH, ClF_5/MMH and other similar propellant combinations are readily adaptable to small film-cooled spacecraft engines. Fuel as film coolant was injected from the circumferential cooling holes of the injector, which were directed at various chamber impingement angles in order to ensure complete coverage of the walls. The details of the injector configurations were not available and hence it is not possible to make any critical comparisons. Kesselring et al. (1972) performed tests with tangential coolant injectors in a nickel calorimetric chamber. The authors assumed that the liquid film was immediately evaporated, based upon calculations of the normally expected heat flux without transpiration. Cook and Quentmeyer (1980) had noticed that carbon deposition was the limiting factor of hydrocarbon fuels. Although several experimental investigations are available in the area of liquid film cooling, they do not specifically deal with liquid film injector orientations. Tangential injectors are used in most cases and the effect of coolant injector orientations has not been properly characterized. Therefore, as in the case of gaseous film cooling, more investigations need to be initiated to determine the relative performance of different film cooling configurations.

The analytical and numerical models available in literature are examined next. One of the early work reported is that of Knuth (1954) wherein the analysis was based on an extension of the Reynolds analogy to heat, mass and momentum transfer in the turbulent core of a two component fully developed turbulent pipe flow with unidirectional radial diffusion. He had considered only the unidirectional radial diffusion and neglected all other mechanisms including the evaporation of liquid film due to convective and radiative heat transfer. Crooco (1952) utilized the same interfacial energy balance as Knuth, and hypothesized that liquid film coolant evaporates and diffuses

from the boundary towards the hot gas of combustion. The vapour is then confined in a laminar sub layer that behaves as a thermal barrier. Emmons's (1962) analysis considered incompressible flow of the hot gas stream, flowing over a stable liquid film having a uniform temperature equal to the boiling point of the liquid. The velocity profile within the sub layer was based upon a diffusivity variation relationship, originally suggested by Rannie (1956) and modified by Turcotte (1960). Turcotte's analysis of the sub layer considered the effect of vapour injection upon turbulence. Using the Reynolds analogy, Emmons obtained an expression relating the heat transfer coefficient between the liquid film surface and the hot gas stream. None of the above analyses take into account the heat transfer by radiation which is significant at high temperatures prevailing in the combustion chamber. It also does not account for the disturbances at the surface of the liquid film and the free-stream turbulence effects.

Kinney et al. (1952), Graham (1958), Sellers (1958) and Emmons (1962) equated the convective energy transfer on the surface of the liquid film from the hot gas stream to the energy utilized for the phase change of the liquid coolant. It was assumed that the radiant energy transfer was negligible. Furthermore, in the experimental investigations conducted by Graham, Kinney and Sellers and in a portion of the experimental investigation conducted by Emmons, the wetted surface was essentially adiabatic. Some of the unknown quantities needed for completing the solution were approximated by means of empirical formulae, and the remaining were determined experimentally. The disadvantage was that the final analytical expression could not be applied with confidence to situations that differ significantly from that for which the unknowns were determined. Sellers determined two unknowns and Graham and Emmons each determined one unknown from experimental data. Subsequently, heat and mass transfer analyses for the wall region wetted by the liquid film was carried out by Gater et al. (1965). A correlation procedure was suggested, which require experimental data points, such as the measurement of the structure of the boundary layer region above the liquid film. Film instability at the liquid-gas interface was considered as important as transpiration effects, but the same was considered only above a critical value of liquid flow rate based on observations by Taylor et al. (1963). No assessment of the validity of the correlation procedures were carried out since accurate experimental data were not available.

Analytical methods suggested by Stechman et al. (1969) considered only the convective heat transfer from the main core gas and loss through the chamber walls. He used a modified Bartz (1957) equation to calculate turbulent heat transfer coefficient from the combustion gases to the film coolant. The convective heat transfer coefficient from the liquid film coolant to the chamber walls was calculated assuming turbulent liquid flow on a flat plate and using a 'flow instability efficiency correction factor'. The predictions obtained from the model had errors ranging from -20% to 13% depending on the thrust chamber configuration, either a fully turbulent or transition laminar flow model was used for the analyses. Kesselring et al. (1972) performed tests in a nickel calorimeter chamber using a propellant combination of OF_2/B_2H_6(oxygen difluoride/diborane). Based on the calculations of the normally expected heat flux, the authors assumed that the liquid film is evaporated, without transpiration. They had developed an integral method to determine the film temperature and film heat transfer coefficient. The model was based on an assumed cubic temperature profile through the wall. Volkman et al. (1990) studied the effects of film cooling on reducing the heat flux experienced at the throat of a rocket. Tests were conducted in a subscale LOX/RP-1 high pressure (138 bar) combustor. Peak heat flux reduction of 70% was observed with film cooling in his studies.

A numerical model, assuming a turbulent boundary layer flow for the hot gas stream and a Couette flow model for the liquid coolant film was proposed by Shembharkar and Pai (1986). The model predicts an exponentially dropping evaporation rate and does not account for transpiration effects. Liquid film length predictions were significantly higher than experimental results. An attempt was made by Grisson (1991) to develop a general analysis of liquid film cooling. In Grissom's comprehensive model, transpiration effects, radiative heat transfer and free-stream turbulence were included. Flat plate correlations were used with a modified leading edge distance for convective heat transfer calculations. The radiation calculations were based on Hottel's chart which over-predicted the radiative heat transfer at high temperatures. The entrainment effects were not considered in the analysis and the model was valid only at low coolant flow rates. Wang and Luong (1994) developed an integrated CFD/thermal methodology to design and analyze regeneratively cooled rocket engine combustion chambers. Yu et al. (2004) had performed a literature review on general film cooling models, and

mass and heat transfer correlations used in these models along with the assumptions employed in the analyses. Pertinent benefits of swirling of the liquid film to reduce entrainment was also discussed in this paper. Zhang et al. (2006) numerically solved the governing equations for the liquid film and the gas stream coupled through the interfacial matching conditions. The gas-liquid interface was at the state of thermodynamic equilibrium. The radial component of velocity at the interface was calculated based on the diffusion of coolant vapour from the interface to the core gas flow. The method involved the assumption of arbitrary values for pressure gradient and local liquid film thickness. Liquid entrainment and free-stream turbulence effects were not considered. It is unclear whether the effects of transpiring vapour was properly included as a boundary condition in their model. Kirchberger et al. (2009) conducted film cooling experiments on a sub-scale heat-sink test article running on GOX and kerosene. His results showed that kerosene was much more effective film coolant than nitrogen.

Models currently available in open literature are focussed on the heat and mass transfer at the interface. These models do not account for the interfacial instability and the annular entrainment of liquid film. Flat plate correlations were generally used neglecting the effects of cylindrical combustion chamber. Enough attention has not been given to the radiation heat transfer from the high temperature gases. Recent research in annular two phase flow indicates the presence of interfacial instability phenomenon affecting annular entrainment. The transpiration of vapour from the liquid film decreases the normally expected convective heat flux that makes the radiation significant. Consequently the results obtained through existing models differ significantly in the prediction of the liquid film length in practical combustion chambers. A need, therefore, exists for developing a comprehensive method for the accurate prediction of the location of the terminus of the liquid film.

Liquid film entrainment studies

Limited studies are available in literature which characterise the mechanism of entrainment and film stability in liquid film cooling flows. Kinney et al. (1952) had

made visual observations of liquid film flows on the inner surface of the tubes containing flowing air. Water, water-detergent solutions, and aqueous ethylene glycol solutions were used as film coolants with air stream momentum flux varying from 40,000 to 200,000 Pa. He observed disturbances at the liquid-gas interface causing loss of coolant, when the coolant flow rate was above a certain value. This value was found to be varying with liquid viscosity and surface tension, and did not show any change with air stream Reynolds number. Knuth (1954) from his liquid-film stability experiments confirmed that longer wavelength disturbances appeared only after some critical flow rates of coolant. Small disturbances with wavelength of the order of ten times the film thickness were observed at all flow rates. However, liquid droplets were entrained by the gas stream from the crests of long wavelength disturbances. Gater et al. (1965) conducted experiments with a flat film and measured the amount of liquid that remained attached to a wall with a knife-edge capture slot. Contrary to the observations by Kinney and Knuth, Gater observed that the disturbances at the liquid-gas interface were dependent only on the momentum flux of the gas stream. He proposed that the quantity of liquid entrained was a function of momentum flux of the gas and surface tension of the liquid film. However, it may be noted that Gator's experiments were at lower gas mass flux conditions compared to earlier experiments. Coy et al. (2009) conducted entrainment studies using slot injectors with a Mach number of the test section of about 0.6 and gas momentum fluxes varying from 30,000 Pa to 99,000 Pa. He concluded that there exists a critical flow rate of the coolant film beyond which any additional liquid injected would become entrained into the gas phase. Miller and Coy (2011) had measured the thickness of liquid film driven by high momentum core gas flow. It was observed that at higher gas momentum fluxes, the entrainment depended more on viscosity of the liquid film than the surface tension. However, a thorough understanding of the coolant entrainment mechanism is incomplete and uncertain at present due to the complexity of the entrainment process and a detailed study in this aspect is essential to unravel the physical phenomenon behind the process.

The main qualitative observations from the literature survey conducted could be summarized as follows

- Film cooling investigations over the years have concentrated mainly on gaseous

film cooling applied to gas turbine airfoils followed by the work on film-cooling of rocket combustion chambers.

- Film cooling associated with airfoils corresponds to external flow situation and cannot directly be applied to internal flow associated with rocket combustion chambers.
- The film cooling performance characteristics vary widely, depending upon the type of coolant, flow and geometric parameters.
- In the field of internal film cooling, very few studies deal with coolant film injector orientations. No studies are available which compares liquid and gaseous film cooling for the same injector configurations.
- In the area of liquid film cooling, models currently available do not account for the interfacial instability and the annular entrainment of the liquid film. Radiant heat transfer from the high temperature gases and the effect of transpiration of vapour from the liquid film on convective heat transfer coefficients are usually neglected.
- A full understanding of the entrainment processes and disturbance wave properties at the liquid-gas interface of liquid film cooling flows is incomplete and uncertain at present.

Further research, therefore, is needed to understand the gaseous and liquid film cooling process applicable to rocket combustion chambers and to find better liquid coolant configurations that can provide optimum wall protection. Present study is aimed at an improved understanding of the film cooling process using a combination of experimental and numerical investigations.

1.4 Objective of the Present Study

There are only few experimental studies available which describe film cooling performance of various gaseous and liquid injector configurations inside a cylindrical geometry. There is significant need for experimental data of various types of coolant holes,

both for the design of rocket thrust chamber components, and for the development of numerical models. Therefore, the objectives of the present research work include obtaining detailed experimental data on film cooling performance for various gaseous and liquid film coolant injector configurations. In this regard, circumferentially and span-wise averaged magnitudes of film cooling effectiveness and film uniformity parameters that are measured downstream of straight, tangential and compound angle film coolant injector holes can be analysed and compared.

A systematic computational methodology can be implemented in the case of gaseous film cooling to understand the physics of film cooling and the influence of the major parameters. The dependency of the flow and vortical structure on blowing ratio, stream wise injection angle, conjugate and adiabatic wall conditions, geometric parameters of the coolant injection holes and free-stream turbulence must be investigated. This calls for a detailed simulation and resolution of all the flow features of a film cooling jet. Computational fluid dynamics (CFD) tools can be used to develop an internal wall-jet film-cooling model that is suitably calibrated from the experimental information. This model would be parameterized according to geometry and blowing conditions. The CFD model will enable visualization and understanding of the associated flow phenomenon.

In the area of liquid film cooling, there exists a scope for developing a comprehensive model incorporating all associated phenomenon as is currently understood. The liquid film cooled length is an important parameter in the design of liquid film cooled rocket combustion chamber. Therefore, the emphasis would be on predicting the liquid film cooled length accurately under various injection conditions. The objective also includes the identification of the predominant mechanisms affecting a stable liquid film near the wall.

It is noted that the nature of disturbance waves and the onset of entrainment process of liquid film cooling are poorly understood. The mass transfer via entrainment process can decrease the liquid film length significantly. Therefore the objective of the present research work would also include the generation of a computational model to analyse the nature of disturbance waves and the possible entrainment mechanisms at various coolant and gas flow conditions.

In summary, the specific scope of the study are the following.

1. Design and build a facility to study film cooling performance associated with internal wall-jet gaseous and liquid film-cooling flows.

2. Generate a comprehensive set of film cooling performance measurements associated with

    - straight, tangential and compound angle cylindrical coolant injection holes for the gaseous coolant.
    - tangential and compound angle cylindrical coolant holes for the liquid coolant.

3. Conduct numerical computations to simulate wall jet gaseous film cooling.

4. Highlight all prominent flow mechanisms downstream of gaseous film coolant injection.

5. Describe the effects of various geometric parameters, adiabatic and conjugate walls, blowing ratios, and free-stream turbulence on gaseous film cooling behavior.

6. Develop a superior one dimensional analytical model for liquid film cooling in rocket combustion chambers based on control volume approach and fundamental energy balance concept to predict the liquid film cooled length.

7. Develop a computational model to analyse the nature of disturbance waves and the possible entrainment mechanisms at gas-phase momentum flux conditions similar to rocket combustion chambers.

1.5 Thesis Outline

The thesis report has been organized as follows:

The technical and industrial motivation that lead to this thesis is presented in *Chapter 1*. This is followed by literature review that leads to the objectives of the present research work.

The experimental rig used in the study along with its important ancillary components for creating the requisite core gas flow and cold coolant flow is described in *Chapter 2*. Details of test section, injector configurations, experimental conditions and an estimate of the relative uncertainty in the deduced parameters are described. It also explains the methodology used to obtain the usable effectiveness data from the raw temperature measurements. Important conclusions drawn from the experimental observations are also described.

Chapter 3 presents the numerical simulation of straight gaseous coolant injection (Simulation I). Details of geometry, boundary conditions, grid, governing equations and the solution methodology are described. Equations used for calculating the material properties are described in *Appendix A*. *Chapter 3* also provides a discussion on the major results from the study.

Details of numerical simulation and the results on the study of compound angle gaseous coolant injection (Simulation II) are documented in *Chapter 4*.

Chapter 5 contains the details of the analytical model developed for liquid film cooling. Key assumptions, correlations adapted from literature, solution methodology and model validation are explained. Effects of gas Reynolds number, coolant inlet temperature, combustion chamber pressure, mass flow ratio of the liquid coolant to the core gas and the free-stream turbulence on the liquid film length are presented in detail. *Appendix B* provides a complete set of calculations based on the analytical model.

Chapter 6 establishes a two-dimensional and transient numerical model to explore the entrainment mechanism (Simulation III). The method adopts the RNG k-ϵ turbulence model and the enhanced wall treatment method. In addition, a geometric reconstruction VOF scheme is adopted. The possible liquid entrainment mechanism based on the results from these simulations is also presented.

Chapter 7 summarizes the most important conclusions from all the chapters. A perspective is provided for future work towards the end.

CHAPTER 2

EXPERIMENTAL INVESTIGATION

2.1 Introduction

The present work was initiated with the design and setting up of an experimental facility to study film cooling performance. A test rig is built and detailed measurements were made to obtain data on film cooling performance for various film coolant injector configurations in a cylindrical test section simulating a thrust chamber. The test rig offers a number of new capabilities such as obtaining data for gaseous and liquid coolant of similar injector configurations. It is capable of providing a hot core gas flow with a versatile test section, in which the secondary coolant flow may be injected through various injector configurations. Note that the contents of this chapter is based on Shine et al. (2012a).

2.2 Experimental Setup

The experiments are done with hot air which simulates the hot combustion products. The test facility consists essentially of three parts, viz., (i) a hot air source with a temperature range of 300-800 K, (ii) coolant injection system and (iii) a test section with an exhaust system. A schematic of the set up is shown in Fig. 2.1.

2.2.1 Hot air generator

Atmospheric air is drawn in by a 10 kW blower and is passed through an electric heater of 100 kW, which heats up the air to a core gas temperature that can be set between

300 to 800 K. A flow meter with a control valve is connected in the line to control the core gas flow. The nichrome heater coil radiatively heats up the metal tubing through which the ambient air flows. There are a number of temperature sensors within the furnace for the safety of the heating coil. The maximum flow Reynolds number that can be obtained is of the order of 7.6×10^4. The entire heater assembly and blower are controlled from a control panel. The main-stream temperature is controlled using a feedback loop with a temperature controller. K-type sheathed thermocouples are used to measure the temperature inside the furnace with an accuracy of ± 1 K. The hot air from the flow straightener enters the test section chamber through a calming section. The calming/approach section is 108 mm in diameter and has a length of 1700 mm. The dimensions of the various sections are shown in Fig. 2.2

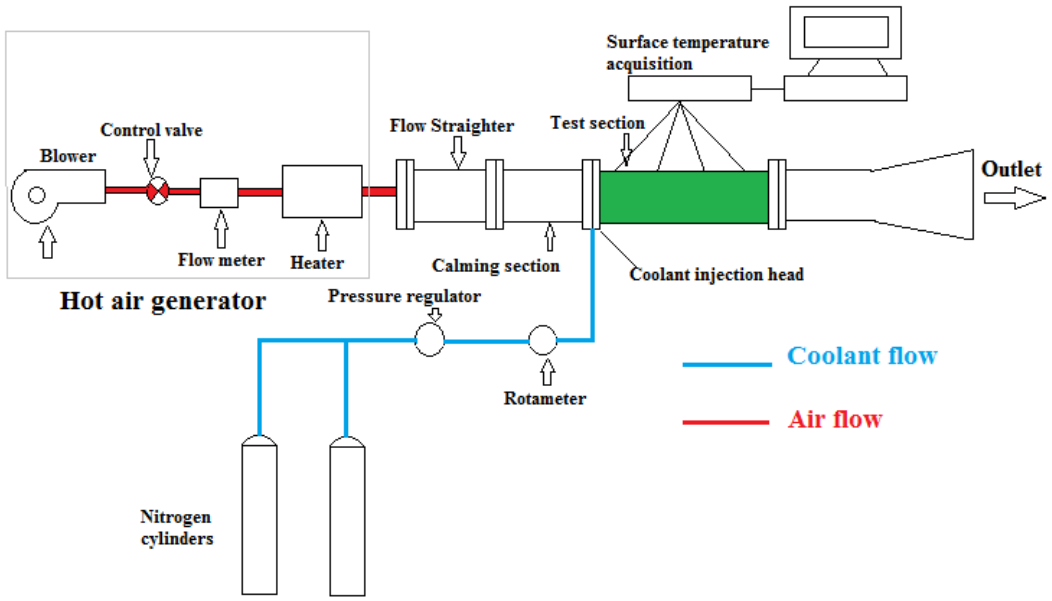

Figure 2.1: Schematic of the film cooling test facility

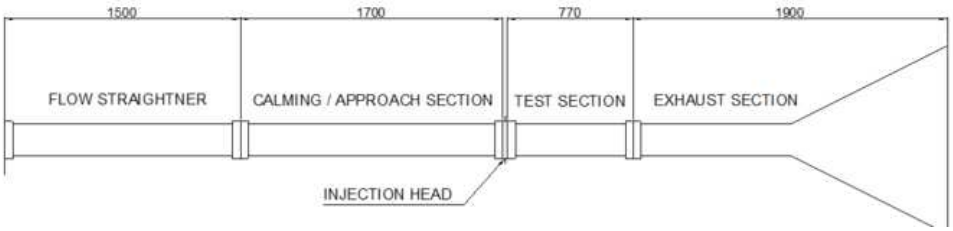

Figure 2.2: Dimensions of various parts of the setup

2.2.2 Coolant Injection System

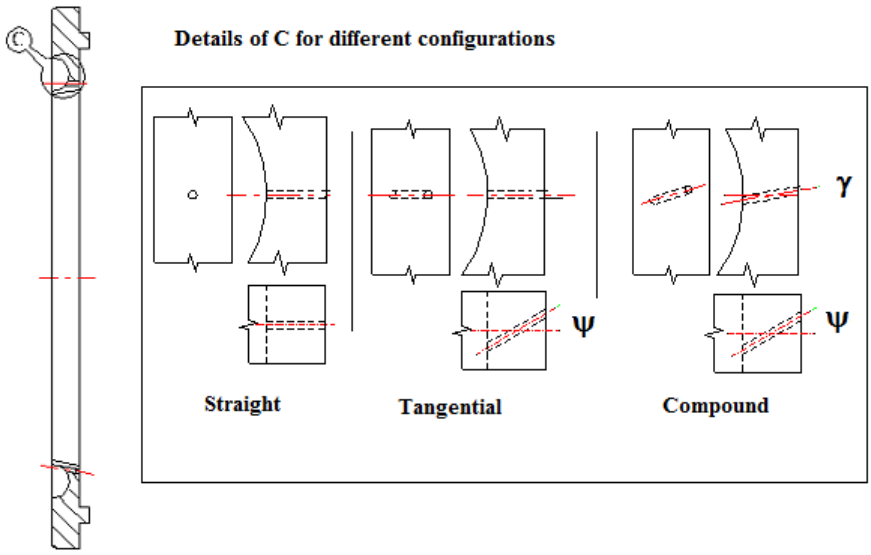

Figure 2.3: Plan, elevation and side views of various coolant injector configurations. ψ is the tangential angle and γ is the azimathal angle.

The gaseous coolant system consists of nitrogen supply cylinder with pressure regulators, rotameter to measure coolant and coolant injector with an inbuilt coolant reservoir. Nitrogen gas is used as the coolant for all gaseous cooling experiments. Nitrogen gas exits through the regulator at a pressure which can be regulated between 1.4 and 2.3 bar. A rotameter, capable of measuring nitrogen gas flow up to 0.0033 m^3/s with an accuracy of $\pm 2\%$ is used to measure the coolant flow rate. The study uses typical configurations of straight and compound angle coolant holes for the gaseous coolant. Experiments are conducted with two configurations of compound angle holes: (i) holes with a tangential angle (ψ) of $30\,^\circ$ having an azimuthal angle (γ) of $10\,^\circ$ (30°-10° injector) and (ii) holes with a tangential angle of $45\,^\circ$ having an azimuthal angle of $10\,^\circ$ (45°-10° injector). Schematic of the holes are given in Fig. 2.3. Two sets of injection holes are used for the liquid coolant. One set of holes has an inclination of 30° (ψ), whereas the other set of holes has a tangential angle of 30° (ψ) and an azimathal angle of 10° (γ).

The gaseous coolant injector is made of two parts for easy fabrication and welded together. It consists of an elliptical grove as reservoir and 50 orifices of 1.5 mm

diameter at a pitch circle diameter of 114.5 mm are drilled from the reservoir manifold, as shown in Fig. 2.4. Details of the two parts of the injector are shown in Fig. 2.5 and Fig. 2.6. Injection orifices of straight, compound angles of 30°-10° and 45°-10° are drilled for coolant injection, each representing an individual hardware. Two inlet ports are provided diametrically opposite to supply the coolant to ensure a uniform flow and an even distribution of coolant through the entire injector orifices.

The liquid coolant injection system consists of a water supply tank and a gaseous nitrogen supply cylinder for pressurizing the water tank with pressure regulator and coolant injection manifold. The injector is similar in construction to that of the gaseous injector and has 50 orifices of 0.55 mm diameter which are EDM drilled. Tangential injector orifices of 30° and compound angle of 30°-10° are drilled for liquid coolant injection. Water exits through the regulator at a maximum pressure of 1.5 bar. The coolant flow is regulated using in-line pressure regulator within the desired range. High pressure nitrogen cylinders are connected in parallel for pressurizing the coolant for long duration tests. The important parameters and capabilities of the test facility are summarized in table 2.1.

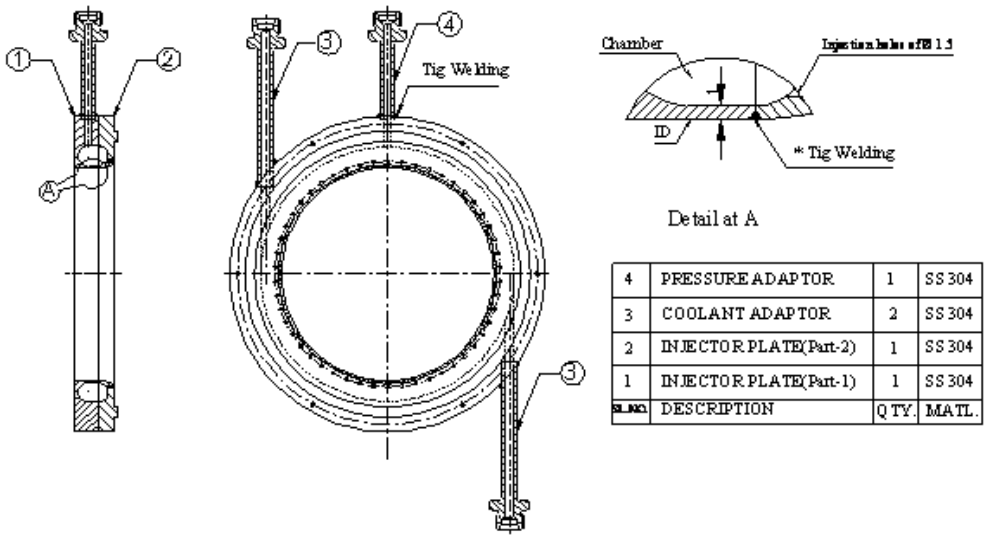

4	PRESSURE ADAPTOR	1	SS 304
3	COOLANT ADAPTOR	2	SS 304
2	INJECTOR PLATE(Part-2)	1	SS 304
1	INJECTOR PLATE(Part-1)	1	SS 304
SL.NO.	DESCRIPTION	Q TY.	MATL.

Figure 2.4: Injector head assembly

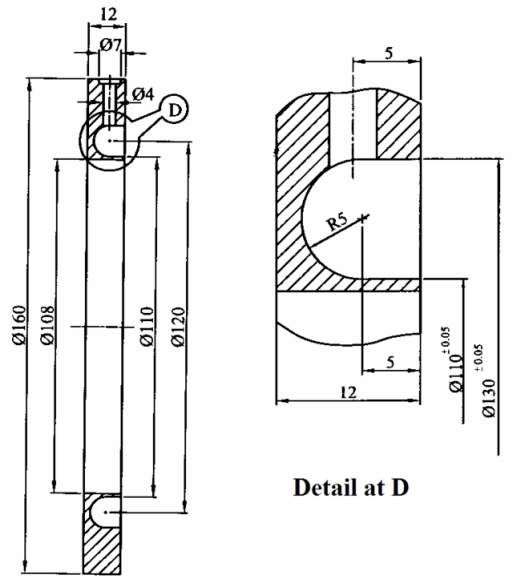

Figure 2.5: Details of the left part of the injector

Table 2.1: Test facility details for film cooling experiments

Parameter	Gaseous cooling	Liquid cooling
Injector type	Straight and compound angles of two orientations, 30°-10° and 45°-10°	Tangential (30°) and 30°-10° compound angle
Coolant hole diameter	1.5 mm	0.55 mm
Coolant	Nitrogen	Water
Core gas flow	Air, 300-800 K	Air, 300-800 K
Core gas Re_g, Max	7.6×10^4	7.6×10^4

2.2.3 Test Section

The test section is made of rolled copper tube of 120 mm inside diameter, 2 mm thick and 770 mm long, which is instrumented with T-type thermocouples to measure the surface temperature as well as the hot air temperature. T type thermocouples of 28 wire gauge are used in the experiments. The diameter is 0.3 mm. Thermocouples are calibrated by using JULABO make refrigerated circulators. This circulator has the capability for working temperatures from 178 K to 473 K. All thermocouple beads are fabricated and welded to the surfaces using a discharge type welder and held tightly using low conducting nylon bands as shown in Fig. 2.7. Thermocouples are calibrated

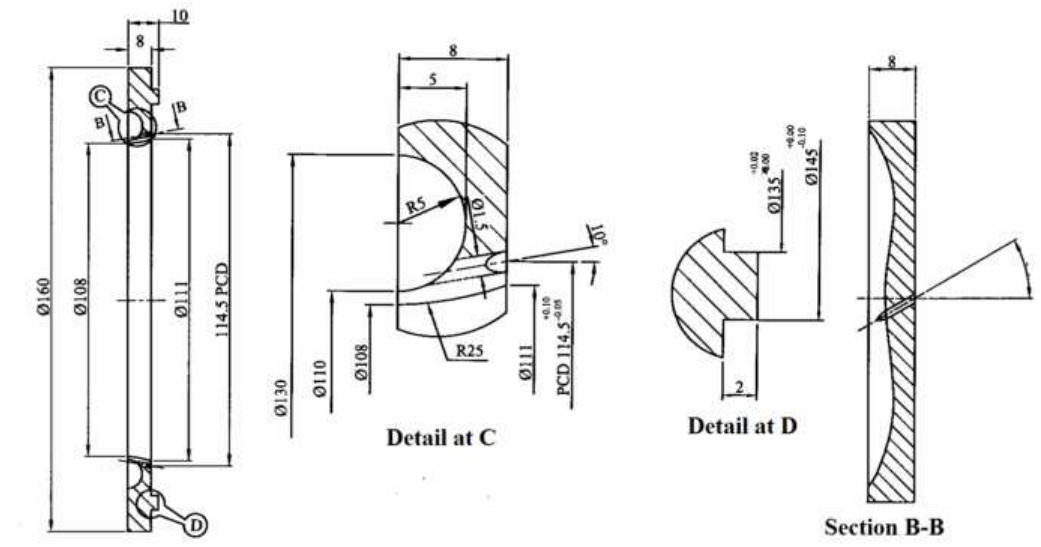

Figure 2.6: Details of the right part of the injector

over the entire measurement range using constant temperature dry blocks prior to attaching them circumferentially on the surface of the test section at equal interval of 30 mm along the length of the test section up to the length of 480 mm. Six such rows of thermocouples are fixed circumferentially at an equal angular displacement of 60° on the test section. Provisions for pressure tapping along the length of the test section allow static pressure measurements. Figure 2.8 shows test section assembly, dimensions, locations of the thermocouple, locations of the pressure tapping and end connections.

Hot air flow is measured by means of an orifice and a U-tube water manometer in addition to the in-line flow meter. The flow was controlled by adjusting the flow valve fixed on the outlet of the blower. The static pressure of the main-stream hot air at 100 mm downstream of the injector assembly is measured using a digital manometer to determine the appropriate air densities and velocities. Temperatures of main-stream flow, the coolant and the surfaces of the test section are one of the primary measurements in the experiment. A total of 96 thermocouples are located on the test section circumferentially and two thermocouples are inserted into the cylinder to measure the inside hot air temperature at its center. All thermocouple outputs are fed to a Keithley model 2750 Multi-meter capable of measuring 120 channels. All thermocouples along with the multi-meter are checked for consistency and repeatability.

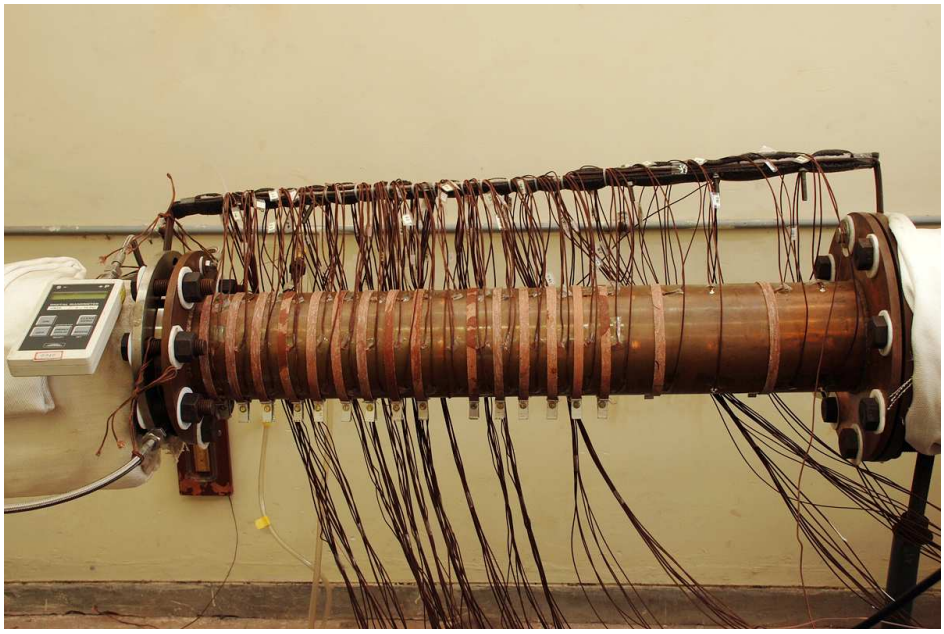

Figure 2.7: Injector and test section instrumentation

2.3 Experimental Conditions

Furnace temperature required for a specific air temperature is identified initially over a range of operating temperatures. After temperature stabilization of the furnace for the desired value of gas temperature, the blower is switched on and the ambient air is allowed to enter the furnace and the air gets heated. Simultaneously the nitrogen gas as the coolant is also allowed to pass through the coolant injection orifices. Once steady state conditions are reached, indicated by the constant temperature read outs, the hot air and test section surface temperatures are recorded for the set mass flow rate of the coolant and hot air. The digital manometer and rotameter readings are also noted. The experiments are repeated for all the test section configurations for different blowing ratios and hot air temperatures. In all, 40 experimental runs were conducted; eight each for individual orifice configuration. Additional experiments were carried out to initialize the heater and other test conditions. Inferences on film stability and uniformity that will be drawn from the measurements, largely depend on the temperature sensitivity of the entire measurement chain and its repeatability after each set of measurement. In this regard, it is ascertained before the commencement of each test that the entire temperature measurements on the test section are within the

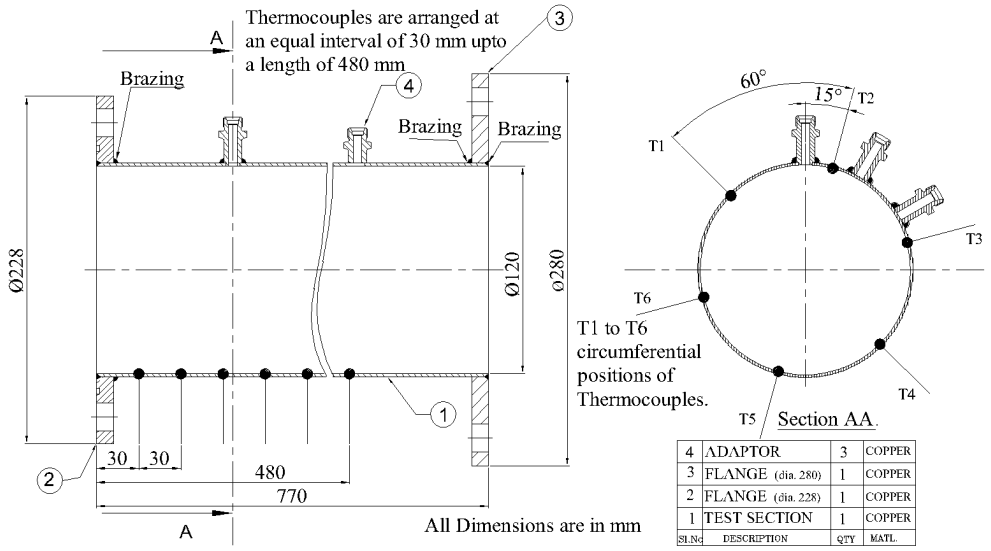

Figure 2.8: Crossectional view of the test section showing locations of the thermocouple and pressure tapping.

allowable dispersion level of ± 0.5 K without film cooling. Experiments have been carried out over a range of coolant flow rates and temperatures. As the study is aimed to qualitatively bring the effect of compound injection angles on various film cooling parameters, experiments are done only at relatively lower temperatures. During the experiments with gaseous coolant film cooling, hot air temperatures are maintained at 343 and 397 K. However, in the case of liquid coolant injection, these temperatures are maintained at 383 and 404 K, which are well above the saturation temperature of the coolant water (373 K). The coolant temperature in all the cases is fixed at 300 K. Coolant injection pressures is varied from 0.25 to 2.4 bar (gauge) for the investigation. Two flow rates for nitrogen, 0.0021 m^3/s and 0.0028 m^3/s are used in the gaseous film cooling experiments. For liquid coolant experiments, water flow rate is varied from 0.07 kg/s to 0.16 kg/s. Two flow rates of hot air, viz., 0.09 and 0.13 m^3/s are considered for each coolant flow rate.

2.4 Film Cooling Effectiveness and Blowing Ratio

Film cooling will result in reduction of heat load to film protected surface. This will cause reduction of outer surface temperature of the test section. Therefore, a nondimensional film cooling parameter, $\eta(x/D)$, based on the outer surface temperature is used for comparing film cooling performance. Since it is a nondimensional variable, it can be related to temperatures that could occur at real engine conditions. Film cooling parameter $\eta(x/D)$ is defined by

$$\eta(x/D) = \frac{[T_{out}\,(x/D) - T_g]}{[T_c - T_g]} \tag{2.1}$$

In the real rocket engine operation, absolute coolant temperature is typically low compared to that of the hot core gas temperature. This results in very low temperature ratio (typically around 0.1) between the coolant and core gas. When using a high temperature ratio (0.73 and 0.84 in the present study) in laboratory studies, matching performance results to engine conditions at high temperature ratios can be done by matching the blowing ratio. The blowing ratio (M) is defined as

$$M = V_c\rho_c/V_g\rho_g \tag{2.2}$$

The blowing ratio scales the thermal transport capacity of the coolant since the convective transport is proportional to $\rho c_p V_c$. Therefore, when testing with a temperature ratio that does not match the engine conditions, the blowing ratio can be matched to the engine conditions to get reliable results.

2.5 Scaling of Film-Cooling Performance with Varying Density Ratio

A number of studies have been conducted to evaluate the effects of coolant to mainstream density ratio (DR) on film effectiveness performance including Pedersen et al. (1977), Baldauf et al. (2002), and Sinha et al. (1991). These studies were conducted

using flat surface, zero pressure gradient test facilities with a single row of coolant holes inclined 35 deg to the surface and oriented in the mainstream flow direction. These studies showed that, although there are distinct differences between low and high DR coolant jet performance, the film effectiveness performance was similar when selecting the appropriate scaling parameter. At very low blowing ratio, M = 0.2, Pedersen et al. (1977) found that laterally averaged film effectiveness was essentially the same for coolant DRs ranging from DR = 0.8 to 4. At this low blowing ratio, the coolant jets were well attached for all DRs and therefore, the film effectiveness performance was dependent on M . At higher blowing ratios, Pedersen et al. (1977) found better film effectiveness for higher DR coolant jets operating at the same M. This is due to the lower density coolant jets having higher momentum ratios and, hence, a tendency to separate from the surface. Baldauf et al. (2002) compared film effectiveness for coolant DR = 1.2 and 1.8 over a range of blowing ratios from M = 0.2 to 2.5. The distributions of effectiveness were similar for both DRs, but the DR = 1.8 coolant had a peak film effectiveness of 0.38, whereas for DR = 1.2 the peak was 0.32. This may be attributed to better lateral distribution of the high-density coolant as noted by Sinha et al. (1991).

2.6 Uncertainty Analysis

The relative uncertainty in the deduced parameters such as the film cooling effectiveness and the blowing ratio has been estimated using the methods described in Kline and McClintock (1953) and Moffat (1985). The uncertainty estimates of the deduced parameters is based on the uncertainties of the primary measurements. The uncertainty in a given function F of the independent variables x_1, x_2,. . .,x_n would be

$$\omega_F = \left[\left(\frac{\partial F}{\partial x_1} \right)^2 + \left(\frac{\partial F}{\partial x_2} \right)^2 + \cdots + \left(\frac{\partial F}{\partial x_n} \right)^2 \right] \tag{2.3}$$

In the present study, the measured variables are pressure and temperature. Though the thermocouples are calibrated within ± 0.5 K accuracy, due to repeated thermal

cycling, the temperature measurements will be known within ± 1 K and the lowest temperature difference measured that is used for computing film cooling effectiveness is 45 K for nitrogen, this would formulate to an uncertainty of $\pm 2.2\%$. Uncertainty in pressure measurement would account to less than $\pm 8\%$. The uncertainty in diameter associated with the fabrication of coolant injector holes is estimated to be $\pm 3.3\%$. After considering the uncertainty of the rotameter and manometer measurements of $\pm 2\%$ and $\pm 8\%$, the uncertainty in estimating blowing ratio is calculated as $\pm 14\%$. The combined uncertainty for the estimation of film cooling effectiveness with respect to blowing ratio would therefore be $\pm 14.5\%$.

2.7 Results and Discussion

As discussed earlier, experiments were conducted and measurements were carried out for (i) straight gaseous injection holes, (ii) 30°-10° compound angle gaseous injection holes, (iii) 45°-10° compound angle gaseous injection holes, (iv) 30° tangential liquid injection holes, and (v) 30°-10° compound angle liquid injection holes. The results of the experiments conducted are described in detail in the following sections.

2.7.1 Gaseous film cooling

Effectiveness

Wall temperature in the vicinity of coolant injection is lower as a film of coolant protects the wall from the hot air. The coolant mixes with the hot air in the downstream regions and results in a gradual temperature rise of the test section. Gaseous film cooling effectiveness was compared with previously published data in order to validate the current experimental techniques and methodology. Results from the present experiment are shown in Fig. 2.9. Circumferentially averaged effectiveness of straight and 30°-10° compound angle injection is plotted against the non-dimensional length of the test section (x/ D) for two values of momentum flux ratio, I = 3 and I = 5.5. It is

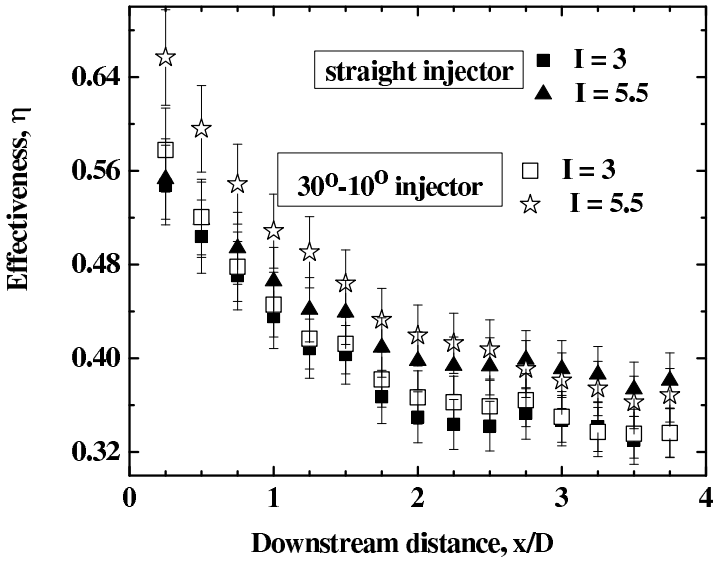

Figure 2.9: Circumferentially averaged effectiveness variation along the test section length for the gaseous coolant

noticed that adding a compound angle did not significantly change circumferentially averaged effectiveness values compared to the straight hole, at lower momentum flux ratio (I) between the coolant and hot air. But at relatively high momentum flux ratio, compound angle holes had significantly greater effectiveness than the straight holes. At I = 3, an increase of 5.5% is obtained for effectiveness in the case of compound angle, whereas at I = 5.5, an increase of 18.8% is noted. These results are in good agreement with the results obtained by Schmidt et al. (1996). Hung et al. (2009) have investigated detailed distributions of film cooling effectiveness on concave surface with one row of injection holes inclined stream-wise at 35 degrees at four blowing ratios (0.5, 1.0, 1.5 and 2.0) with different hole configurations. Simple and three compound angles of 0, 45 and 90 degrees with the coolant to mainstream density of 0.98 are tested under the mainstream Reynolds number (Re_d) of 2300. Results showed that the compound-angle injection produced higher film cooling effectiveness at moderate and high blowing ratios. Fig. 2.10 shows the film cooling effectiveness comparison of the present study and that of Hung et al. (2009) for both configurations. It is seen that compound angle produced higher effectiveness in both studies.

To compare the effectiveness of the different geometries over a full range of momentum flux ratios, spatially averaged effectiveness ($\overline{\overline{\eta}}$) values are used. Spatially

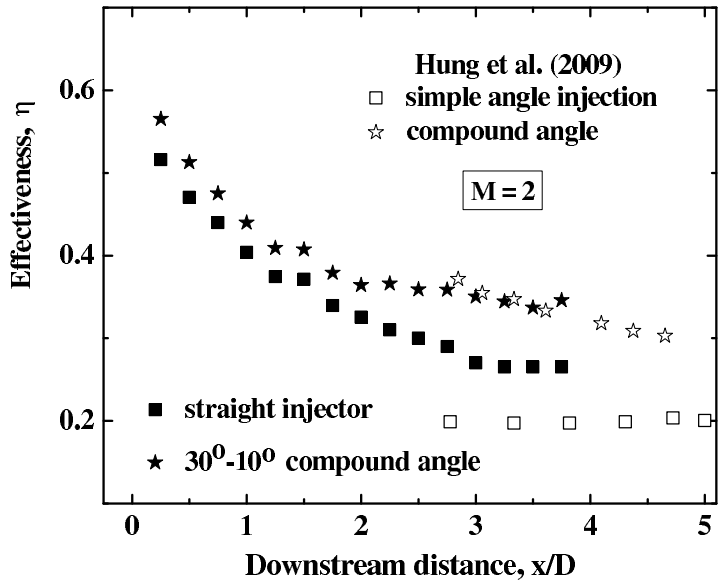

Figure 2.10: Comparison of the present study with Hung et al.(2009)

averaged effectiveness is defined as the integral average of the circumferentially averaged effectiveness along the axis. $\bar{\bar{\eta}}$ is calculated for a distance upto 120 mm downstream of the film coolant injection. Figure 2.11 shows the variation of $\bar{\bar{\eta}}$ with momentum flux ratio. Effectiveness decreased slightly with increasing I for the compound angle holes, but still had reasonably good effectiveness compared to straight holes. Effectiveness values however started increasing beyond a critical value of momentum flux ratio. This effect is further analysed using the computational model and is discussed in section 3.3.3. Adding compound angle significantly increased the extent which higher levels of effectiveness were maintained. Ligrani et al. (1994) and Schmidt et al. (1996) had also obtained similar results, i.e. the effectiveness of the compound angle holes decreases with increasing I, but improved relative to the straight injection case. No experimental values were available from earlier experiments for values of I beyond 3.9.

It can be concluded that the current experimental techniques and methodology produced results that are in good agreement with previously published data, within experimental uncertainty. The validation of the measurement technique gives confidence in the subsequent results.

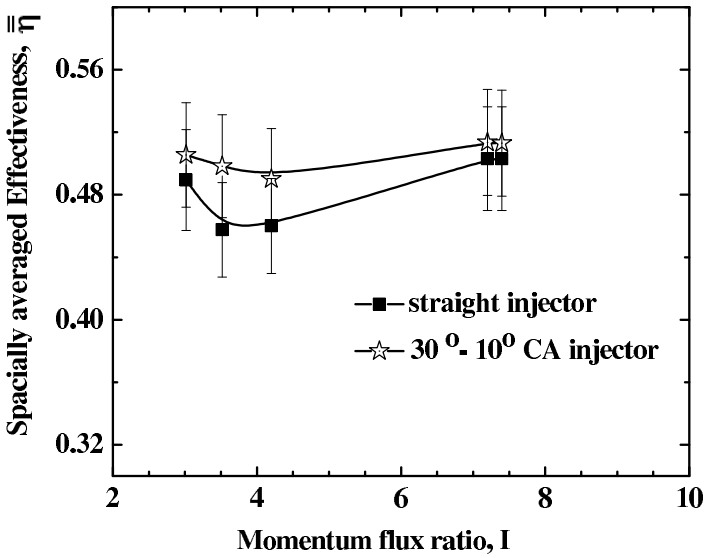

Figure 2.11: Spatially averaged effectiveness variation for straight and 30°-10° compound angle gaseous injector at different momentum flux ratios.

Influence of tangential angle

Effectiveness variation along the test section length for 30°-10° and 45°-10° compound angle injection for gaseous coolant at two blowing ratios is shown in Fig. 2.12a and 2.12b, respectively. It is seen that increasing the tangential angle to 45° results in lower effectiveness. It is also found that the trend remains similar even at a lower core gas temperature of 343 K as shown in Fig.2.12c. At high impingement angles, the film does not stick to the wall and may disintegrate leading to increased wall temperature as can be seen from the profile. It may however be noted that although the differences are not very significant, they are not negligible and will be multiplied many fold while using a lower coolant injection temperature and a higher core gas temperature. The factors leading to this phenomenon can be attributed to the flow behavior of the coolant and its interaction with the core flow for different injector configurations. An in-depth analysis of the flow field and Nusselt number distribution downstream of coolant injection is done using the computational model to document the physical mechanisms for the outcome. The inferences obtained from the computational model is explained in Section 4.3.1, 4.3.2 and 4.3.3.

2.7.2 Liquid film-cooling

Relative merit of tangential and compound angle injection

Effectiveness variation along the test section for 30° angular and 30°-10° compound angle injection with liquid coolant is shown in Fig.2.13. Comparison is done at two core gas temperatures of 383 K and 404 K for various injection pressures. Effectiveness at various coolant injection pressures and a trend line for average value is shown. The results show that adding a compound angle to tangential injection produced an improvement in effectiveness close to the injection point i.e., for x/D < 0.75. At higher x/D ratios tangential injection has the advantage of improved effectiveness. In compound angle injection, it is expected to have broader distribution of coolant near the injection region and higher heat transfer coefficient. Lower effectiveness observed for

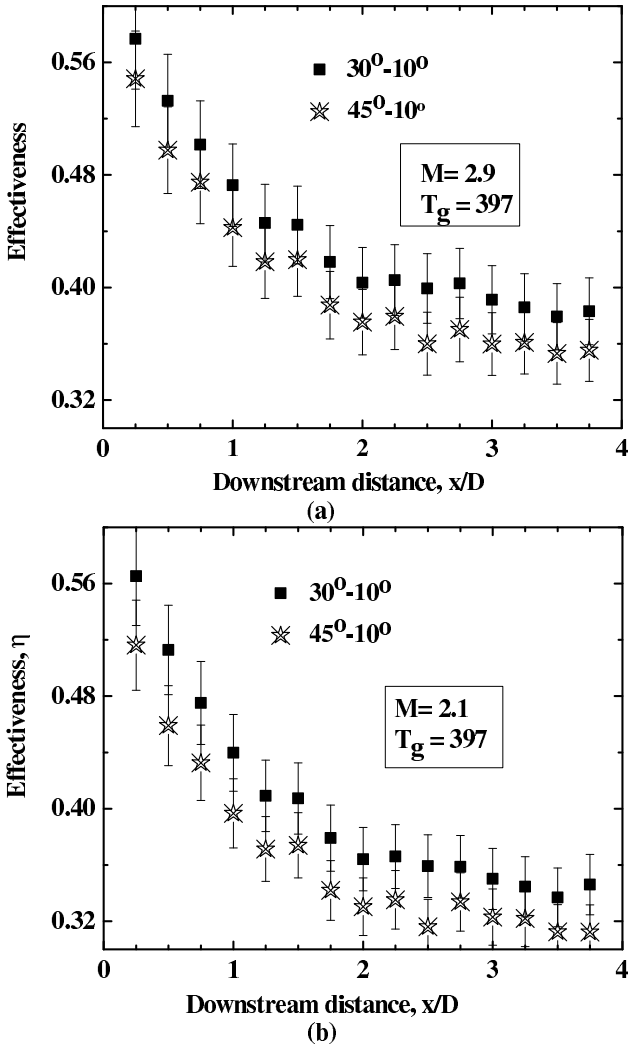

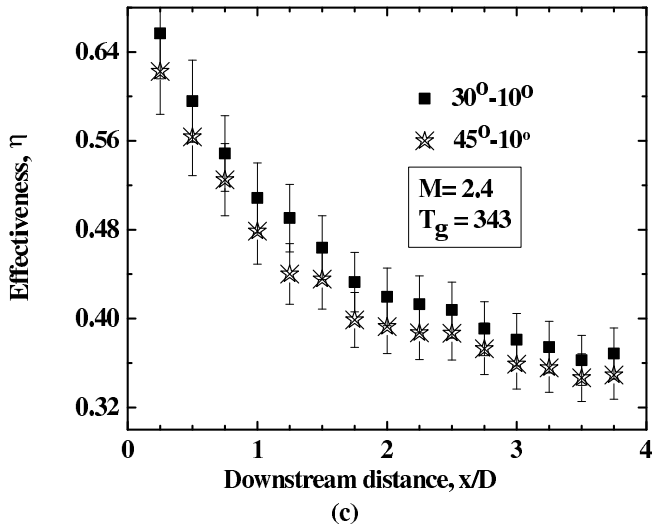

Figure 2.12: Circumferentially averaged effectiveness variation along the test section for the compound angle gaseous coolant injectors at different blowing ratios (a) M = 2.9, (b) M = 2.1 and (c) M = 2.4.

the compound injector indicates higher heat transfer coefficients and higher heat flux to the chamber wall. This also results larger reduction in effectiveness at higher core gas temperature.

Effect of core gas temperature

The test section outer surface temperature variations with x/D for the liquid film injectors at different core gas temperatures are presented in Fig.2.14. Comparison is done at the same coolant injection pressure of 1 bar. Higher surface temperatures are observed with higher mainstream temperature in both cases. This is due to the increased evaporation of the coolant and the associated reduction in film thickness. Therefore, shorter film cooled length is expected at elevated core gas temperatures.

Comparison between compound angle gaseous and liquid coolant injection

Figure2.15 shows the effectiveness variation of gaseous and liquid coolants for the 30°-10° injector configuration. Average effectiveness values for a particular core gas temperature are plotted against the normalised axial distance. As expected, liquid

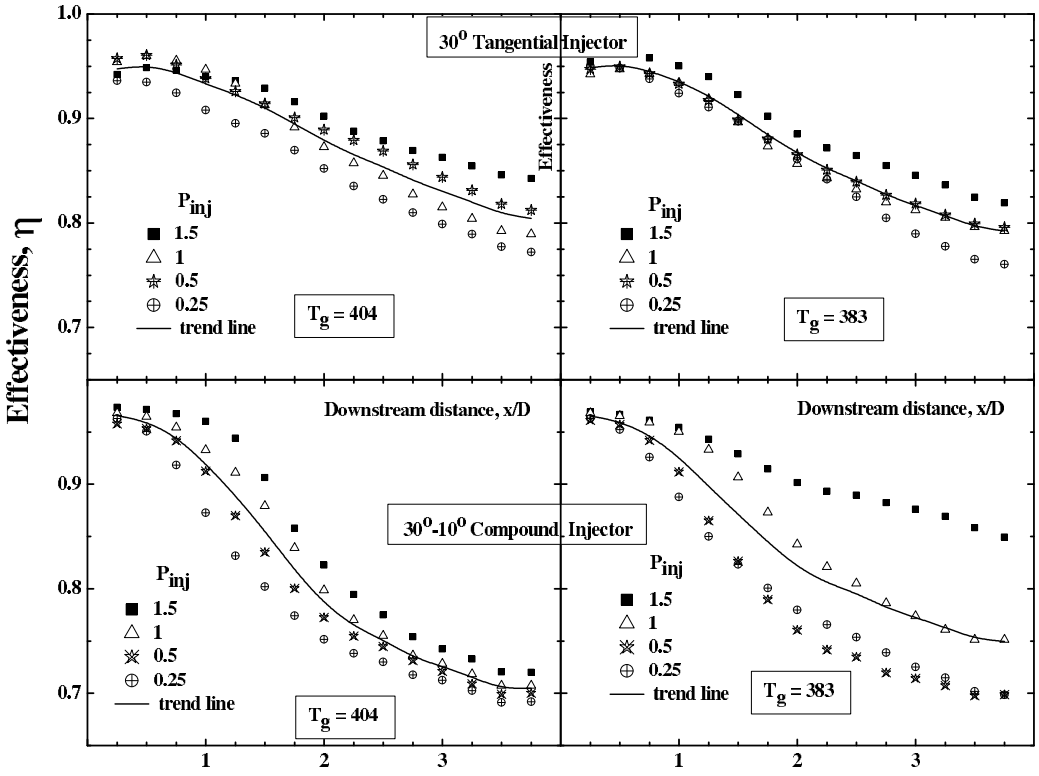

Figure 2.13: Variation of circumferentially averaged effectiveness along the test section for the liquid coolant injectors

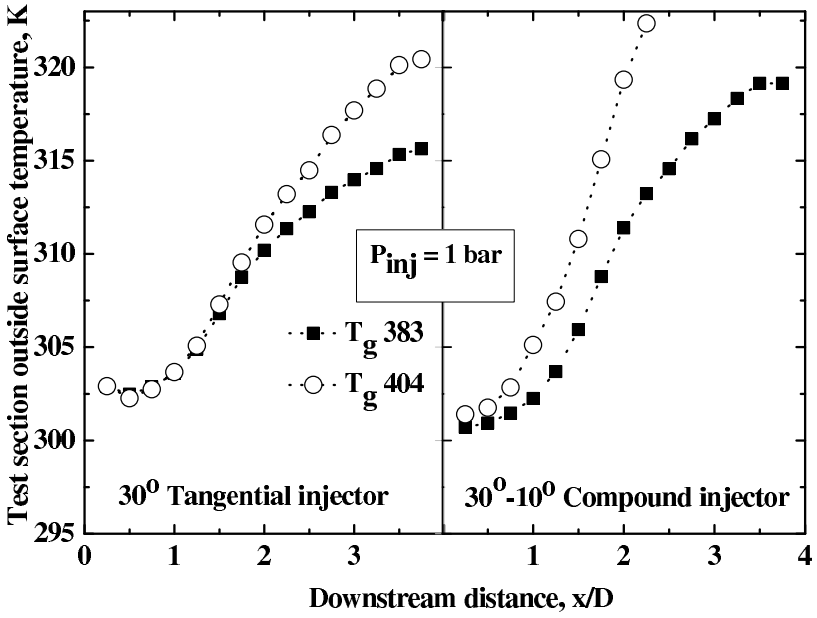

Figure 2.14: Wall outer surface temperature variation of the test section with liquid film cooling

effectiveness are high due to the associated high momentum flux ratio. For liquid coolant, effectiveness initially shows flat characteristics, while that of gaseous coolant is continuously dropping. This may be attributed to better lateral distribution of the high-density coolant as noted by Sinha et al. (1991). The lower density coolant jets have a tendency to separate from the surface. The length of the film cooling influence is comparatively lesser for gaseous injection as the effectiveness curve flattens after x/D = 2. But the higher momentum flux, present in the case of liquid coolant, allows the film to move axially over a larger distance.

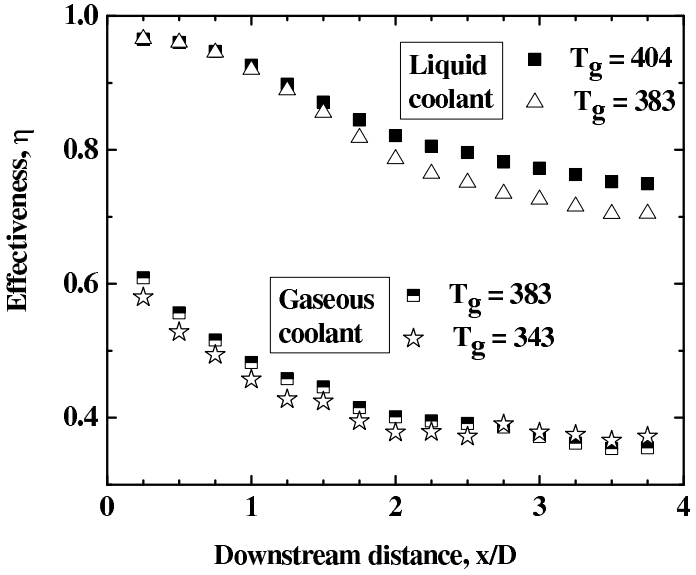

Figure 2.15: Circumferentially averaged effectiveness variation along the test section for the 30°-10° gaseous and liquid coolant injectors

2.7.3 Film uniformity results

The uniformity of the film around the circumference is essential so that no local hot spots are created. The dispersion in the radial wall temperature measurements at every axial location is suggestive of the uniformity of the coolant film beneath it. Figure 2.16 illustrate the standard deviation of the radial temperature measurements at every axial location of the test section for the 30°-10° gaseous and liquid injector respectively. Curves are obtained at different injection pressures. It is observed that the deviations are minimum at regions near to the injection points for both liquid and gaseous

coolants and become significant, away from the coolant injection locations. This is attributable to the increased turbulence and mixing between the core and coolant leading to un-symmetry and non-uniformity in film. The trends are similar at all injection pressures. It can be noted that higher injection pressure is essential to keep the liquid film uniformly around the circumference of the test section.

Figure 2.17 shows the variation in the standard deviation of the radial temperature measurements along the test section for all the investigated injector configurations. Fig.2.17a and 2.17b show the influence of injector geometry for the gaseous and liquid coolants respectively. From Fig.2.17a, it is evident that all three injector geometries for the gaseous coolant give about similar variations, indicating similar interaction of the coolant with the core fluid for each injector around the circumference. Compound angle injection of liquid coolant shows significant variation in temperature around the circumference compared to the tangential injection. It can be concluded that film is not properly maintained around the circumference away from the injection point. The additional velocity component imparted by the compound angle injection causes the jet to hit at the top surface and hence fails to maintain the film properly.

2.7.4 Circumferential effectiveness variation

For a heated cylinder, local Nusselt numbers are influenced by boundary layer development, which begins at the bottom of the cylinder and concludes at the top with formation of a plume ascending from the cylinder. If the flow remains laminar over the entire surface, the distribution of the local Nusselt number is characterized by a maximum at the bottom and a monotonic decay along the circumference. This will affect the temperature measurements in any vertical plane. Fig.2.18 shows the effectiveness distribution features for the straight injector at two axial locations. Effectiveness peak is located at the bottom of the jets and is due to non-uniform azimuthal heat transfer. Similar trends are observed for all injectors.

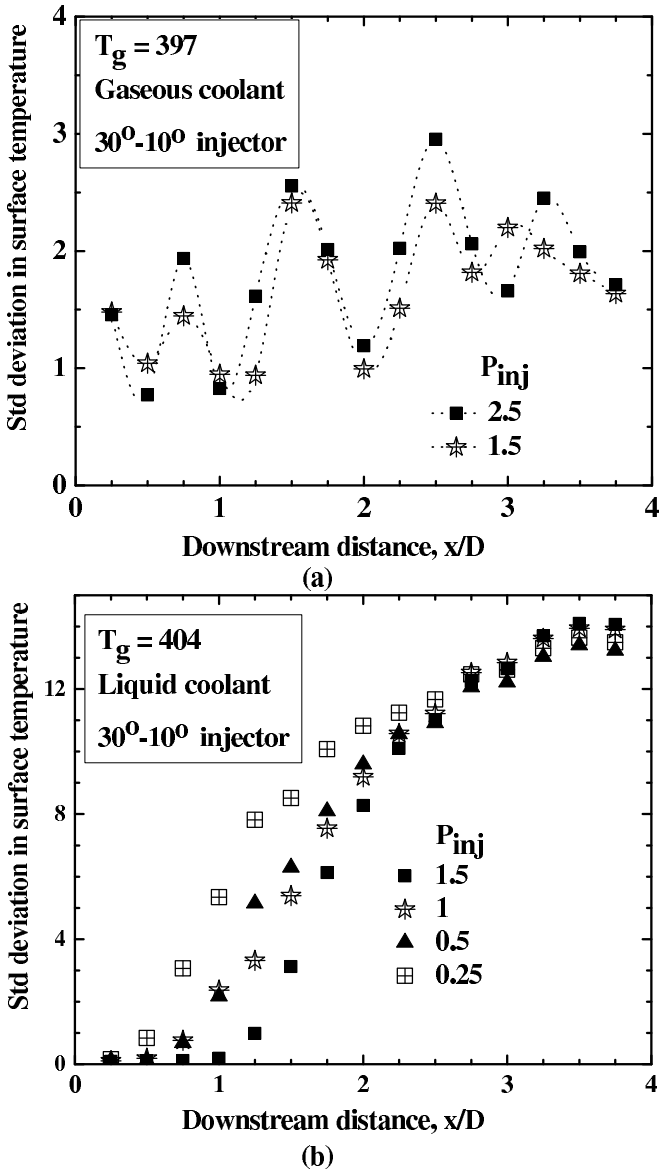

Figure 2.16: Film uniformity representation in terms of standard deviation in wall temperature for the 30°-10° injectors at various injecction pressures (a) gaseous coolant and (b) liquid coolant

2.7.5 Effect of coolant injection pressure and core gas temperature on effectiveness

Film cooling effectiveness at different coolant injection pressure and core gas temperature is plotted against the normalised test section length in Fig.2.19. Comparison is done for various injector configurations. Gaseous and liquid coolant injection for 30°-10° compound angle injector is compared in Fig.2.19a and Fig.2.19b. The effects are

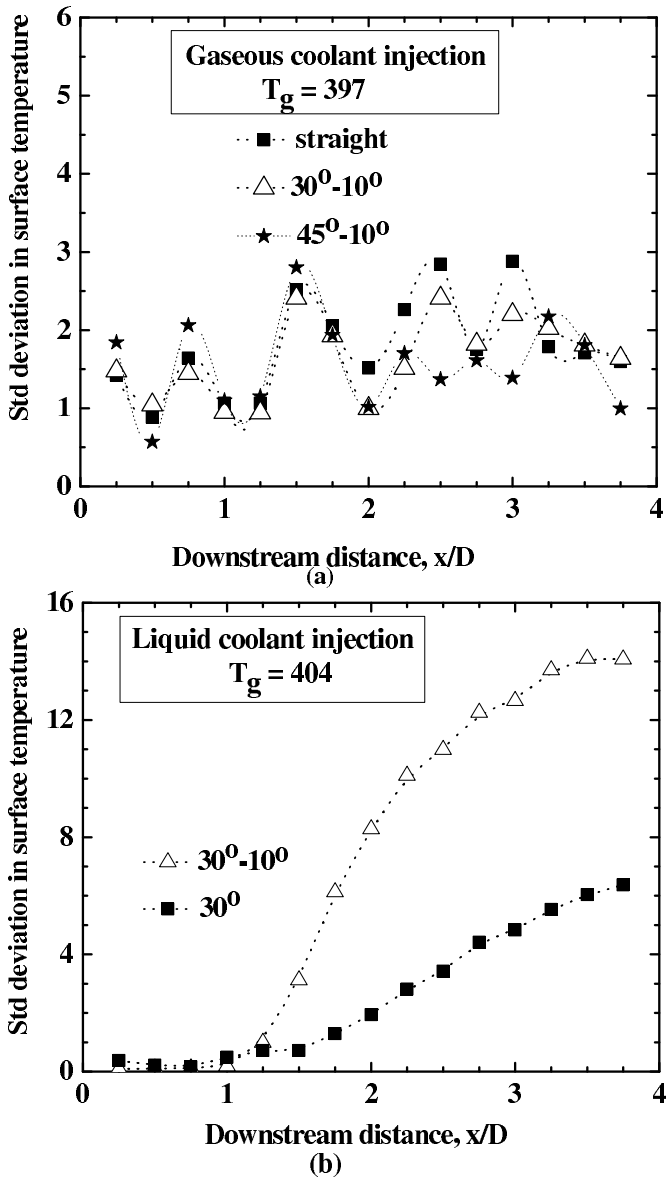

Figure 2.17: Film uniformity representation in terms of standard deviation in wall temperature for all injectors studied at an injection pressure of 1.5 bar. (a) gaseous coolant and (b) liquid coolant

similar in nature for both liquid and gaseous injection. Film effectiveness is highest at low core gas temperature and higher coolant injection pressure conditions. A weak dependence of film cooling effectiveness on core gas temperature is noted at low coolant injection pressures. These characteristics are not observed with the gaseous straight injector and the 30° tangential liquid injector (Fig.2.19c and 2.19d). One general observation is that the jets with high pressure provide high film cooling effectiveness for both the coolants.

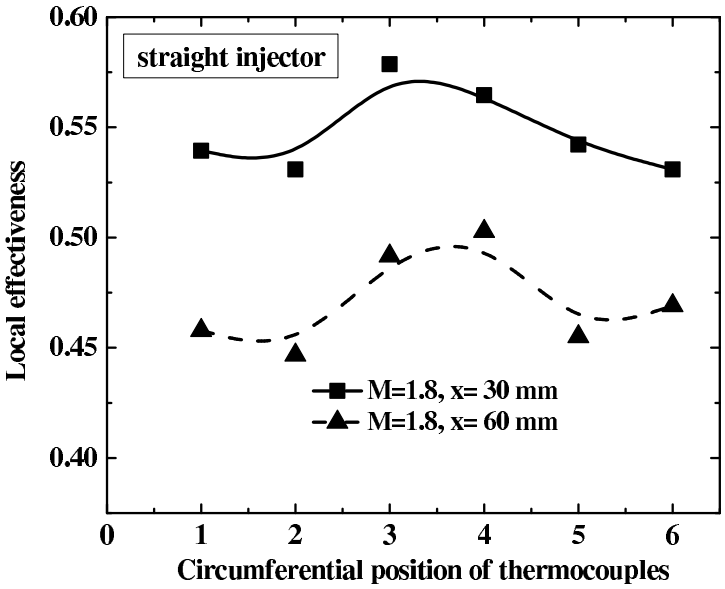

Figure 2.18: Local effectiveness values for the straight injector at two axial locations for the straight injector

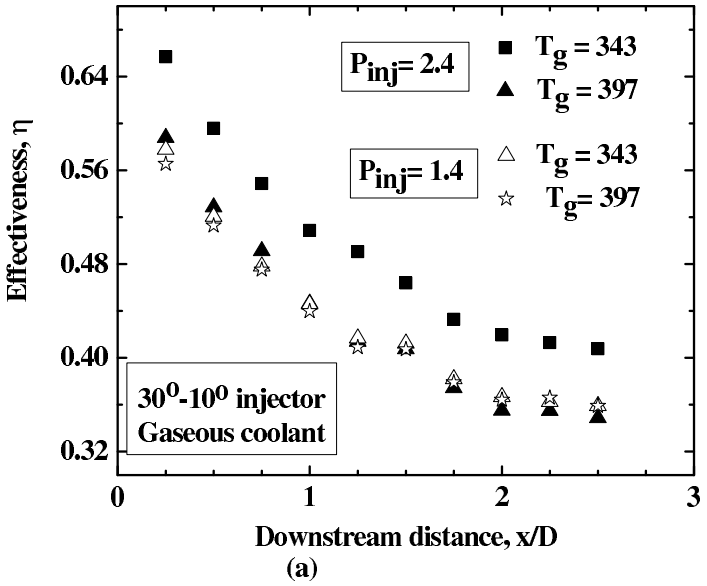

2.8 Conclusions

Circumferentially and span-wise averaged magnitudes of film cooling effectiveness and film uniformity parameters are described for internal flow from the measurements downstream of straight, tangential and compound angle film coolant injector holes. Straight and compound angle injection at two different configurations of 30°-10° and 450°-10° are investigated in the gaseous film cooling experiments using nitrogen. Tan-

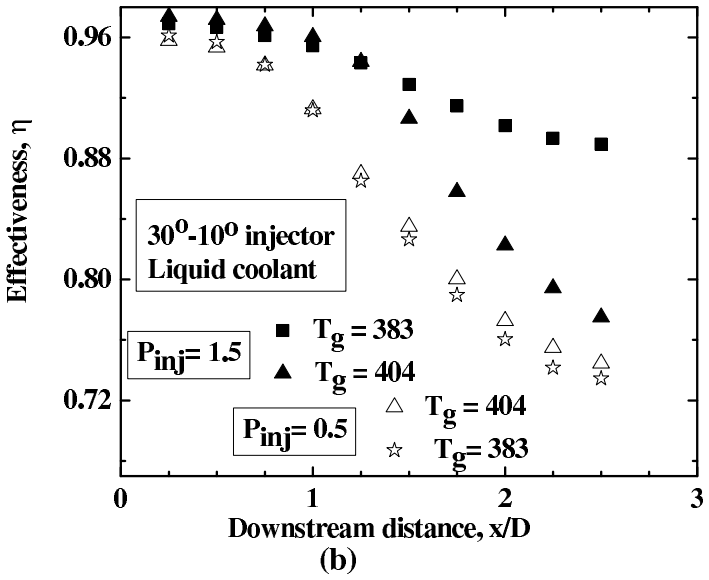

(b)

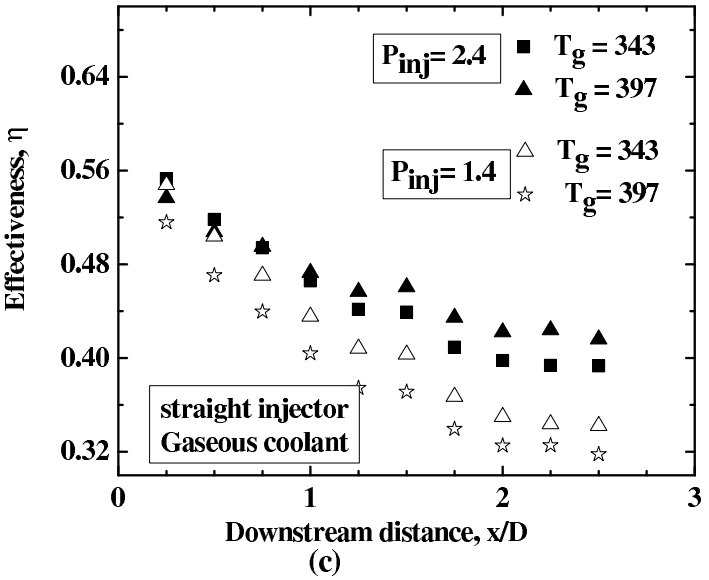

(c)

gential injection at 30° and compound angle injection at 30°-10° are examined in the liquid film cooling experiments using water. During the experiments, the blowing ratio was varied in the range of 1.8 to 3.9 in the case of gaseous film experiments by varying the coolant injection pressure from 1.3 to 2.4 bar (gauge). The coolant injection pressure varied from 0.25 to 1.5 bar for the liquid film experiments. Important conclusions drawn from this work include:

- All gaseous film configurations showed similar film-cooling effectiveness at low momentum flux ratios. But at relatively high momentum flux ratio, compound angle holes had significantly greater effectiveness than the base line case.

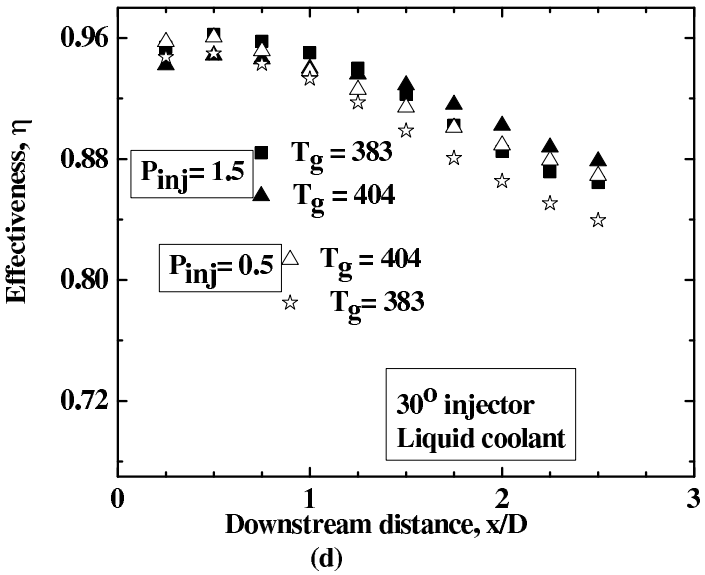

Figure 2.19: Circumferentially averaged effectiveness along the test section at different coolant injection pressures and core gas temperatures for various coolant injectors a) 30°-10°, gas, (b) 30°-10°, liquid, (c) straight, gas and (d) 30°, liquid

- Higher film cooling effectiveness prevailed for the compound injection orifice of 30°-10° compared to other configurations including that of 45°-10° suggesting that an optimum compound injection angle do persist maximizing the film cooling effectiveness.

- In the case of liquid film injection, adding a compound angle produced improvement in effectiveness close to the injection point i.e., for x/D < 0.75. At higher x/D ratios, tangential injection has the advantage of improved effectiveness. This indicates longer liquid film length for tangential injector compared to the compound angle injector. Effectiveness of tangential injector is little affected by the changes in core gas temperature whereas the compound angle injector is showing a notable reduction in effectiveness at higher core gas temperature.

- For all cases investigated, variation in temperature around the circumference is minimum at regions near to the injection points and becomes significant away from the coolant injection locations.

- Film cooling effectiveness increases with the coolant injection pressure for gaseous

and liquid coolants. The drop in effectiveness along the test section is less for the liquid injection at high coolant injection pressures.

- It was noted that a relatively stable film prevails for low core gas temperature and higher injection pressure tends to reduce the film uniformity.

CHAPTER 3

SIMULATION I: GASEOUS FILM COOLING WITH STRAIGHT INJECTION

In this chapter, the gaseous coolant injection using the straight injector is studied by solving the governing equations numerically. The details of the numerical model developed are described along with the solution procedure. Grid independence study and experimental validation are performed. The results of the different coolant injection cases studied are also discussed. Note that the contents of this chapter is based on Shine et al. (2012b).

3.1 Purpose

Literature survey has revealed that the film cooling performance is mainly affected by various parameters such as blowing ratio, curvature of the wall, geometry of the coolant hole, free-stream turbulence and core gas Reynolds number. It is also noted that the film cooling performance of straight cylindrical coolant holes in a circular pipe has not been properly characterized in previous studies. Therefore, simulations are done to document all the pertinent flow physics associated with the film cooling flow field of straight cylindrical coolant holes. 3-dimensional multi-species computational model using finite volume formulation has been developed and validated against the experimental data. Results provide valuable insight into the film cooling performance and the heat transfer characteristics associated with this type of film cooling jets. The purpose of this study can be summarized as follows.

- Highlight all prominent flow mechanisms downstream of film coolant injection.

- Describe the effect of various geometric parameters, blowing ratio and free-stream turbulence on film cooling behavior.
- Predict the film cooling effectiveness for adiabatic and conjugate heat transfer models.

3.2 Details of Numerical Simulation

A 3-dimensional multi-species numerical model, developed using commercial computational fluid dynamics (CFD) software ANSYS FLUENT 13.0.0, is used to predict film cooling effectiveness downstream of the coolant exit. The details of geometry, boundary conditions and the grid are described below, followed by the governing equations and solution methodology.

3.2.1 Geometry, boundary conditions and the grid

The geometry of the present computational model is based on the test set up used for validation. Sufficient length for the approach section is provided to ensure that the boundary conditions do not artificially affect the flow approaching the test section. A length of 60d is provided for the approach section and has a diameter of 108 mm similar to experimental conditions. The test section is having 120 mm inside diameter and the coolant holes are located at a pitch circle diameter of 114.5mm. A test section length of 240 mm is chosen because it can satisfy the simulation objective with a minimum computational time. The details are shown in Fig.3.2. Other geometric parameters are described in Table 3.1. It summarizes all cases considered for the computational analysis with Case-0 representing the experimental geometry. Geometries with dimensions mentioned in Case-1 and 2 are used for simulating the various cases of expansion ratios for the straight injector. Similarly Case-3 and 4 are used for simulating different coolant hole diameters, whereas Case-5 and 6 are for simulating different hole spacing. For accurate representation of coolant jet interaction, the coolant holes, the inlet region of hot core gas and the film cooled test section are

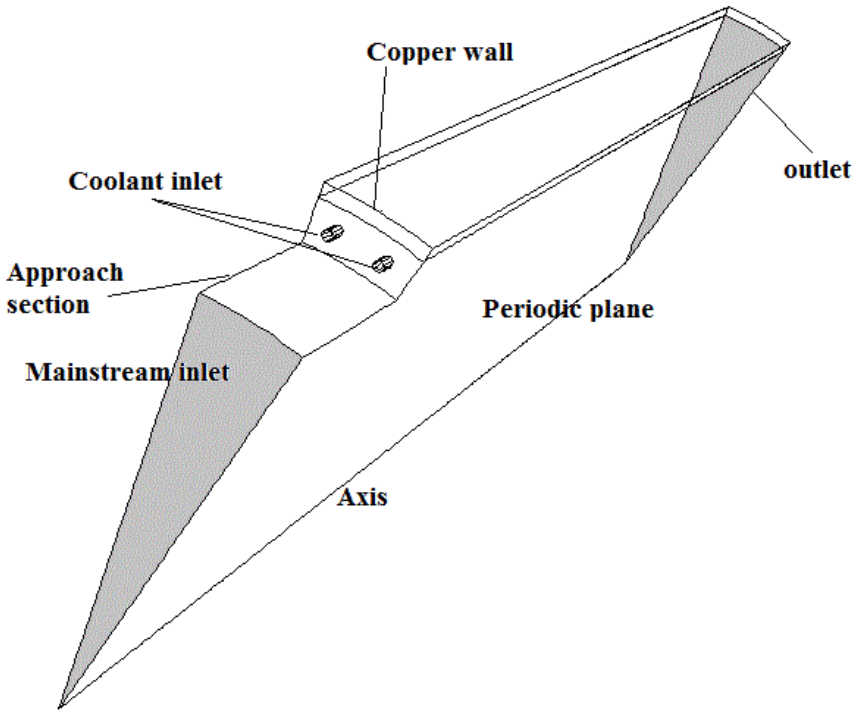

Figure 3.1: Schematic of the overall computational domain

modeled simultaneously. Schematic of the present computational domain is shown in Fig. 3.1. Since the experimental geometry has a periodicity between coolant holes, a sector containing two coolant holes is only considered for computations. The boundaries are defined from experimental conditions. Pressure inlet condition is applied at mainstream inlet and coolant inlet zones. Outflow boundary condition is applied at the outlet. Rotational periodicity with no pressure loss boundary condition is specified at both side faces. Though turbulence intensity levels are not measured during the experiment, an approximation for the computational model based on the equation, $Tu = Re^{\frac{-1}{8}}$ is used. The boundary conditions used at the mainstream and coolant inlet are summarized in Table 3.2. The interface between fluid and solid is specified as a coupled boundary, which avoided the use of the film cooling heat transfer boundary condition and allows a direct calculation of the heat transfer and wall temperature. The physical domain is separated into fluid and solid blocks by the wall. Copper wall with combined external convection and radiation boundary conditions at outer surface is modeled to simulate the experimental condition. Natural convection heat transfer coefficient of 4 $\mathrm{Wm^{-2}K^{-1}}$ calculated based on Churchil and Cho's correlations are

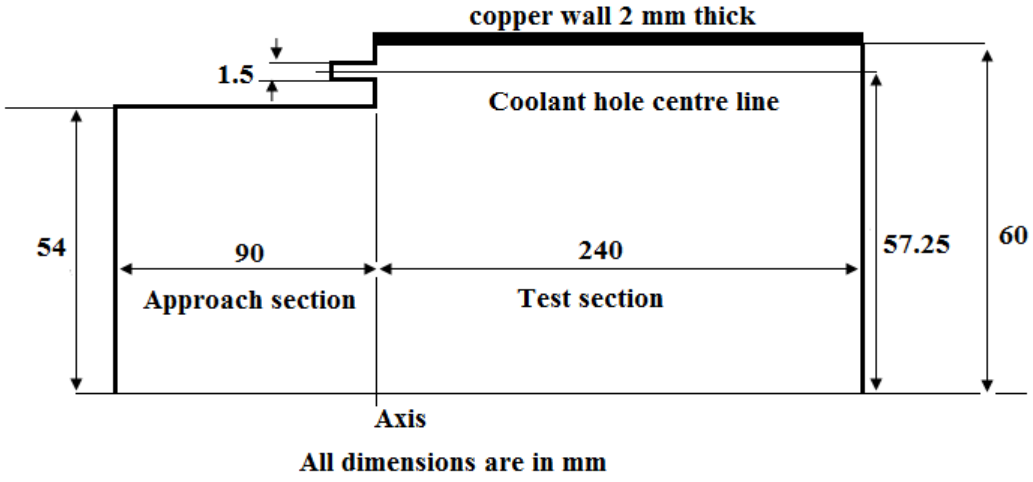

Figure 3.2: Dimensions of the computational domain

Table 3.1: Summary of cases simulated

Case No	D	d	D_1	H	β	No of holes around circumference	Hole pitch diameter, mm
0	120	1.5	108	6	7.2	50	114.5
1	120	1.5	102	9	7.2	50	114.5
2	120	1.5	96	12	7.2	50	114.5
3	120	1	108	6	7.2	50	114.5
4	120	2	108	6	7.2	50	114.5
5	120	1.5	108	6	6	60	114.5
6	120	1.5	108	6	8	45	114.5

used in the calculation of average heat transfer coefficient over the entire circumference. An emissivity value of 0.02 for the copper surface and the ambient temperature of 300 K is assumed for all computations. Values of specific heats, viscosities and thermal conductivities of individual gases are calculated using polynomial functions of temperature (Appendix A.1). The specific heats, viscosity and thermal conductivity are weighted by the mass fractions of species to obtain mixture values.

Structured and unstructured grids with hexahedral type are employed in the study to provide the highest grid quality. The grids are designed to be intensive, with high quality to capture the interaction and jet characteristics. The grid size for the current

Table 3.2: Boundary conditions at the test section inlet

		Straight injector
Mainstream inlet	Mass flow rate, kg s^{-1}	0.083-0.14
	Turbulence Intensity, %	4
	Hydraulic diameter, m	0.108
Coolant inlet	Pressure inlet, Pa	900-2700
	Turbulence Intensity, %	6
	Hydraulic diameter, m	0.0015

simulation is approximately 24×10^5 cells.

3.2.2 Governing equations with solution methodology

The mathematical model consists of conservation equations of each component species. Nitrogen gas and hot air are considered as coolant and core gas species for modelling gaseous film cooling process. The local mass fraction of each species is predicted through the solution of a convection-diffusion equation for the i^{th} species. The equation for conservation of mass is

$$\frac{\partial\left(\rho Y_i\right)}{\partial t}+\nabla.\left(\rho\vec{V}Y_i\right)=-\nabla.\vec{J_i} \tag{3.1}$$

where Y_i is the mass fraction and $\vec{J_i}$ the diffusion flux arises out of concentration gradients of species i.

$$\vec{J_i}=-\left(\rho D_{i,m}+\frac{\mu_t}{Sc_t}\right)\nabla Y_i \tag{3.2}$$

Sc_t is the turbulent Schmidt number and is taken as 0.7 as Yimer et al. (2002) has recommended this value for use in CFD applications involving axisymmetric free-jet flows. $D_{i,m}$ is the diffusion coefficient for species 'i' in the mixture. The diffusion coefficient for the mixture of nitrogen and air is calculated using Chapmann and Enskog equation (Reid et al., 1977).

Turbulence modeling

Turbulent flows are characterized by small fluctuations of the velocity and pressure fields. These small scale fluctuations are computationally too expensive to resolve. Instead, the instantaneous Navier-Stokes (N-S) equations are time-averaged and two additional transport equations for the turbulent kinetic energy, k, and the turbulence dissipation rate, ϵ are used to model the small scale fluctuations which appear in the newly-added terms of the averaged N-S equations. Therefore k-ϵ models are also called two-equation models or Reynolds-averaged N-S (RANS) models. The computational time is greatly reduced by modeling the small scales of the turbulence. The RANS equations are written in the Cartesian tensor form as:
N-S Equations

$$\frac{\partial}{\partial t}\left(\rho U_i\right) + \frac{\partial}{\partial x_j}\left(\rho U_i U_j + \rho\overline{u_i' u_j'}\right) = -P_i + \frac{\partial}{\partial x_j}\left[\mu\left(\frac{\partial U_i}{\partial x_j} + \frac{\partial U_j}{\partial x_i}\right)\right] \tag{3.3}$$

where U_i and $u_i^{'}$ are the mean and fluctuating velocity components (i = 1,2,3); ρ and μ are the density and dynamic viscosity of the fluid; P_i is the pressure gradient; x_i represents the coordinate; and the additional terms, $\overline{\rho u_i' u_j'}$, represent the effects of the turbulence and are called the Reynolds stress tensor. In order to close the RANS equations, the Reynolds stresses are modeled inside the k-ϵ models in such a way as to include the effect of turbulence as an increased viscosity. Thus the eddy-viscosity model for the Reynolds stresses is introduced

$$-\rho\overline{u_i' u_j'} = \mu_t\left(\frac{\partial U_i}{\partial x_j} + \frac{\partial U_j}{\partial x_i}\right) - \frac{2}{3}\rho\delta_{ij}k \tag{3.4}$$

Here, k is the turbulent kinetic energy,

$$k = \frac{1}{2}\overline{u_i' u_j'} \tag{3.5}$$

and μ_t is defined as the eddy or turbulent viscosity that is related to the k and ϵ. In addition, two transport equations for the k and ϵ are added to the averaged N-S equations in all such models.

The standard k-ϵ model was first proposed by Launder and Spalding (1972). Both the model transport equations for k and ϵ can be derived from the exact N-S equations, while the derivation for the ϵ equation involves a great amount of physical reasoning. The standard k-ϵ model, in essence, is a high Reynolds number turbulence model. The k-ϵ turbulence model has been successfully applied for turbulence modeling a wide range of film cooling flows (Walters and Leylek (2000), McGovern and Leylek (2000), Hyams and Leylek (2000), Brittingham and Leylek (2000), Koc et al. (2006), Baheri et al. (2008), Li et al. (2009), etc.). Therefore, k-ϵ model is selected for the current simulation of gaseous film cooling flow. The additional transport equations for the turbulent kinetic energy 'k' and dissipation rate 'ϵ' used in the present study are

$$\frac{\partial}{\partial t}(\rho k) + \frac{\partial}{\partial x_i}(\rho U_i k) = \frac{\partial}{\partial x_j}\left[\left(\mu + \frac{\mu_t}{\sigma_k}\right)\frac{\partial k}{\partial x_j}\right] + G_k - \rho\epsilon \tag{3.6}$$

and

$$\frac{\partial}{\partial t}(\rho \epsilon) + \frac{\partial}{\partial x_i}(\rho U_i \epsilon) = \frac{\partial}{\partial x_j}\left[\left(\mu + \frac{\mu_t}{\sigma_\epsilon}\right)\frac{\partial \epsilon}{\partial x_j}\right] + C_{1\epsilon}\frac{\epsilon}{k}G_k - C_{2\epsilon}\rho\frac{\epsilon^2}{k} \tag{3.7}$$

G_k is the production of turbulent kinetic energy and is calculated as

$$G_k = -\rho\overline{u_i^{'}u_j^{'}}\frac{\partial U_j}{\partial x_i} \tag{3.8}$$

To evaluate G_k in a manner consistent with the Boussinesq hypothesis,

$$G_k = \mu_t S^2 \tag{3.9}$$

where S is the modulus of the mean rate-of-strain tensor, defined as

$$S = \sqrt{2S_{ij}S_{ij}} \tag{3.10}$$

The turbulent (or eddy) viscosity, μ_t, is computed by combining k and ϵ as

$$\mu_t = \rho C_\mu k^2/\epsilon \tag{3.11}$$

where C_μ is a constant.
σ_k and σ_ϵ are the turbulent Prandtl numbers for k and ϵ, respectively. The model constants $C_{1\epsilon}$, $C_{2\epsilon}$, C_μ, σ_k and σ_ϵ have the values 1.44, 1.92, 0.09, 1.0 and 1.3, respectively.

Near-Wall Treatment

The k-ϵ models are primarily valid for turbulent core flows, i.e., the flow in the regions sufficiently far from the walls. The near-wall flows are composed of three regions: a viscous sublayer region where molecular viscosity plays a dominant role in the flow transport phenomena, a buffer region where both turbulent and molecular viscosities play important roles, and a turbulent core region where the effect of molecular viscosity can be neglected. This is effectively accounted by using semi-empirical formulae called "wall functions". These are used to bridge the viscosity-affected region between the wall and the fully-turbulent region. The use of wall functions obviates the need to modify the turbulence models to account for the presence of the wall. The standard wall functions are based on the work of Launder and Spalding (1974), and have been most widely used in industrial flows. For the current simulation work, the above wall treatment method for the near-wall region is employed with the k-ϵ model.

Solution Algorithm

The segregated solver is chosen as the solution algorithm for the simulation work since the memory requirement for the coupled algorithm is more than the segregated algorithm. In this approach, the governing equations are solved sequentially and an iteration method is necessary due to the non-linearity of the governing equations. The solution steps of the segregated solver under steady state conditions are outlined below and are illustrated in Figure 3.3.

1. Fluid properties are calculated based on the current solutions (or assumed solutions at the start of the simulation process).

2. Each of the momentum equations for velocities (u, v, and w) are solved in turn using current values for pressure and face mass fluxes. Thus the velocity field is updated.

3. The pressure-correction equation is then solved to obtain corrected pressure and velocity fields.

4. The turbulence scalar equations for k and ϵ are solved using the previously updated values of the other variables.

5. Convergence of the equation set is then checked and on settlement, convergence calculations are stopped, if not, the steps 1-5 is repeated.

Discretization Methods

Control-volume approach is used to transform the governing equations into algebraic equations that can be solved numerically. This approach consists of integrating the differential governing equations over each control volume to yield discretized equations that conserve each quantity on a control-volume basis. Thus, discretization methods are needed for this process and details are given in this section. The discretization of the governing equations is performed using the second order upwind scheme.

Pressure-velocity coupling is achieved through the pressure-correction equation which is derived from the continuity and momentum equations. The semi-implicit method for pressure-linked equations [SIMPLE] algorithm was used to couple the pressure and velocity.

Discretization of equations: A discretized scalar governing equation for u, v, w, k or ϵ contains the unknown scalar variable φ at the centre point, P, and the unknown values φ in its surrounding neighbor volumes. Its linearized form can be written as

$$a_p \varphi_p = \sum_{nb} a_{nb} \varphi_{nb} + b \tag{3.12}$$

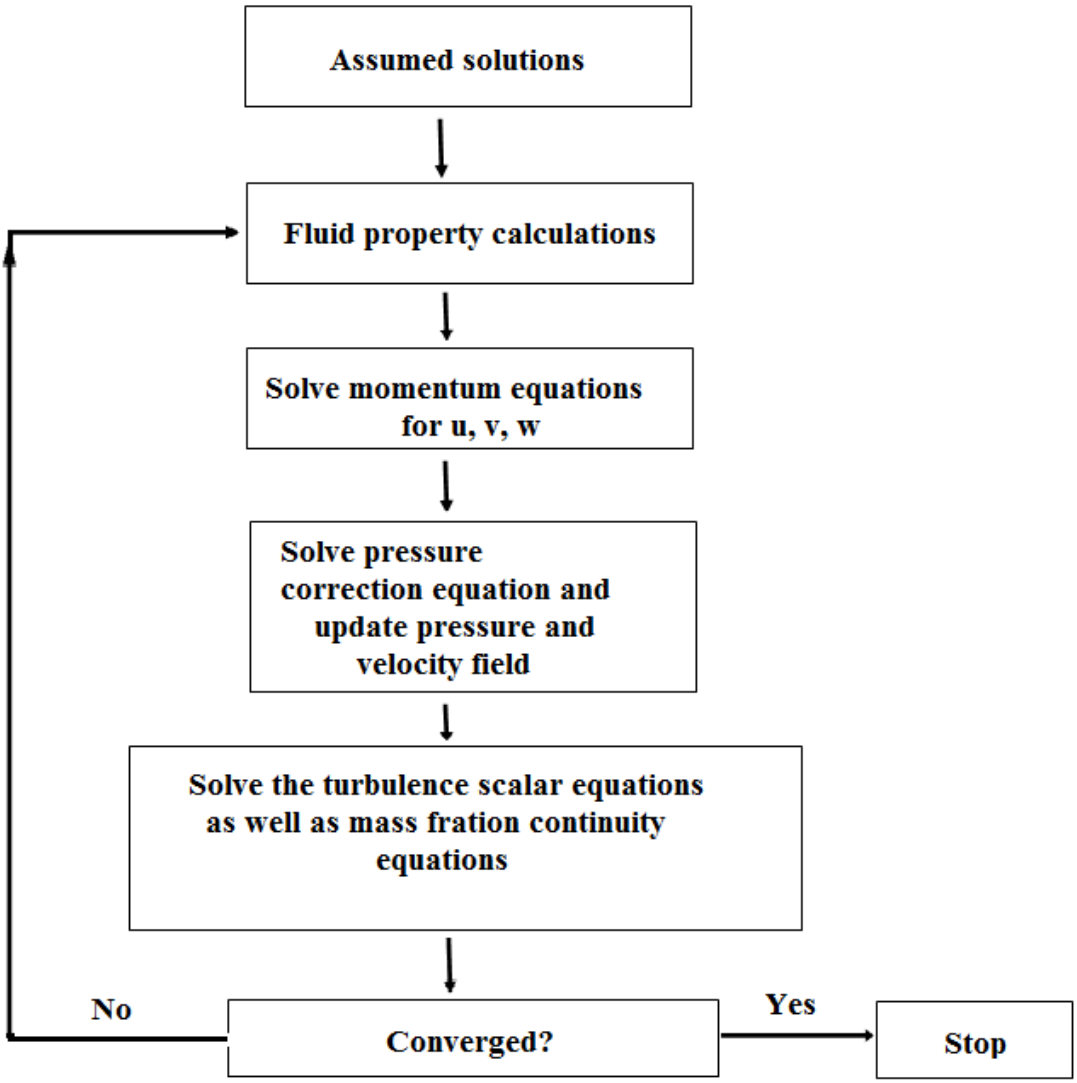

Figure 3.3: Solution steps of the segregated solver.

where a_p and a_{nb} are the linearized coefficients, and b is the source term. In general this equation is non-linear with respect to variables and hence iteration technique is necessary for its solution.

Solution Convergence

Convergence is established based on overall mass and energy imbalance within the domain of less than 0.001% and on reduction of scaled residuals six orders of magnitude. At the end of each iteration, the residual sum for each of the conserved variables is computed and compared with the convergence criterion. The residual sum is the sum of absolute values of the residual for each control volume. The residual is also normalized. Typically, 1500-2000 iterations are needed to obtain a converged result, which takes about 10-12 hours on a DELL Precision AW T550V workstation having Dual Quad Xeon E55220 processor with 72 GB DDR3.

3.2.3 Effectiveness

Due to the finite wall thickness and high thermal conductivity material used for fabricating the experimental test section, conjugate heat transfer models are used for comparing the results of different cases studied. A non-dimensional film-cooling effectiveness parameter $\eta(x/D)$, based on the wall outer surface temperature of the test section $T_{out}\,(x/D)$, is used to compare experimental and computational results. This parameter is selected based on the fact that, outside surface temperatures are measured in the film cooling experiments conducted. The film-cooling effectiveness η is defined by

$$\eta(x/D) = \frac{[T_{out}\,(x/D) - T_g]}{[T_c - T_g]} \tag{3.13}$$

η_{exp} and η_{comp} is calculated from the experimental and computational values of $T_{out}\,(x/D)$. As there were six thermocouples installed circumferentially at every axial location of the experimental test section, a circumferential average value of $T_{out}\,(x/D)$ is used to calculate η_{exp}.

To simulate the adiabatic case, adiabatic wall condition is directly imposed on the wall surface in contact with the gas. For this reason, a film-cooling effectiveness

parameter ϕ based on the inside surface temperature of the test section $T_{int}\,(x/D)$, is used for comparing adiabatic and conjugate wall cases. It is defined as follows.

$$\phi(x/D) = \frac{[T_{int}\,(x/D) - T_g]}{[T_c - T_g]} \tag{3.14}$$

ϕ_{AW} and ϕ_{conj} is calculated from the values of $T_{int}\,(x/D)$ obtained from the computational adiabatic and conjugate models.

3.2.4 Grid independence study

A grid convergence study is conducted to show that the numerical solution is independent of the grid used. It has been performed separately for each blowing ratio (M = 2.64, 3 and 3.63) with different grid densities. Different grid densities are made varying the resolution by a factor of about 2 between two consecutive grid levels. Four different grids are tested starting from a grid size of 12.4×10^5. Table 3.3 shows the grid sizes for different grids and the test section inside surface temperatures at three locations. The result of the grid independence analysis is given in Fig. 3.4 where change in film cooling effectiveness η_{comp} along the test section downstream of injection is illustrated for the different mesh sizes studied. It is clear that the results in the case of medium and fine grids are almost similar and solution becomes grid independent after medium grid. Hence medium grid is used for CFD simulation. The medium grid selected for simulation has a total size of 2,419,141 cells where the finest resolution is of the order of 8×10^{-4} D and located at the vicinity of the coolant hole downstream of injection. There are 42 grid nodes in the circumference around the coolant injection hole. The computation of the flow with film-cooling injection converged for every grid and coolant flow regime tested; residuals are 10^{-6} and stable. The rate of convergence is almost identical when computing with and without the presence of a cooling jet. This further ensures the robustness of all grid sizes tested.

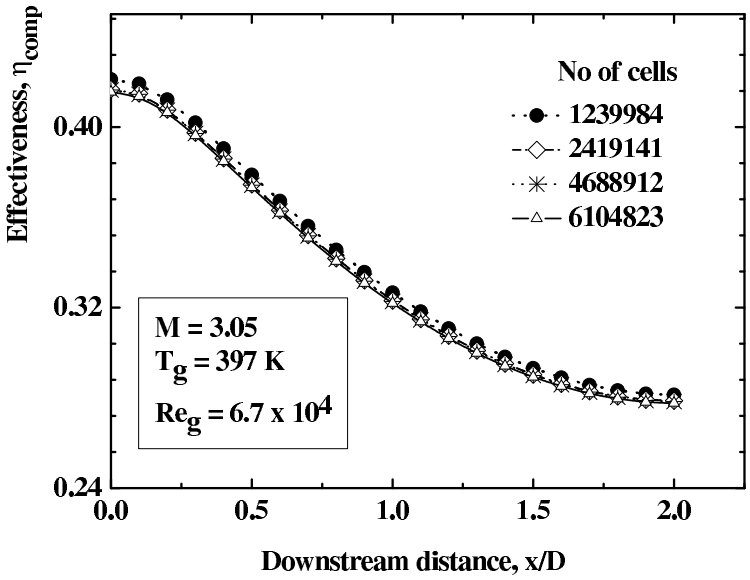

Figure 3.4: Grid sensitivity test for the straight injector

Table 3.3: Grid Independence study at Re = 6.7 x 10^4 and M= 3.05 using four consecutively refined grid levels

Grid level	No of cells	T_{int} x/D = 0.10	T_{int} x/D = 0.25	T_{int} at x/D = 0.50	% change in T_{int}
Coarse	1239984	356.52	357.7	360.5	-
Medium	2419141	356.94	358.11	360.86	0.09
	4688912	356.99	358.18	360.9	0.01
Fine	6104823	357.02	358.2	360.9	0

3.3 Results and Discussions

Figure 3.5 demonstrates the result of numerical simulation which is consistent with the experiments. Experiments conducted at various blowing ratios and core gas temperatures are used for comparison. These cover blowing ratios varying from 1.94 to 3.63, and ratio of coolant temperature to mainstream temperature varying from 0.73 to 0.84. The temperature of the coolant gas is kept at 300 K. Overall, the agreement between predicted and measured effectiveness is good. The global tendency is well predicted in all the cases. The deviations are attributed to higher estimated experimental uncertainty and difficulty in maintaining constant coolant temperature in the

experiment. Figure 3.6 shows the percentage deviation between one set of experimental and computational data. The maximum difference however, is about 8%. One general observation is that the error is progressively increasing in the downstream direction. A wall jet model for slot film cooling was proposed by Simon (1986) us-

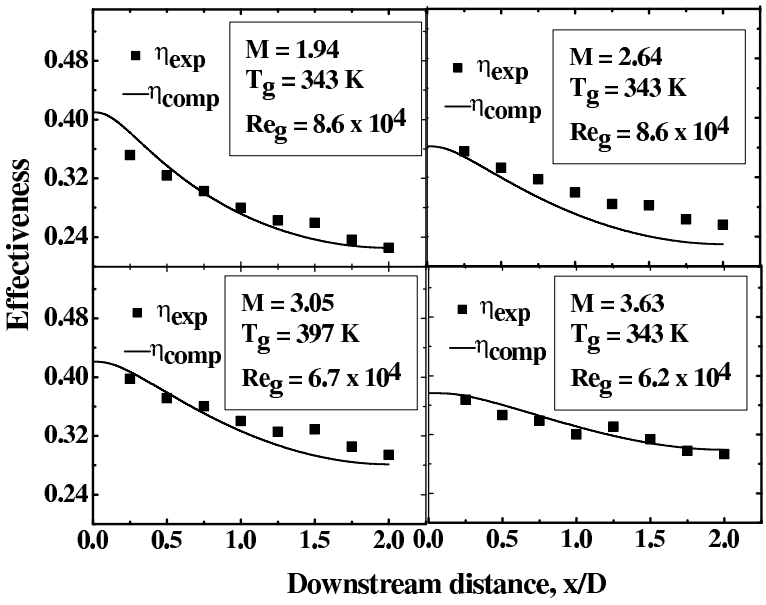

Figure 3.5: Comparison of computed η with experimental data

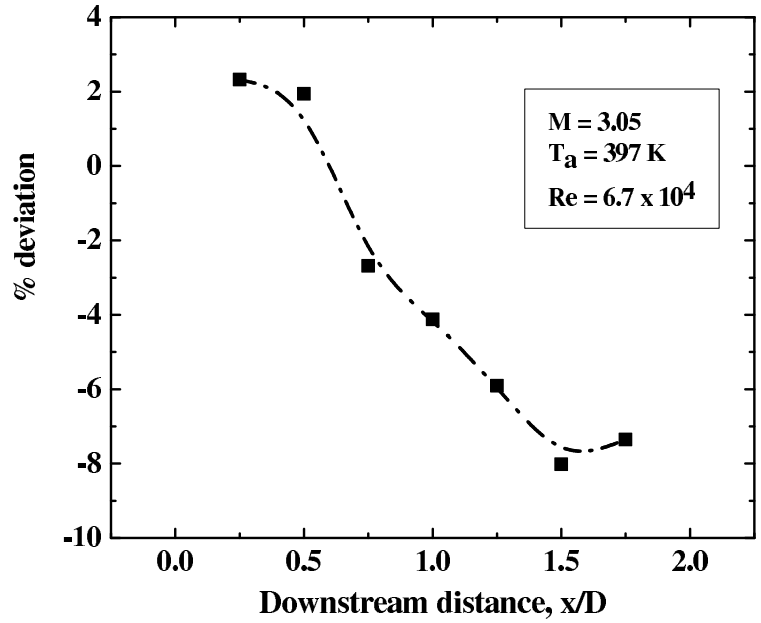

Figure 3.6: Deviation between experimental and computational data

ing adiabatic wall conditions. Equations were developed for predicting adiabatic film

cooling effectiveness under conditions of variable turbulence intensity, flow and temperature. Therefore, adiabatic film cooling effectiveness, generated from the present numerical model is compared with Simon's model in Fig. 3.7. The values predicted using Simon's model (Simon, 1986) are considerably higher. There are two main reasons for this behaviour. (i) The coolant exposed to the mainstream has a width equal to the coolant diameter and this causes increased dispersion of the coolant. (ii) Simon has considered the jet moving along the wall. Moreover the model was proposed for low blowing ratios whereas the present experiments are conducted at higher blowing ratios. The figure also shows comparison with the model proposed by Arnold et al. (2009b). It is observed that the current computational predictions show similar trends with those obtained from Arnold et al.'s (Arnold et al., 2009b) model. Arnold's empirical model was for regenerative and film-cooled high-pressure rocket combustion chambers with tangential slot injection.

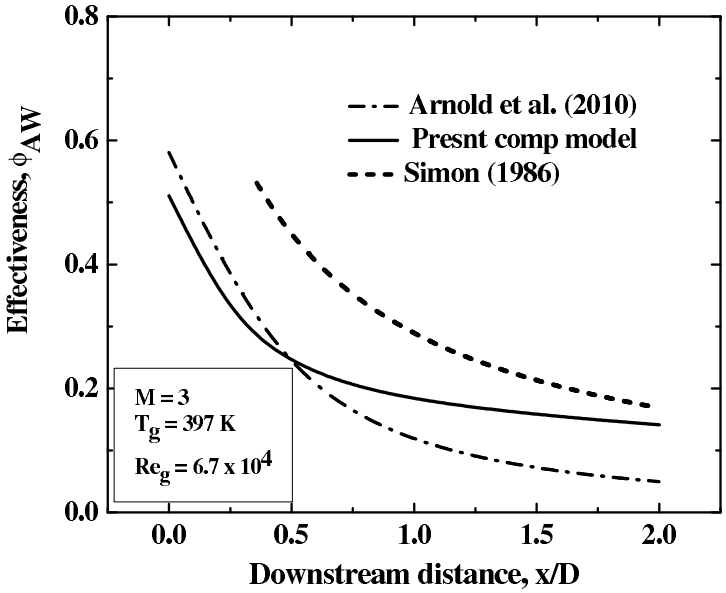

Figure 3.7: Comparison of adiabatic effectiveness values with other empirical models

3.3.1 Velocity fields

This section presents the flow field results downstream of film coolant injection. Three different computational images illustrating axial velocity contours, tangential velocity vectors and vorticity contours are shown.

Velocity field downstream of injection

Contours of normalized axial velocity and tangential velocity vectors at 5 mm downstream of coolant injection are shown in Fig. 3.8 (a). The coolant jet forms a counter rotating vortex structure. This drags more mainstream fluid near the wall and has a detrimental effect on the film cooling effectiveness. The strength of the vortices changes with blowing ratio and results in changes in the film-cooling performance.

Vorticity contours in a plane parallel to the circumferential wall

Normalized vorticity contours (normalization done with the maximum vorticity levels present) in a plane parallel to the circumferential wall and passing through the coolant hole center is shown in Fig.3.8(b). The source of the counter rotating vortices can be identified as the vorticity contained in the film-hole boundary layers. The vorticity pockets are diffused as the jet moves downstream.

Velocity vectors showing the general flow features downstream of injection

The velocity vectors demonstrating the flow features downstream of injection along the stream wise direction is shown in Fig. 3.8 (c). The jet impingement on the wall is observed. A reverse flow region is being developed from the rebound of the jet. These effects cause an increased local heat transfer coefficient and net heat flux in these regions. The temperature contours downstream of coolant injection along the stream wise direction is also shown in Fig.3.9.

3.3.2 Adiabatic and conjugate cooling effectiveness

The coupling of heat transfer in the fluid with heat conduction across the chamber wall is important for rocket combustion chamber applications and thus presents a conjugate heat transfer condition. To compare film cooling effectiveness under adiabatic

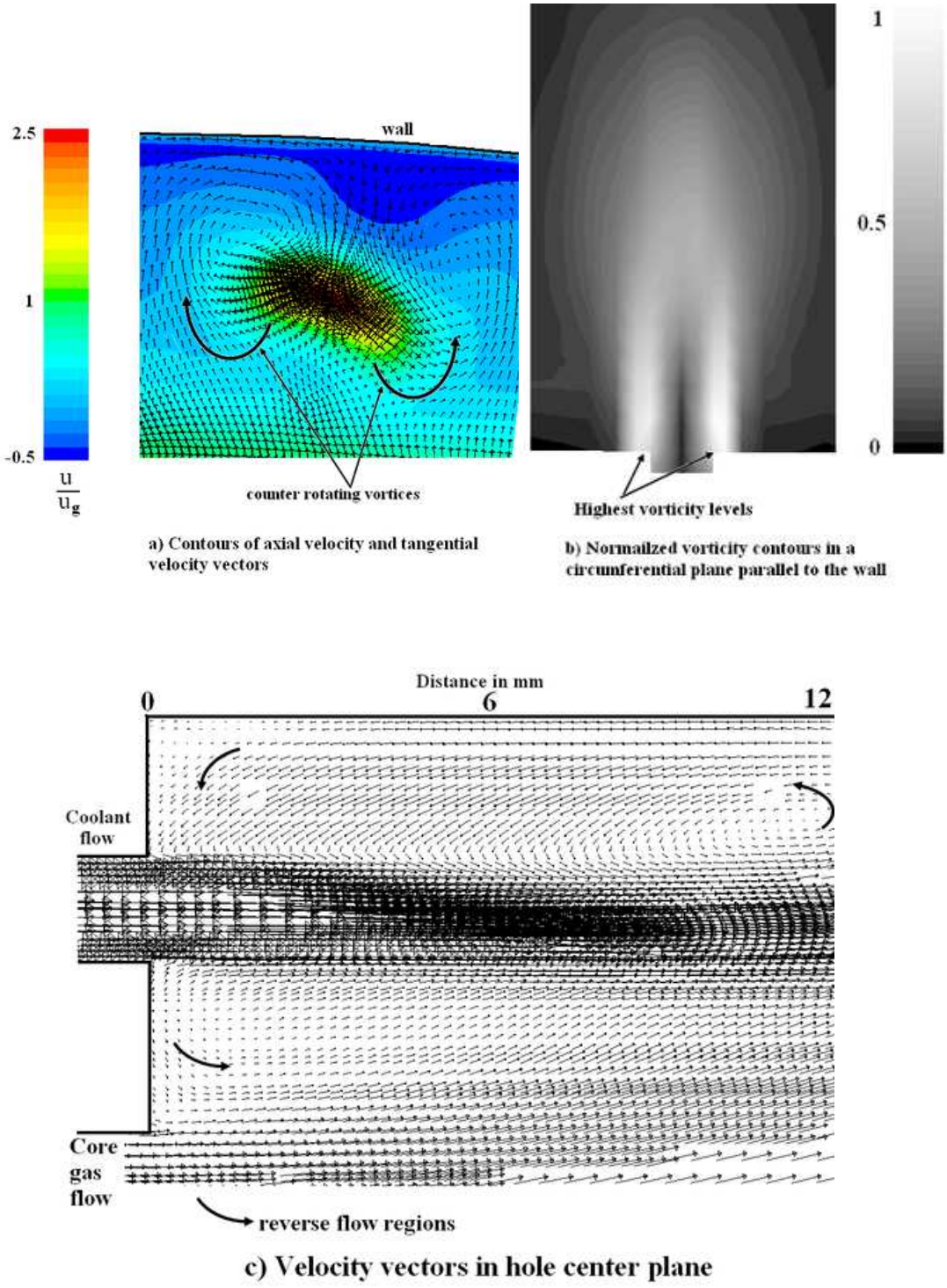

Figure 3.8: Flow field results in three different planes

and conjugate heat transfer conditions, numerical analysis is performed for two different heat transfer conditions at the solid-fluid interface. The conjugate case uses a coupled wall condition at the solid-liquid interface which allows a direct calculation

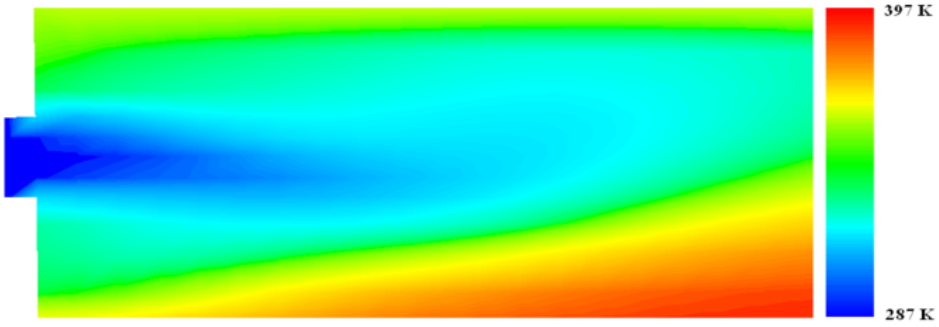

Figure 3.9: Temperature contours downstream of coolant injection

of the heat transfer and wall temperatures. Combined external convection and radiation boundary condition are used at the outer surface of the chamber wall. Figure 3.10 shows the variation of η_{exp}, η_{comp}, ϕ_{AW} and ϕ_{conj} along the axial length for two different test cases. The closeness of η_{comp} and ϕ_{conj} is due to the thin high conductivity wall material used in computational model (2mm thick copper). The effectiveness distribution for the conjugate case is significantly different from the adiabatic case. The high ϕ_{conj} observed far downstream of the injection point is attributed to the high thermal conductivity material and the convective heat transfer at the wall. Similar qualitative behavior of ϕ_{AW} and ϕ_{conj} was observed by Silieti et al. (2009), Weiguo et al. (2012), and Ghorab (2011), even though their computational geometry was entirely different from the present case. In the vicinity of coolant injection, conjugate wall effectiveness is low compared to adiabatic wall. This is due to the conduction effect through the wall. Heat transfer from the hotter downstream region subdues the internal cooling effect in this region. Similar trends for η_{exp}, η_{comp} and ϕ_{conj} brings out the importance of including the chamber wall in computational analysis of film-cooling studies in cylindrical combustion chambers.

A regeneratively cooled rocket combustion chamber is similar to a high conductivity wall. The improvement in far field effectiveness obtained in the present study using a high conductivity material shows that film cooling combined with regenerative cooling will be a very good option for protecting the entire length of rocket combustion chambers. To investigate the effect of thermal conductivity of the conjugate wall, simulations were done with different values of conductivity. Figure 3.11 presents the

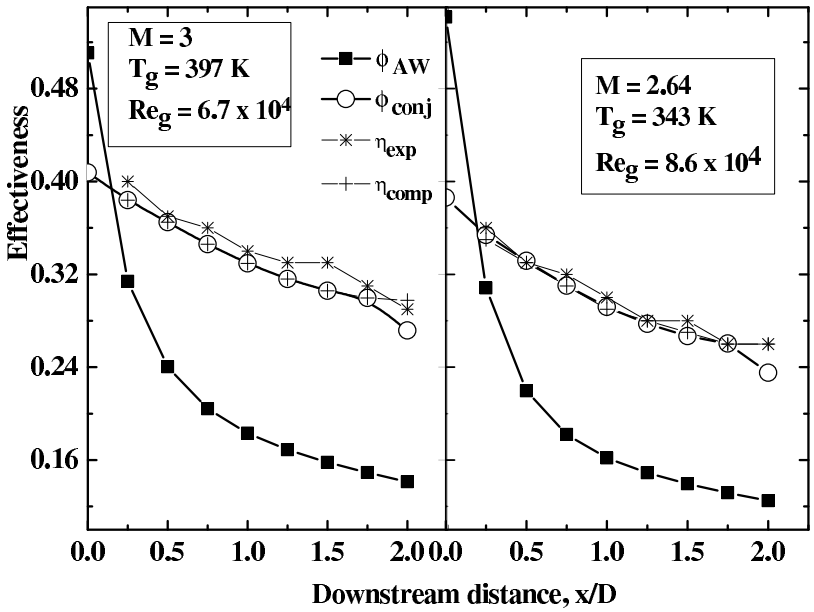

Figure 3.10: Comparison of the predicted ϕ_{AW}, ϕ_{conj}, and η_{comp} with the experimental data η_{exp}

inside surface temperature distribution for the conjugate walls with different 'k' values and for the adiabatic case. Temperature variation along the axial length is different for the conjugate walls indicating wall conduction effects in the axial direction. The local heat flux at the fluid-solid interface is plotted against normalized axial distance in Fig. 3.12. A negative heat flux indicating reverse heat transfer from the wall to the coolant is evident for high conductivity walls in the near coolant injection region. Span of this negative heat transfer region is found increasing with increase in conductivity. The heat transfer through the solid wall from the hotter downstream to the cooler upstream region creates an increase in the solid-fluid interface temperature and reverse heat transfer in the near injection region. Due to this coolant heating, inside surface temperatures are higher for the high conductive walls as seen in Fig. 3.11. A qualitative illustration of the heat transfer scenario with highly conductive wall is shown in Fig. 3.13. Lowest surface temperatures, in the neighborhood of injection, are obtained for the case of wall made of low thermal conductivity material. A peak in surface heat flux is noted in the near coolant-injection region for all cases. This is due to the variation in heat transfer coefficient in these regions created by the sudden expansion of pipe.

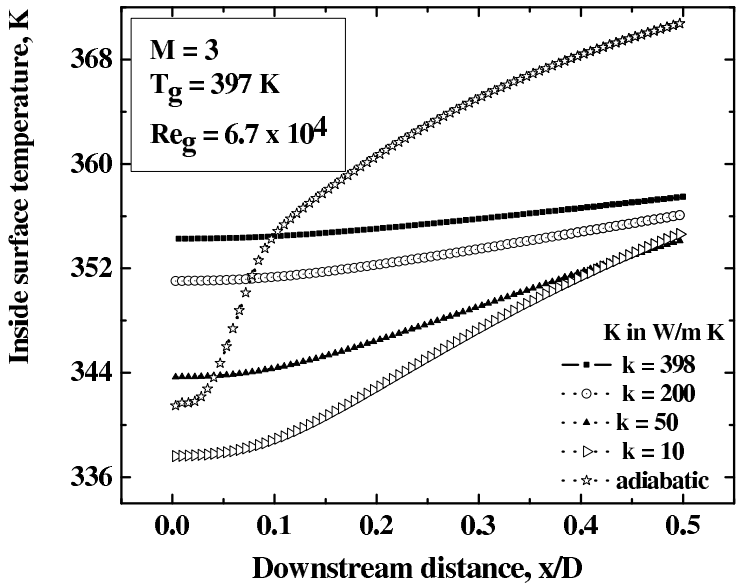

Figure 3.11: Wall inner surface temperature variation for walls with different thermal conductivities

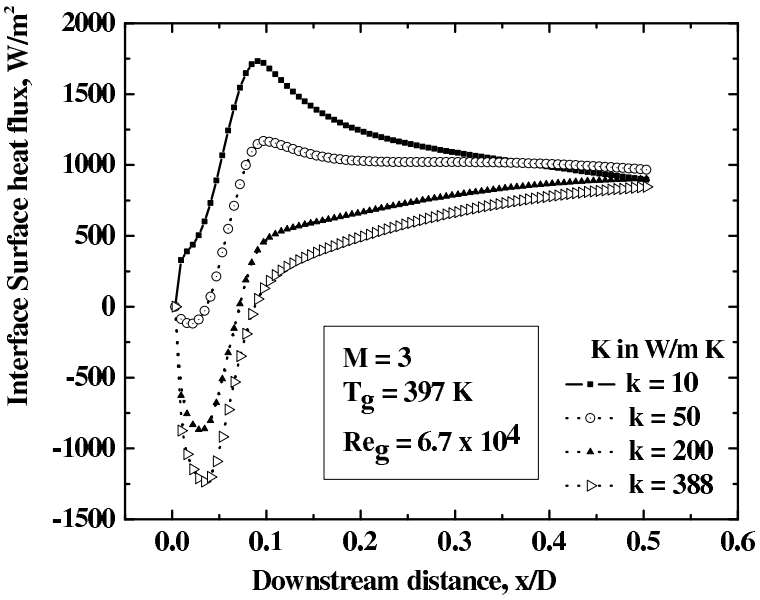

Figure 3.12: Interface surface heat flux variation for walls with different thermal conductivities

3.3.3 Effect of blowing ratio

Figure 3.14 shows how η_{comp} vary with normalized axial distance for different blowing ratios. The simulations are done for experimental conditions mentioned corresponding to M = 3. As blowing ratio increases, overall effectiveness across the test section also

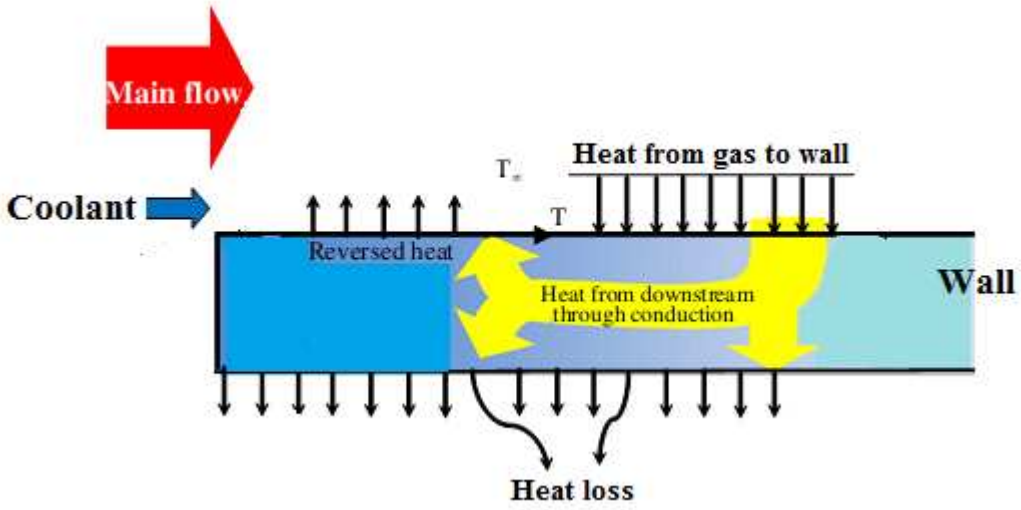

Figure 3.13: A qualitative illustration of heat transfer scenario showing reversed heat transfer associated with high conductive wall

increases in the vicinity of film coolant injection up to M = 3.5. However, beyond M = 3.5, a drop in effectiveness is noted. To compare this phenomenon over a full range of blowing ratios, spatially averaged effectiveness $\overline{\overline{\eta}}_{comp}$ values are plotted as shown in Fig. 3.15. Spatially averaged effectiveness is defined as the integral average of the effectiveness along the axial direction. At higher blowing ratios, the effectiveness values beyond x/D = 1.25 shows negligible variation. Due to this, $\overline{\overline{\eta}}_{comp}$ is calculated for a distance of 150 mm (x/D = 1.25) downstream of the film coolant injection. It is seen that the highest magnitudes of $\overline{\overline{\eta}}_{comp}$ are obtained for blowing ratios around 3.5. It can be concluded that an optimum blowing ratio exists and is around 3.5 for the present conditions. These results are qualitatively consistent with the observations made by Schmidt et al. (1996) and Bell et al. (2000) for compound angle coolant injection on a flat plate.

The wall-normal vorticity values along a line passing through the coolant hole centers in three different planes (planes perpendicular to the axis) i.e., at the hole exit and the axial cutting planes at a distance of 5 and 10 mm from the coolant injection point, for different blowing ratios are shown in Fig. 3.16. The vorticity contained in the film holes is found to increase with blowing ratio. The vorticity level degrades rapidly and is about 10% of its initial value at 5 mm downstream of coolant exit. The degradation in vorticity is mainly due to counteracting vorticity produced at the jet-mainstream in-

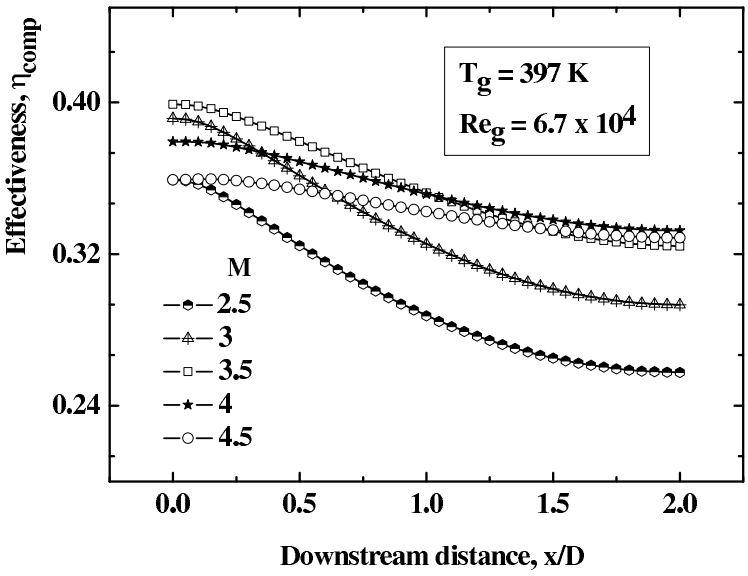

Figure 3.14: Variation of circumferentially averaged effectiveness η_{comp} along the test section for various blowing ratios

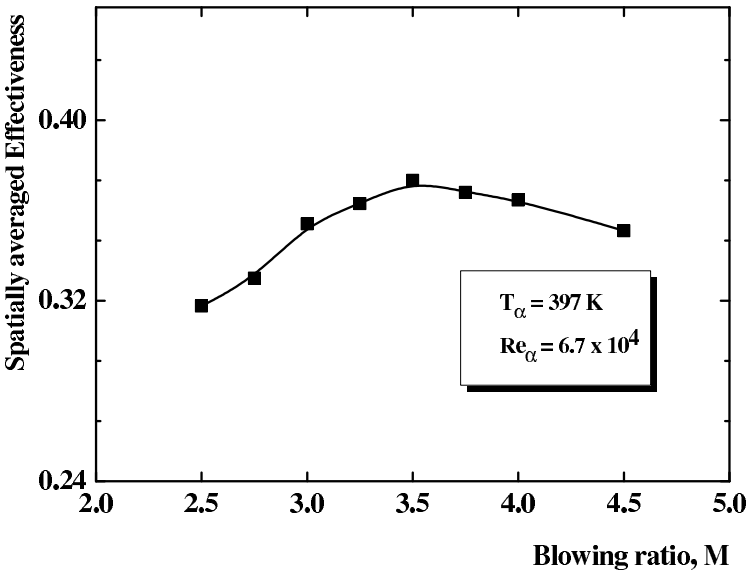

Figure 3.15: Spatially averaged effectiveness $\overline{\overline{\eta}}_{comp}$ with blowing ratio.

terface. Since the mainstream flow velocities are constant, the counteracting vorticity levels are expected to be similar. This is evident from the fact that the magnitude of destruction of vorticity is almost similar for all blowing ratios. Maximum turbulence intensity levels at various locations downstream of coolant injection are compared in Table 3.4. Comparison is done with respect to maximum turbulence intensity existing at the hole exit of M = 2.5. The turbulence is being generated at the shear layer

between the mainstream and the coolant jet and also in the separation region near the hole exit plane. As blowing ratio increases, the turbulence production within the film hole increases. At higher blowing ratios, increased mismatch between the coolant and mainstream momentum results in increased turbulence. Thus higher blowing ratios (M>3.5) are characterized by high turbulence and high vorticity levels. In these conditions, more mainstream fluid is dragged towards the wall and results in an effectiveness drop in the neighborhood of injection. It can be concluded that the film cooling performance at different blowing ratios are affected by the vorticity produced at the coolant hole boundary layers, vorticity produced by the shearing of coolant jet and mainstream, the turbulence generated, the exit momentum of the coolant jet and the associated flow structure.

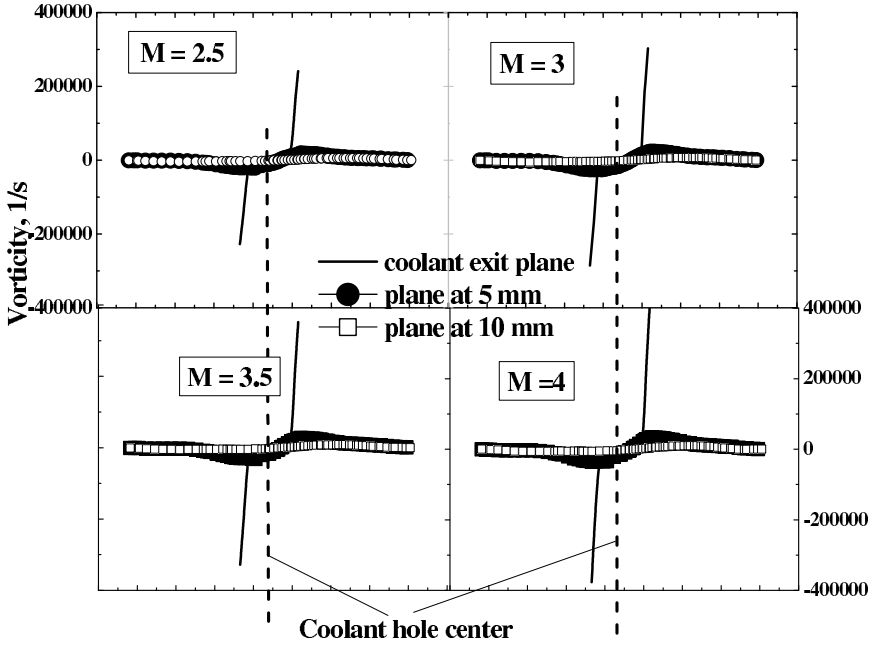

Figure 3.16: Radial vorticity levels across coolant hole in different planes perpendicular to the axis downstream of coolant injection

3.3.4 Effect of expansion ratio

Figure 3.17 represents the effect of changes in expansion ratio, ER, on film cooling effectiveness. The different values of ER are selected based on the fact that computa-

Table 3.4: Comparison of turbulence levels at different blowing ratios

	Maximum turbulence intensity levels in % compared to the hole exit plane of M = 2.5		
Blowing Ratio, M Ratio, M	At the hole exit	5 mm downstream of coolant injection	10 mm downstream of coolant injection
2.5	100	164	117
3	115	197	145
3.5	124	220	168
4	134	240	196

tional results are available for similar expansion ratios for flows adjacent to backward-facing step. As can be seen from the figure, the decrease in η_{comp} is larger for the expansion ratio (ER) of 1.25 for both blowing ratios in comparison with the experimental geometry (ER = 1.1). The behavior of turbulence intensity levels is first examined to investigate this phenomenon. Abu-Mulaweh et al. (2002) has pointed out that an increase in step height leads to an increase in turbulence intensity. In the near region of coolant injection, present simulation showed 20% increase in turbulence intensity levels when ER increased from 1.1 to 1.25. The abrupt expansion of the test section produces a backward facing step flow. The step height is the difference between the test section height downstream of the step and the upstream height. The reverse and swirling flow regions developed adjacent to the step and its impingement increases the turbulence downstream of the step. The variation in turbulence intensity showed similar trends as that observed with Nusselt number. Figure 3.18 illustrates the effect of step height on local Nusselt number. The increase in turbulence intensity is causing an increase in Nusselt number. The location of peak Nu moves away from the step as the step height increases due to the larger re-attachment length (Chen et al., 2006). The high turbulence generated at high expansion ratios results in more mixing of the mainstream fluid and the coolant maximum vorticity levels decreased to 33% of its initial value within 5 mm of the hole exit for ER of 1.1. But this was only 50% in case of ER = 1.25. These effects have resulted in poor effectiveness values at ER = 1.25. Lowest metal temperature is obtained at the corner and adjacent to the coolant jet because of the presence of jet and low mainstream convection flow in that region.

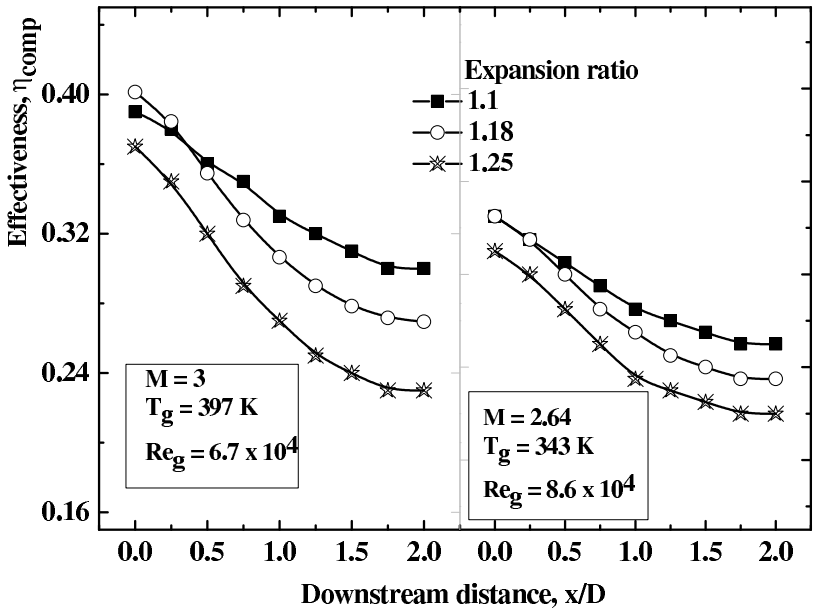

Figure 3.17: Variation along the axial length at different expansion ratios.

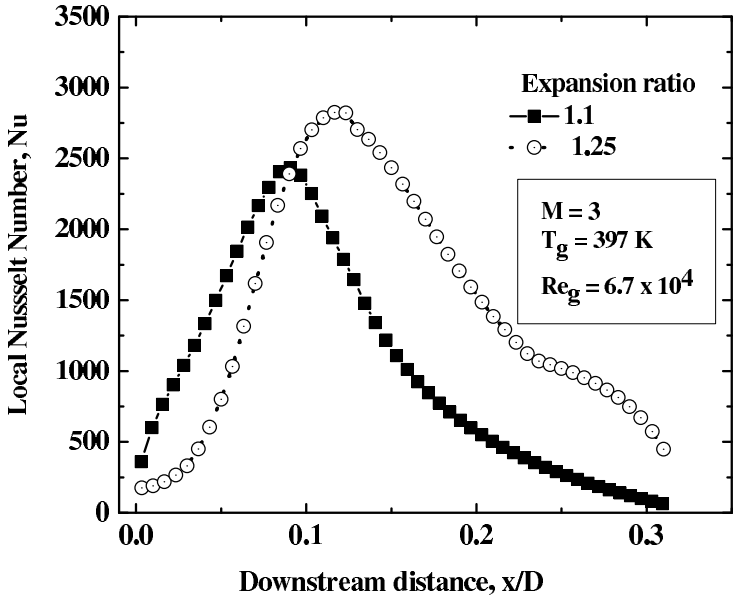

Figure 3.18: Local Nusselt number variation downstream of the step at ER = 1.1 and ER = 1.25.

3.3.5 Effect of coolant hole diameter

Figure 3.19 presents η_{comp} distribution in the axial direction for different diameter of coolant holes. The simulations are done at constant blowing ratio of M = 3. An equivalent slot width can be used to compare different coolant hole diameters (Bogard

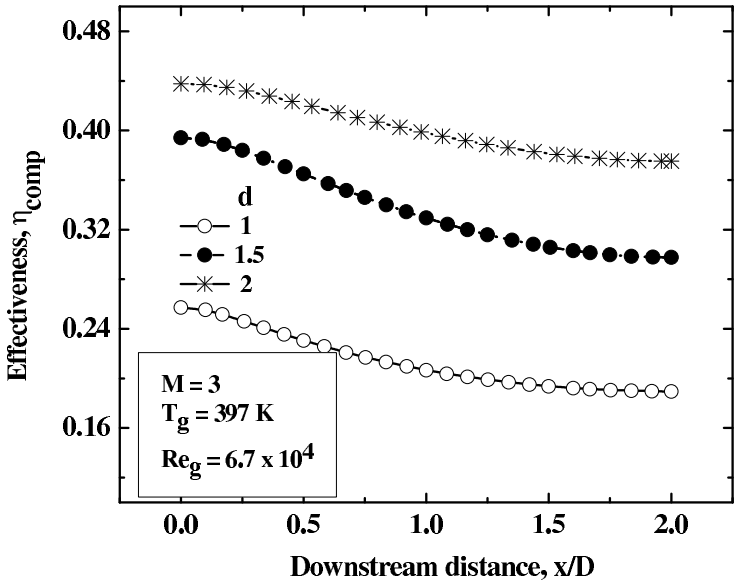

Figure 3.19: Variation along the axial length showing the effect of coolant hole diameter

and Thole, 2006) and is defined by

$$s_e = \frac{A_{hole}}{P_e} \tag{3.15}$$

where P_e is the pitch of the hole and A_{hole} is the area of cross-section of the coolant jet at exit. Here the total mass flow of coolant per circumference is equivalent to that for a slot of the same equivalent width. The s_e for the three coolant hole diameters 1, 1.5 and 2 mm are 0.1, 0.25 and 0.43 mm respectively. The highest effectiveness noted for d = 2 mm case is attributed to the presence of large amount of coolant near the wall. η_{comp} for the 1 mm hole is considerably less than the other two cases. The maximum turbulence intensity and radial vorticity levels at various locations downstream of coolant injection for different hole sizes are compared in Table 3.5. It is apparent that strong vortices and high levels of turbulence present at coolant exit in the case of small diameter holes. The jets in this study are discrete and there is 0.06D circumferential distance between adjacent jet center lines. Therefore, circumferential temperature distribution at various axial locations is analyzed for variation. It is noted that for all jets, the temperature variation around the circumference is almost negligible.

Table 3.5: Comparison of turbulence and vorticity levels at different coolant hole sizes at M = 3

	Maximum turbulence intensity levels in % compared to the hole exit plane of d = 1			Maximum vorticity % levels in % compared to the hole exit plane of d = 1		
Coolant hole size, d	At the hole exit	5 mm downstream of injection	10 mm downstream of injection	At the hole exit	5 mm downstream of injection	10 mm downstream of injection
1	100	136	80	100	9	1.6
1.5	83.4	147	109	62	11	2.2
2	77.4	126	123	60	7	3.4

3.3.6 Effect of hole spacing

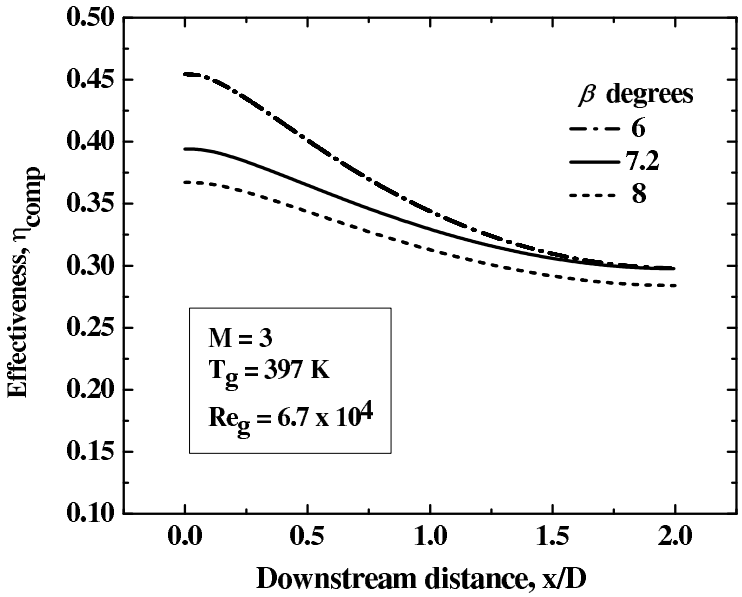

Figure 3.20: Film cooling effectiveness η_{comp} variation for various coolant hole spacing

Simulations were done for different circumferential arrangements of the coolant jet by varying the included angle (β) between the coolant holes. β values used in the study were 6°, 7.2° and 8°. The blowing ratio was kept constant at M = 3. Variation for the cases is plotted against the normalized test section length in Fig. 3.20. The η_{comp} for three β values 6°, 7.2° and 8° are 0.3, 0.25 and 0.22 mm respectively. The figure shows that cooling effectiveness increases with the decrease of β. But this effect

Table 3.6: Comparison of performance of coolant holes with β for M = 3

β	s_e	$\overline{\overline{\eta}}_{comp}$ in %	Decrease in β	% Variation in $\overline{\overline{\eta}}_{comp}$ compared to β = 8°
8°	0.22	35.7	0°	0
7.2°	0.25	38.2	0.8°	7
6°	0.3	43.2	2°	21

is observed only up to x/D = 1.5. When the jets are closer, the vortices generated in the adjacent holes interact with each other and prevents the mainstream gas to reach the metal surface. The main characteristics observed for the coolant holes with β = 6° are increase in vorticity levels in the neighborhood of injection (around 40%) and large vorticity destruction rate away from injection location. When β increases, more and more mainstream fluid reaches the metal surface and the effectiveness becomes low. No substantial circumferential temperature variation was noted for the three cases investigated.

Spatially averaged effectiveness parameter $\overline{\overline{\eta}}_{comp}$ is used for comparing the performance of coolant holes with different circumferential spacing. The effectiveness values showed appreciable variation up to x/D = 0.5 and therefore, $\overline{\overline{\eta}}_{comp}$ is calculated for a distance of x/D =0.5 downstream of the film coolant injection. Table 3.6 compares the variation in $\overline{\overline{\eta}}_{comp}$ for different coolant hole spacing compared to β = 8°. It is evident that variation of about 1% in $\overline{\overline{\eta}}_{comp}$ is observed with every 0.1° change in β with respect to β = 8°.

3.3.7 Free-stream turbulence effects

In a practical combustion chamber, swirling flow characterized by high turbulence intensity (Tu) has been shown to have a significant effect on the film cooling performance (Yang et al., 2007). Earlier results showed the film cooling effectiveness to decrease with increase in turbulence intensity (Marek and Tacina, 1975). Turbulence intensity in real engine would be much higher as measured by Hersh (1961) and Talmor (1966). Hersch conducted experiments in a liquid oxygen/gaseous hydrogen

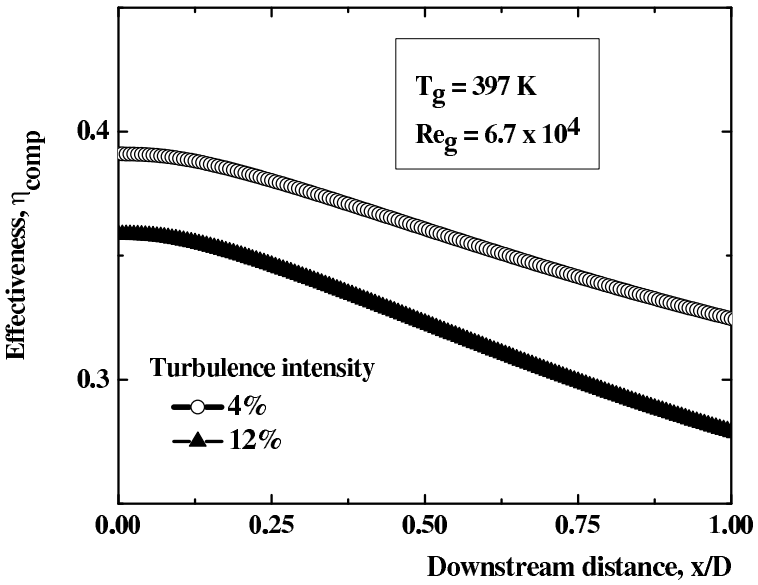

Figure 3.21: Variation of effectiveness at two turbulence intensity levels

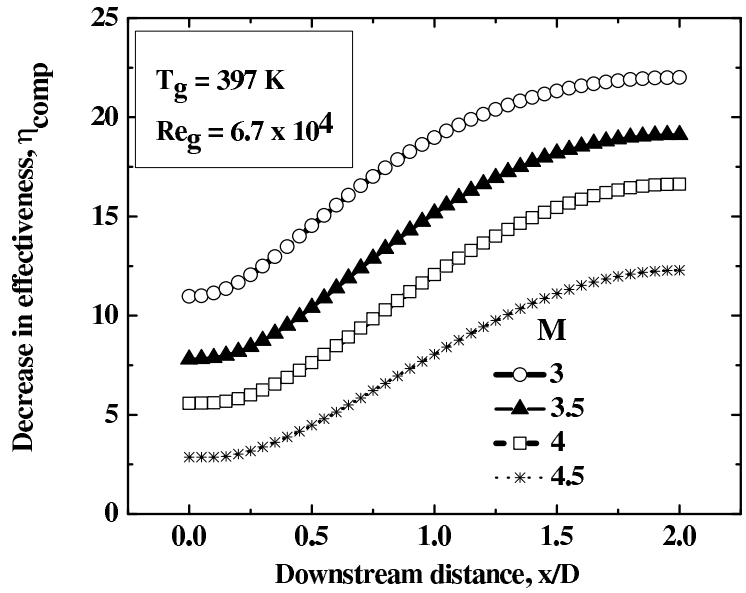

Figure 3.22: Percentage reduction in η_{comp} at Tu = 12% compared to Tu = 4%, at different blowing ratios

engine and measured Tu levels from 10% to 5% at distances of 5.08 to 20.32 cm from the injector. Talmor's experiments were in an N_2O_4/AZ50 engine and measured Tu levels from 20% to 15% at distances of 15.24 to 58.42 cm from the injector. Compared to this, low levels of Tu are only expected in the experiment as a flow straightner and a calming section is attached before the test section. In order to study the effect of higher free-stream turbulence on effectiveness, simulations are carried out with high

free-stream turbulence value of 12%. Figure 3.21 shows the effectiveness variation for the two turbulence levels. Figure 3.22 illustrates the percentage reduction in effectiveness (η_{comp}) resulted due to an increase in free-stream turbulence intensity from 4 to 12% for different blowing ratios. The effectiveness reduction is comparatively less at higher blowing ratios. Increased mixing of the coolant with the core gas due to higher free-stream turbulence resulted in further reduction in effectiveness at low blowing ratios. It can be concluded that higher free-stream turbulence can rapidly affect the flow field near the jet exit at low blowing ratios and can significantly reduce the film cooling effectiveness.

3.3.8 Effect of radiation of the outside surface

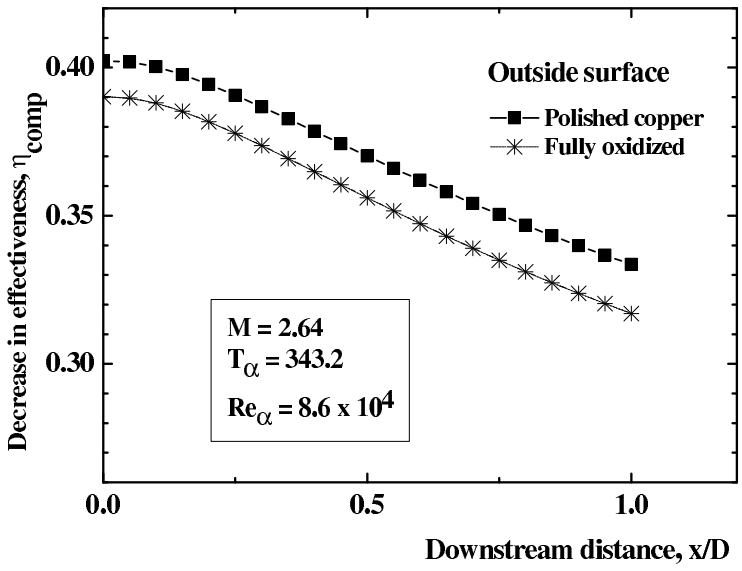

Figure 3.23: Effect of emissivity of test section outside surface on effectiveness

Simulations are carried out for polished copper surface with an emissivity value of 0.02. However, fully oxidised copper surface emissivity values are an order of magnitude higher. Therefore simulations are conducted to assess the effect of this variation. The effectiveness variation is shown in Fig. 3.23 for the straight injector at M=2.64. A variation of 10-15% in effectiveness is observed along the test section between the polished copper surface and fully oxidized copper surface.

3.4 Conclusions

Computational simulations are performed for a row of straight cylindrical coolant holes distributed circumferentially around a cylindrical test section. A 3-dimensional multi-species numerical model is developed using the finite volume based CFD code ANSYS FLUENT 13.0.0. Simulations used the RANS and k-ϵ turbulence model to compute film-cooling effectiveness for different cases: blowing ratios (1 to 4.5), three D/d ratios (60, 80 and 120), three expansion ratios, ER (1.1, 1.8 and 1.25) and three β (6, 7.2 and 8) values. The boundary conditions are chosen to match with the experimental test case as close as possible. The key conclusions from this study are as follows:

- Conjugate heat transfer model predicted the film-cooling effectiveness more accurately and showed significant difference with adiabatic model. The wall conduction effects tend to reduce the effectiveness near the coolant injection point. Higher effectiveness is persisted far downstream of the injection point for all conjugate cases investigated compared to the adiabatic case. A negative heat transfer condition was noted near the injection location for high conductivity walls and this brings out the fact that highly conductive wall is not a proper choice for internal wall-jet film-cooling applications.

- It is observed that the advantage of more coolant availability at high blowing ratios is offset by the higher mixing of coolant with the mainstream due to high turbulence and vorticity levels. This results in an optimum blowing ratio for a given geometric configuration and is around 3.5 for the present conditions.

- The variation in coolant jet exit momentum, the counter rotating vortices generated due to the interaction of coolant jet and the mainstream flow, and the strength of vortices are affecting film cooling performance in the neighborhood of injection.

- Secondary recirculation zones are developed adjacent to the jet exit in regions close to the wall and the centre. These flow structures are responsible for higher

mixing of the coolant and mainstream and the Nusselt number distribution immediately downstream of injection.

- Higher expansion ratio of the duct causes increase in turbulence and heat transfer coefficient and is resulting lower effectiveness at high expansion ratios.

- Simulations showed variation of about 1% in spatially averaged effectiveness parameter for every 0.1 degree change in the included angle between two coolant holes compared to β= 8° case.

- Increase in free stream turbulence reduces the film-cooling effectiveness and this effect is significant at low blowing ratios.

CHAPTER 4

SIMULATION II: GASEOUS FILM COOLING WITH COMPOUND ANGLE INJECTION

4.1 Purpose

The experimental studies described in Chapter 2 showed that in the case of gaseous film coolant injection, compound angle injectors had reasonably higher effectiveness compared to straight injector. However, for compound injectors, the increase in tangential angle from 30° to 45° resulted in increased wall temperature and a fall in effectiveness as discussed earlier and illustrated in Fig. 2.12. The experimental measurements provided a database of information describing the film cooling effectiveness of compound angle injectors. They do not explain the physical mechanisms responsible for such behaviour. Only a simultaneous, in-depth examination of the flow field and associated wall surface temperature profile can throw light on the phenomenon causing it. Therefore, numerical simulations are carried out for the two compound angle gaseous coolant injector configurations used in the experimental study. The main objective of the simulations is to assess the relative performance of different compound angle holes accurately and to identify the dominant flow mechanisms. It may also be noted that the contents of this chapter is based on Shine et al. (2013a).

4.2 Details of Numerical Simulation

The computational methodology implemented is already developed and validated for studying straight coolant injectors as described in Chapter 3. Consistent with those studies, CFD analysis is performed using a 3-dimensional multi-species numerical

model formulated using the control-volume approach. The continuity, momentum and energy equations are solved to predict velocity, temperature fields and conjugate film cooling effectiveness. High Reynolds-number k-ϵ turbulent model with standard wall functions is used for turbulence modelling. The interface between fluid and solid uses a coupled wall condition and this allows a direct calculation of the heat transfer and interface temperature. Species transport without chemical reactions are assumed to model mainstream and film coolant separately. The mathematical model, discretization schemes of governing equations, convergence criteria etc. are essentially the same as the already developed method for the straight injector.

The geometry of the present computational model is based on the experimental test set up. Since the experimental geometry has a periodicity between coolant holes, a sector containing two coolant holes is only considered for computations. The computational domain is exactly the same as the one described in Chapter 3 except the coolant injector configurations. The ambient temperature is assumed as 300K for all computations.

Numerical simulations are performed for both compound angle configurations of 30°-10° and 45°-10°. The boundaries are defined from experimental conditions. Pressure inlet condition is applied at mainstream inlet and coolant inlet zones. Outflow boundary condition is applied at the outlet. Rotational periodicity with no pressure loss boundary condition is specified at both side faces. Turbulence intensity is approximated based on the equation $Tu = Re^{\frac{-1}{8}}$ at the core gas inlet. The geometry and the mesh are created with multi-block structured grid. Cells in the model are entirely hexagonal and varied in size to have finer mesh around film hole and coolant flow regions. The normalized y^+ values at the near wall node are kept very close to 30. To study the grid-independence, four test grids are generated using the solution-based adaption capability. Refining of the grid is done until no appreciable changes are apparent in the film cooling effectiveness η_{comp} along the test section downstream of injection. The variation of η_{comp} is shown in Figure 4.1 and 4.2 for the grid-independence study cases. Very small change in effectiveness ($\approx 0.1\%$, observed with finer meshes, ensures that the model developed is very robust and is independent of the grid density of the computational mesh. The medium sized grid selected for

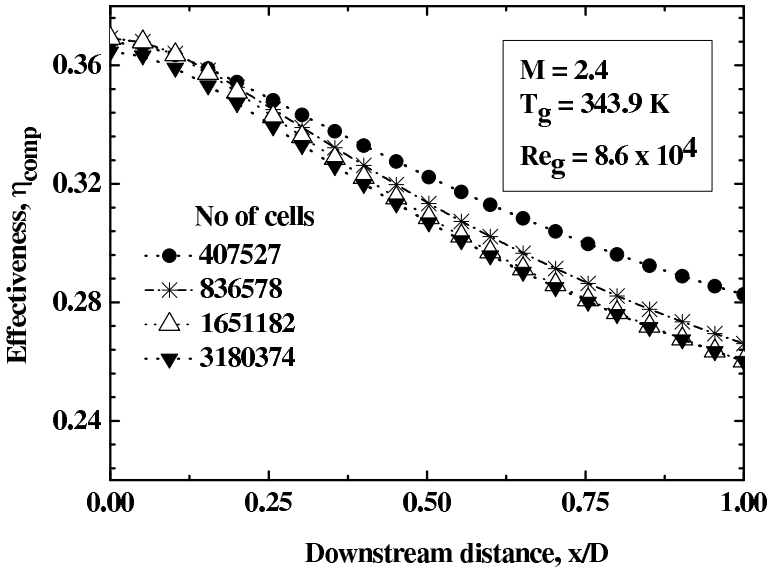

Figure 4.1: Grid sensitivity test for the 30°-10° injector

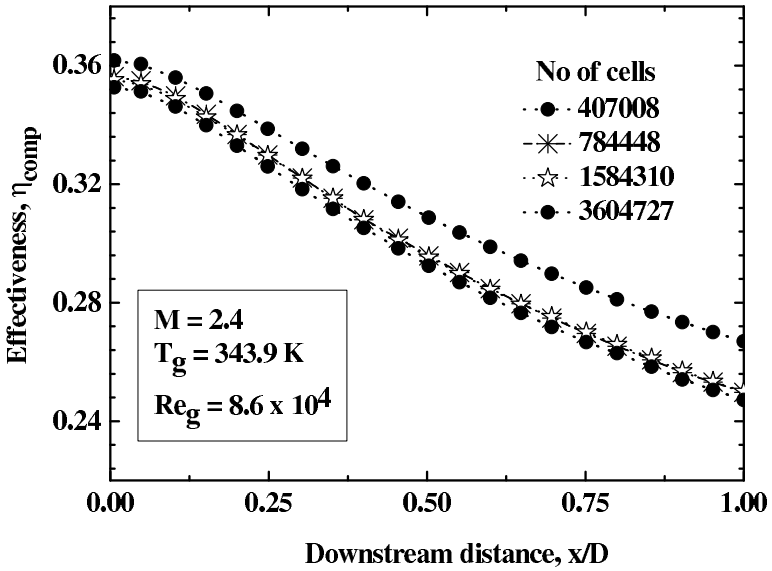

Figure 4.2: Grid sensitivity test for the 45°-10° injector

simulation of 30°-10° and 45°-10° injectors have total size of 1651182 and 1584310 cells, respectively.

4.3 Results and Discussion

The effectiveness parameters defined by equation 3.13 is used for validating different cases studied. ϕ_{AW} and ϕ_{conj} calculated using the equation 3.14 are used for com-

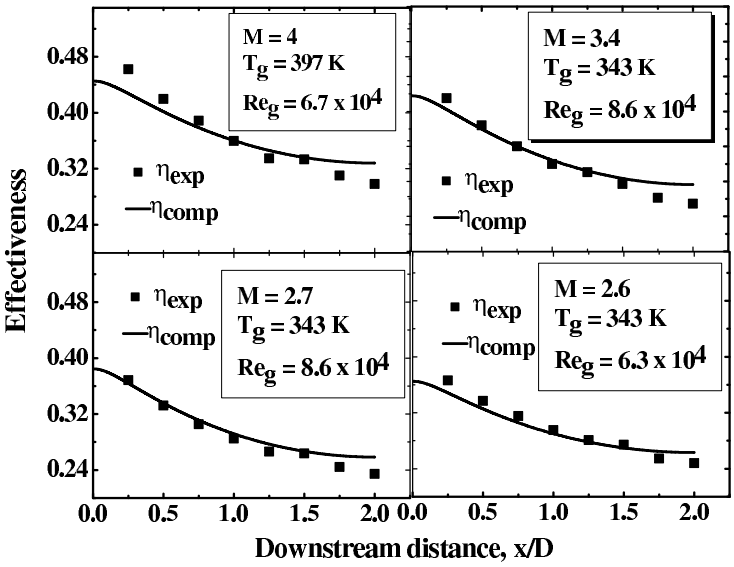

Figure 4.3: Calculated film-cooling effectiveness obtained from the computational model versus experimental values for the 30°-10° injector

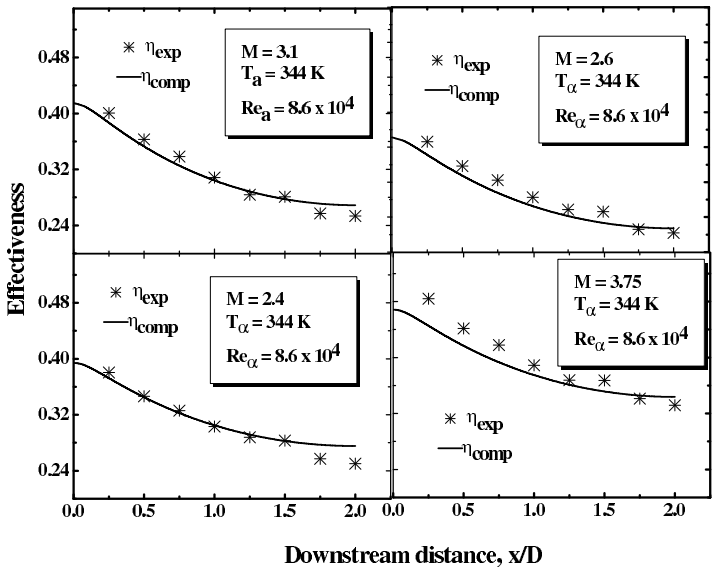

Figure 4.4: Calculated film-cooling effectiveness obtained from the computational model versus experimental values for the 45°-10° injector

paring computational adiabatic and conjugate models. The computational model was tested extensively by comparing the predicted results with four experimental cases for each coolant configuration. Comparison plots are shown in Fig. 4.3 and Fig. 4.4. These cases cover a range of blowing ratios varying from 2.4 to 4.0, and ratio of coolant temperature to mainstream temperature (TR) varying from 0.73 to 0.83. The temperature of the coolant gas is kept at 300 K. The comparisons showed good agree-

ment with experiments, and served to validate the computational methodology which was implemented. The global tendency is well predicted in all the cases.

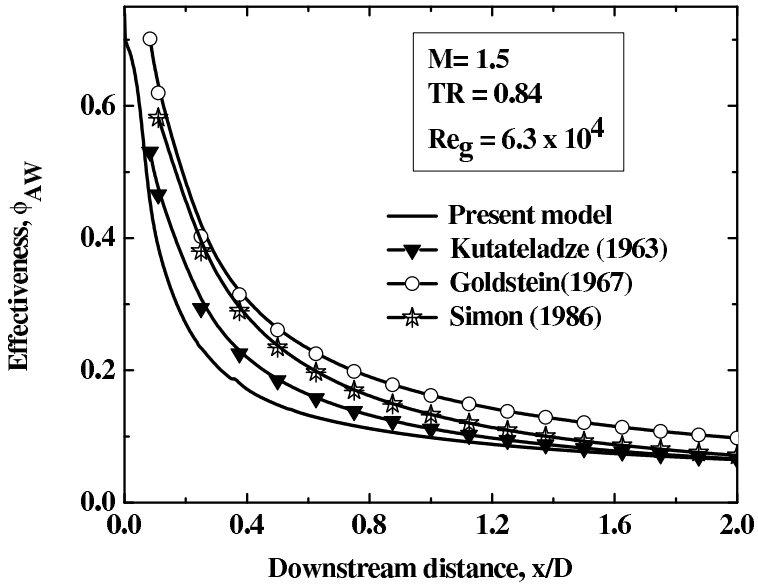

Figure 4.5: Comparison with other empirical models

In the past, few empirical film cooling effectiveness predictions have been proposed for tangential injectors by researchers. Two such models are compared with the current computational model developed for 30°-10° injector in Fig. 4.5. Adiabatic film cooling parameter ϕ_{AW} for the blowing ratio of 1.5 is compared. Kutateladze and Leontev (1963) proposed a correlation for flat plate with tangential injection for small temperature gradients. The model developed by Goldstein and Haji-Sheikh (1967) for turbulent incompressible flow has been extensively tested with experimental data and has shown good agreement for blowing ratios upto ≈ 1. Present model predicts lower adiabatic film cooling effectiveness values compared to all empirical models. The coolant jet is circular in nature and the coolant exposed to the mainstream has a width equal to the coolant jet diameter. This causes increased dispersion of the coolant and lower effectiveness. The figure also shows the predictions from Simon's (1986) jet model for slot film cooling. The values obtained from Simon's model lies above the present simulation, possibly due to the error sources previously mentioned in Section 3.3.

4.3.1 Velocity field

Contours of normalized axial velocity and plane tangential velocity vectors at 5 mm downstream of compound angle injection are shown in Fig. 4.6 to compare the flow fields downstream of the two coolant injectors considered. The coolant spreads and transforms into a circumferential flow pattern in both cases. The presence of jet is visible in the case of 30°-10° injector whereas the jet is completely spread in the case of the 45°-10° injector. To investigate the presence of coolant near the wall along the axial direction, the coolant concentration values along an axial line 0.25 mm away from the inside surface is obtained and plotted in Fig. 4.7. Higher coolant concentration is noted in the jet exit regions, but decreases to low values within an x/D of 0.2. In the near-hole regime of coolant holes, the vertical momentum imparted by the coolant hole orientation results in increased coolant concentration near the wall. This causes higher local effectiveness in these regions. At downstream positions, the mixing of the coolant with the core gas causes large reduction in effectiveness. Effectiveness for two blowing ratios are compared in Fig. 4.8. The coolant concentration values in the immediate region downstream of the jet exit are not significantly different for both injectors though an increase can be noted for the 45°-10° injector very near to the jet exit. The values for the 45°-10° injector are less than those with 30°-10° injector by approximately 10% in the downstream regions for all blowing ratios. As the tangential angle increases, lower stream-wise momentum of the coolant jet results in penetration of the mainstream leading to lower film cooling effectiveness.

The velocity vectors demonstrating the flow features downstream of the jet are shown in Fig. 4.9. Secondary recirculation flows are developed adjacent to the jet exit in the regions close to the wall and the center. The reverse flow region above the jet results from the rebound that develops when the jet impinges on the wall. It is observed that the reverse flow region near the wall decreases in size in the axial direction, as the tangential angle of the coolant jet changes from 30° to 45°. At regions close to the center, another recirculation zone develops adjacent to the step. A small "corner eddy" is also developed adjacent to the bottom corner of the jet. It is also noted that the size of the recirculation regions depends on the blowing ratio and the core gas Reynolds number. The secondary flow structures formed at regions close to the axis

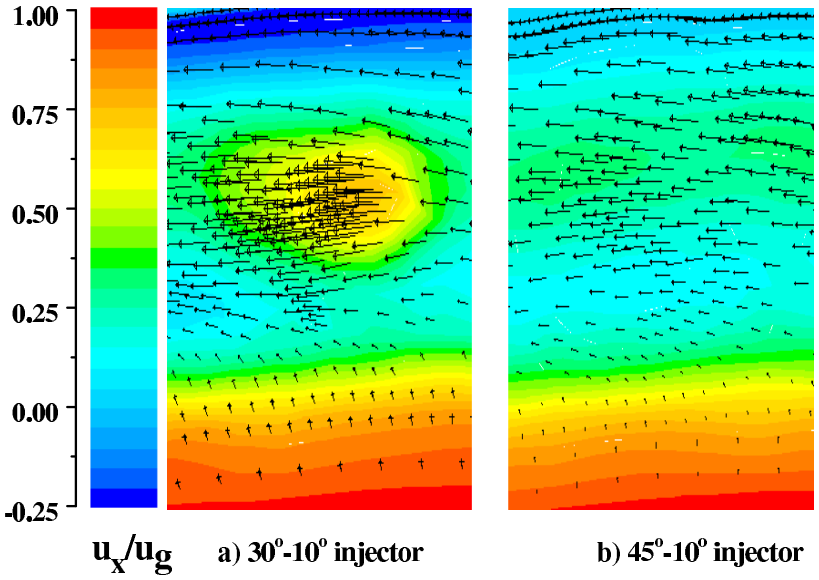

Figure 4.6: Contours of normalized axial velocity and plane tangential velocity vectors at 5 mm downstream of coolant injection for the two injectors. (TR = 0.84 and M = 2.7)

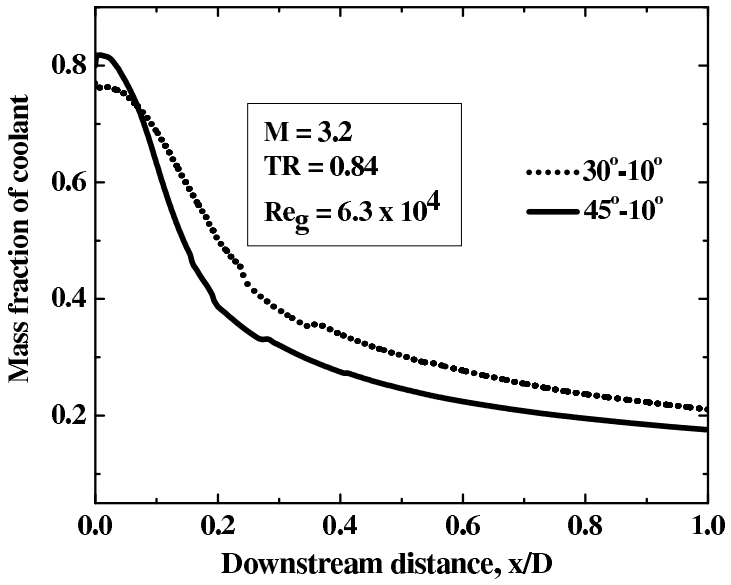

Figure 4.7: Mass fraction of the coolant along an axial line near the wall

are responsible for the higher mixing of the coolant and the mainstream, whereas the one formed close to the wall affects the Nusselt number distribution as explained in the subsequent section.

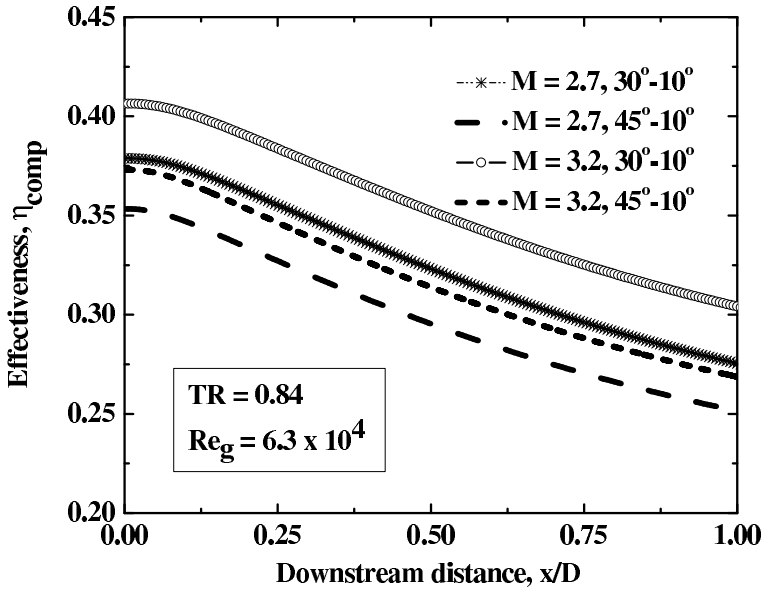

Figure 4.8: Comparison of effectiveness for various injectors

4.3.2 Nusselt number

Figure 4.10 illustrates the variation of local Nusselt number downstream of the coolant injection. Significant increase in the Nusselt number is observed for both the injectors. It is seen that a very high value of Nusselt number exists immediately downstream of coolant injection. The high conductive copper walls (k = 398 $WM^{-1}K^{-1}$) used in the simulations leads to significant heat transfer through the solid wall from the hotter downstream regions to the cooler upstream region and creates reverse heat transfer in the neighborhood of injection. The local heat flux curves at the solid-fluid interface for the various cases of wall conductivity for the 45°-10° injector are shown in Fig. 4.11. This illustrates the reverse heat transfer effects associated with high conductive walls.

There are two contributing sources for the increase in the Nusselt number viz., (i) the effect of abrupt expansion of the test section, (ii) the flow structures created by the coolant injection discussed earlier. As the geometry of both the cases is fixed other than the injector orientation, the effect of expansion ratio needs to be the same. The higher local wall Nusselt number downstream of a backward-facing step has been

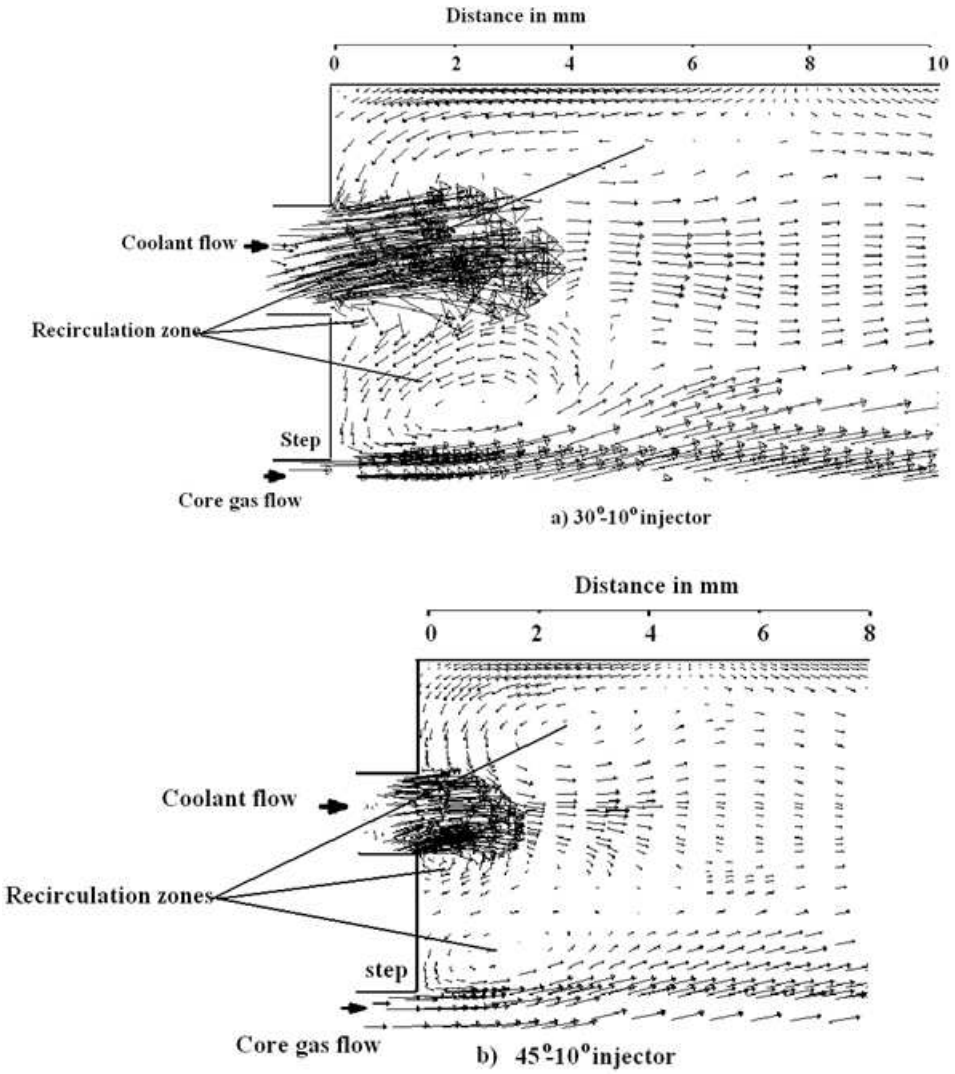

Figure 4.9: Velocity vectors demonstrating the flow features downstream of the step

noticed by Abu-Mulaweh et al. (2002)and Lan et al. (2009). Abu Mulaweh's experimental results on turbulent mixed convection flow along a vertical flat plate showed an increase in local Nusselt number from 150 to 490 at a core gas velocity of 0.41 m/s at an expansion ratio of 3. Numerical simulation of turbulent forced convection in a duct with backward facing step by Lan et al. (2009) showed higher local wall Nusselt number downstream of the step. He observed an increase from 20 to 49 in peak Nusselt number compared to the value at the corner of the step at a core gas Reynolds number of 4.7 x 10^4 at an aspect ratio of 3. It was also shown that the increase in the aspect ratio or the Reynolds number resulted in higher local Nusselt number. In the present analysis, the values for step height, expansion ratio (ER) and core gas Re are 6

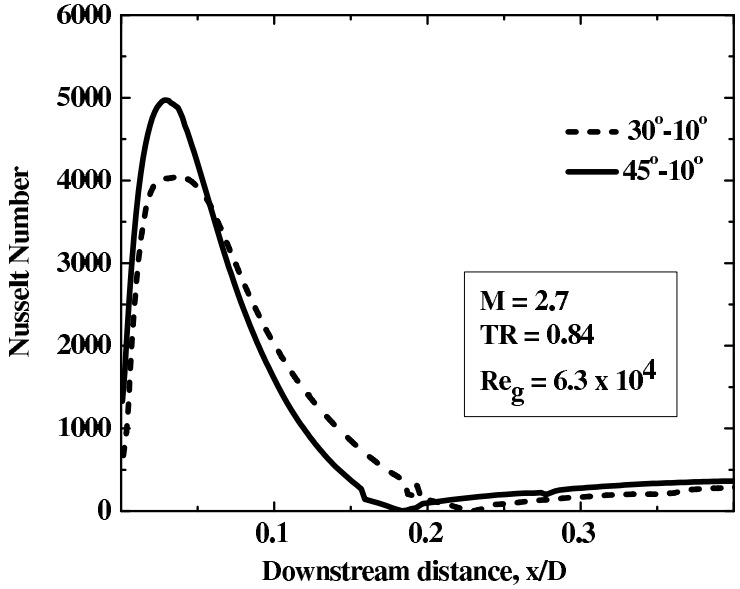

Figure 4.10: Local Nusselt number variation in the coolant injection regime for both injectors

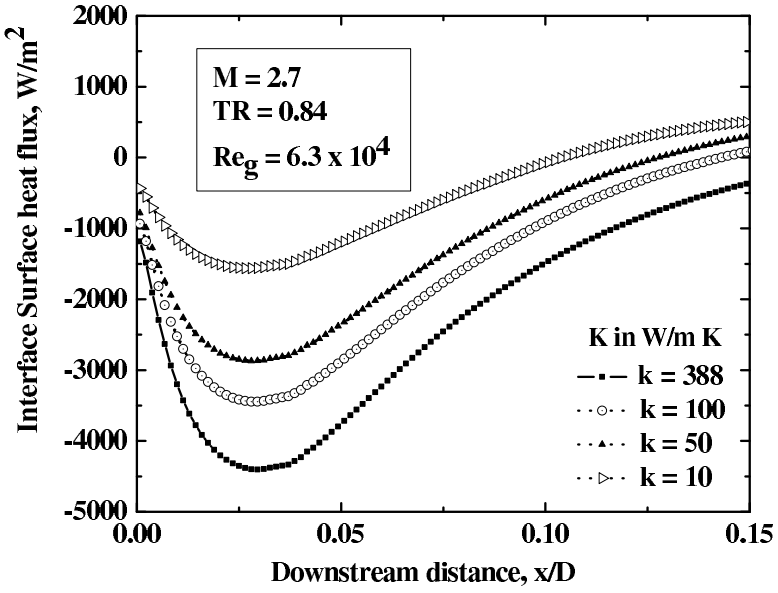

Figure 4.11: Interface surface heat flux variation for different wall thermal conductivities for the 45°-10° injector

mm, 1.11 and 6.3 x 10^4 respectively. Simulations show local Nusselt number increase from 670 to 4040 for the 30°-10° injector and 1330 to 4970 for the 45°-10° injector. It can be concluded that the presence of coolant jet, its interaction with the core gas, jet impingement on the wall etc. are the dominating mechanisms responsible for developing a maximum local Nusselt number downstream of coolant injection. The Nusselt

number remains constant away from the coolant injection location.

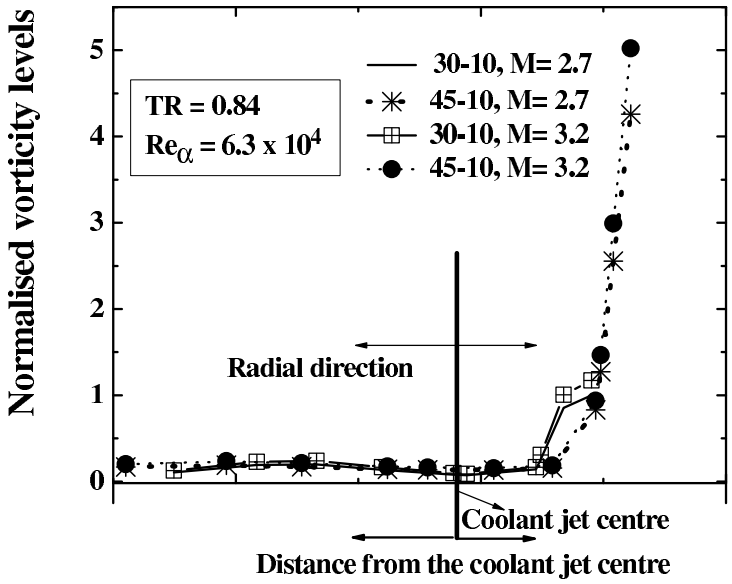

Figure 4.12: Normalized vorticity levels across coolant hole at the jet exit plane

4.3.3 Vorticity levels

The normalized vorticity levels (normalization done with the maximum vorticity levels present in the 30°-10° injector case at M = 2.7) across coolant hole at the jet exit plane is shown in Fig. 4.12. Vorticity appears to be a predominant flow feature that causes mixing and coolant spread in the circumferential direction. The main source of vorticity can be attributed to the coolant-hole boundary layers. Symmetric counter rotating vortices are noticed with straight cylindrical coolant holes. Present simulations of compound angle coolant holes showed shrinking of one vortex leg. High vorticity levels are observed at one side of the coolant hole for both injectors. Vorticity levels are found increasing with increase in tangential angle and blowing ratio. 45°-10° injector produced vorticity levels around five times higher than that observed with 30°-10° injector at a blowing ratio of 3.2. This asymmetric vorticity levels are responsible for higher lateral spreading of the coolant. As the coolant moves towards the downstream, the vorticity aligns itself with the coolant path. Relatively lower stream-wise momentum and higher asymmetric vorticity levels cause increased mixing of coolant

and mainstream in the case of 45°-10° injector. The increase in heat flux associated with high heat transfer coefficient results in lower effectiveness. At higher blowing ratio, the intensity of local vorticity increases. It is also noted that the vorticity is more aligned with original orientation at higher blowing ratios due to the higher momentum.

4.3.4 Adiabatic and conjugate cooling effectiveness

Like in the case of straight gaseous coolant injector, film cooling effectiveness for the adiabatic and conjugate cases is estimated in this case also and comparisons are made. Direct calculation of the heat transfer and wall temperatures is made using a coupled wall condition at the solid-liquid interface for the conjugate cases. Figure 4.13 illustrates the variation of ϕ_{conj} and ϕ_{AW} along the axial length. The coolant and core gas conditions are considered constant for all simulations. The adiabatic case provides the highest ϕ values for $x/D < 0.25$ and 45°-10° injector produces the highest cooling performance at the jet exit. This is attributed to lower temperature of the coolant at jet exit and more coolant availability for the 45°-10° injector in the hole exit regions as illustrated in Fig. 4.7. The axial conduction present in the case of conjugate walls offset the above advantage and produces lower effectiveness values. The effect is severe for the 45°-10° injector due to higher heat transfer coefficient in these regions. Substantially lower ϕ_{conj} values are noted for both injectors in the reverse heat transfer regimes. Due to the convective heat transfer effects, ϕ_{conj} is higher than ϕ_{AW} at far downstream of injection. Beyond this region, very close to the jet exit, 30-10 injector showed higher film cooling effectiveness throughout the test section for both adiabatic and conjugate cases. ϕ_{conj} values for different thermal conductivity wall materials are compared with ϕ_{AW} of 45°-10° injector in Fig. 4.14. The figure clearly indicates that the finite wall thickness and metal conductivity play a major role in deciding the film cooling performance of compound angle holes. Decrease in thermal conductivity of the test section has resulted in increase of ϕ_{conj} near the coolant jet exit and is within the region x/D < 0.25. The simulations showed about 80% increase of ϕ_{conj} for thermal conductivity decrease from 388 to 10 Wm^{-1} K^{-1}. The overall cooling performance over a length of x/D = 2 is compared by calculating a spatially averaged

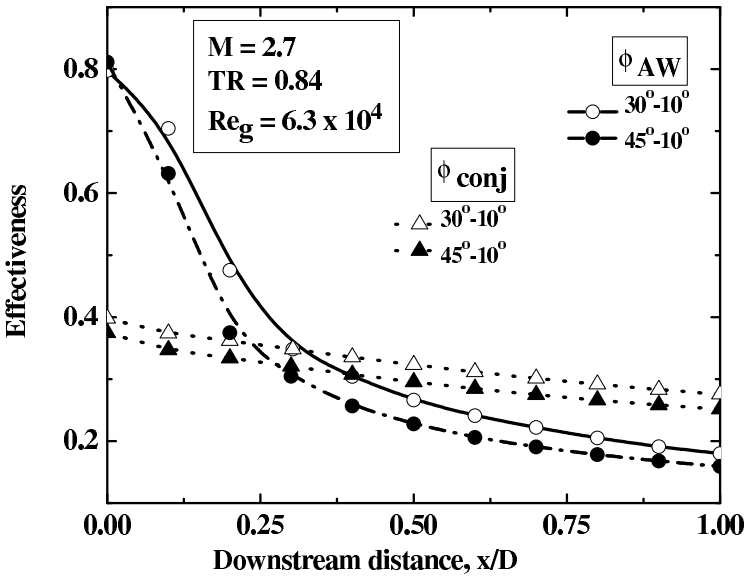

Figure 4.13: Comparison of the predicted ϕ_{conj} and ϕ_{AW} for both injectors

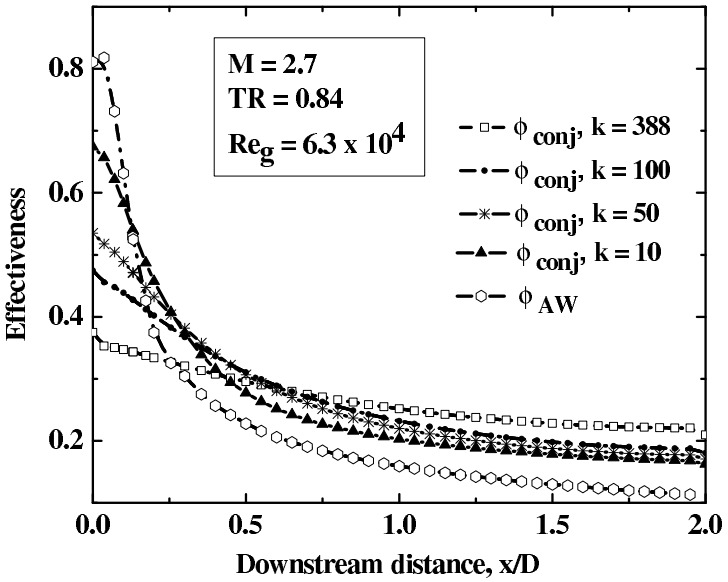

Figure 4.14: Variation of ϕ_{conj} for different wall conductivities and ϕ_{AW} of 45°-10° injector

effectiveness value. It is defined as the integral average of ϕ_{conj} along the axis for a length x/D = 2. The values of ϕ_{conj} obtained are almost similar (≈0.26) for k = 388, 100, 50 and 10 Wm^{-1} K^{-1} respectively. A significantly lower value of 0.209 is obtained for the adiabatic case. It can be concluded that the conjugate heat transfer cases studied exhibited higher overall downstream cooling performance compared to the adiabatic wall.

4.3.5 Effect of blowing ratio

Figure 4.15 presents the film cooling effectiveness of coolant hole configurations at a lower and a higher blowing ratios of 1.5 and 3.6. Both injectors are showing almost similar characteristics at M = 1.5, whereas 30°-10° injector shows an average 9% increase in film cooling effectiveness at M = 3.6. The increased effectiveness observed at higher blowing ratios is attributed to the presence of more coolant near the wall resulting in a longer jet. Because of the increased turbulent intensities and higher shear interaction with the mainstream, the heat transfer coefficient also increases at higher blowing ratios. Due to this, larger drop in effectiveness along the downstream direction is observed at M = 3.6. The higher lateral momentum and the stronger asymmetric vortices present with 45°-10° injector results increased mixing between coolant jet and mainstream. This reduces availability of the coolant near the wall and results in lower effectiveness.

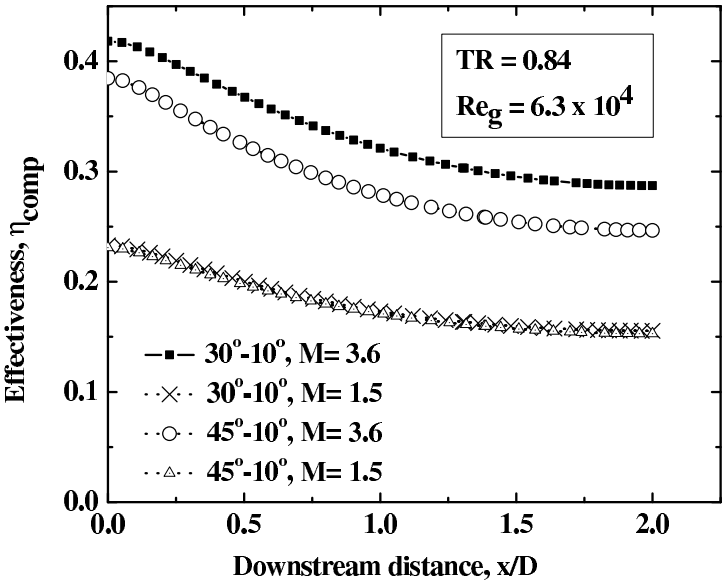

Figure 4.15: Variation of η_{comp} for low and high blowing ratios

4.3.6 Effect of free-stream turbulence

As rocket engines are characterised by high free-stream turbulence levels, its effect on film cooling characteristics is also investigated. Experimental investigations by

Al-Hamadi et al. (1998) showed significant reduction in local film cooling effectiveness for compound angle coolant holes at high free-stream turbulence levels. Marek and Tacina (1975) has noted an inverse relation between film cooling effectiveness and free-stream turbulence level. Simulation of straight injectors revealed the effects to be more predominant at low blowing ratios. Figure 4.16 illustrates the effect of turbulence intensity on film cooling performance. The percentage reduction in η_{comp} predicted for both compound injectors for Tu values of 8 and 12% as compared to Tu = 4% is plotted. Similar behaviour seems to exist in both injectors, even though a slight increase is noted for 30°-10° injector. Lower effectiveness is observed at high turbulence intensity and its effects are more predominant at locations away from the coolant jet exit.

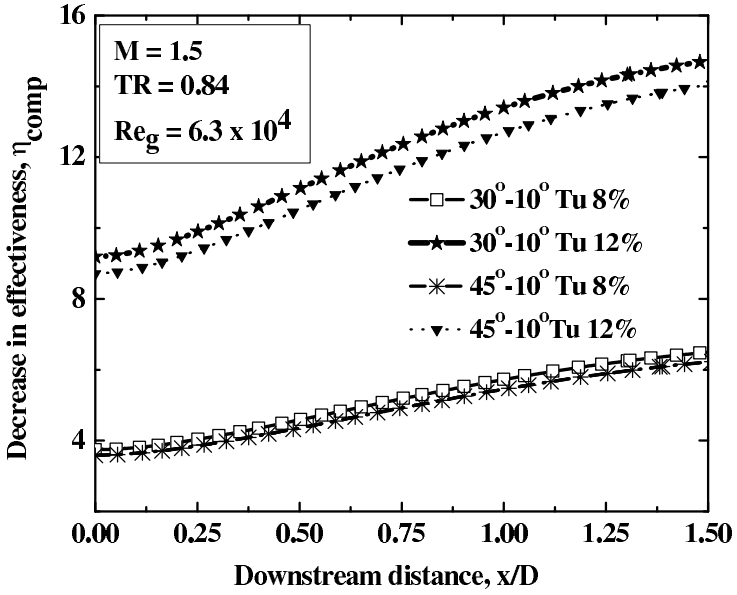

Figure 4.16: Percentage reduction in η_{comp} at Tu = 12% compared to Tu = 4%, at different blowing ratios

4.4 Conclusions

Computational simulations are performed for a row of circumferential gaseous film-cooling holes employed inside a circular pipe with two distinct configurations: (i) holes with a tangential angle of 30-deg and an azimuthal angle of 10-deg; (ii) holes

with a tangential angle of 45-deg and an azimuthal angle of 10-deg. Simulations are carried out using the computational fluid dynamics code ANSYS FLUENT 13.0.0. Species transport equations, RANS and the k-ϵ turbulence model are used to compute flow field and film cooling performance associated with adiabatic and conjugate wall conditions. Important observations from the study are summarized below.

- Except at regions very close to the coolant jet exit, 30-10 injector exhibited better film cooling performance for both adiabatic and conjugate wall conditions. The poor performance of the 45-10 injector is due to the increased mixing of coolant and mainstream caused by the relatively higher asymmetric vorticity levels and lower stream-wise momentum present. The coolant jet exit-conditions are highly nonuniform and configuration dependent. It can be concluded that increasing the tangential angle do not necessarily provide improvement in the film cooling performance.

- Secondary flow recirculation zones are found adjacent to the jet exit in the regions close to the wall and the centre. Its occurrence and size are mainly affected by the injector configuration, blowing ratio and mainstream Reynolds number.

- Increase in tangential angle has resulted in significant increase in Nusselt number in the jet-exit regions. A local maximum value is observed around the reverse flow regions close to the wall.

- The wall conduction effects tend to reduce the effectiveness near the coolant injection point. The heat transfer through the solid wall from the hotter downstream to the cooler upstream region is noted. Results show significant effect of wall conductivity on the temperature field in the jet exit regions, and additional heating of the jet.

- Higher coolant concentration near the walls produced higher adiabatic film cooling performance for the 45-10 injector at regions very close to the coolant jet exit. All the conjugate heat transfer cases studied exhibited higher overall downstream cooling performance compared to adiabatic case.

- Numerical results show film cooling performance for both injectors are similar at low blowing ratios, whereas 30-10 injector has the advantage of higher performance at higher blowing ratios.

- Adiabatic wall provided the highest effectiveness near the coolant jet exit. The axial wall conduction effects tend to reduce the effectiveness near the coolant injection point. Higher far field effectiveness is observed for the conjugate walls owing to convective cooling effects.

CHAPTER 5

ANALYTICAL MODEL FOR LIQUID FILM COOLING

5.1 Introduction

This chapter introduces a new one-dimensional analytical model of the liquid film cooling process at subcritical conditions. The emphasis is on predicting the liquid film cooled length accurately under various injection conditions. Film cooling is analyzed as a collection of several fundamental processes. The analysis thoroughly examines all the energy interactions with the liquid film. The approach followed involves the selection of a control volume for mass and energy balance. Significant terms in the energy equation are then identified. The coolant evaporation rate per unit surface area is obtained from this energy balance. The coolant flow per circumferential length of the combustion chamber is calculated after considering the losses at injection point and the losses due to entrainment of liquid. The liquid film length is determined from the coolant flow (per circumference) and the evaporation rate per unit surface area. Most appropriate models pertaining to the situation are selected from literature to calculate the energy interactions and the liquid entrainment rate. Effects of gas Reynolds number, coolant inlet temperature, combustion chamber pressure, mass flow ratio of the liquid coolant to the core gas and the free stream turbulence on the liquid film length are analysed in detail. It may also be noted that the contents of this chapter is based on Shine et al. (2012c).

5.2 Analysis of Liquid Film Evaporation

Liquid film cooling analysis basically involves the mass and energy balance of the liquid film. The present model uses a control volume (Fig. 5.1) for the mass and

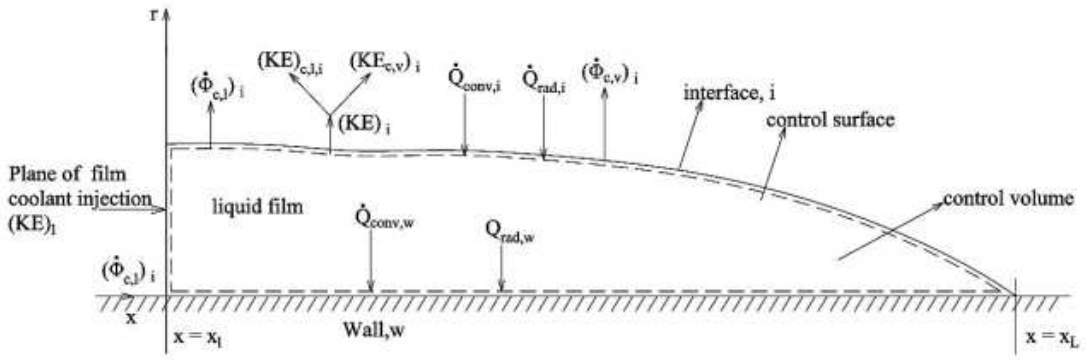

Figure 5.1: Control volume for energy balance.

energy balance. The conservation of mass requires that for steady state conditions, the incoming coolant mass flow rates equal the mass lost from the control volume. Here, the coolant is lost due to the evaporation and entrainment processes. Therefore, the mass balance equation is

$$\dot{m}_c = \dot{m}_{evap} + \dot{m}_{entr} \tag{5.1}$$

The energy interactions accounted are; (i) convection and radiation heat transfer at the interface of liquid film with the combustion gas, and at the solid wall, (ii) enthalpy and kinetic energy carried by coolant vapour, entrained liquid at the interface and the liquid coolant entering the control volume. Applying law of conservation of energy for steady conditions,

$$\begin{aligned} (KE)_1 + (\Phi_{c,l})_1 + \dot{Q}_{conv,i} + \dot{Q}_{rad,i} \quad &= \\ (\Phi_{c,l})_i + (\Phi_{c,v})_i + (KE)_i + \dot{Q}_{conv,w} + \dot{Q}_{rad,w} & \end{aligned} \tag{5.2}$$

In most cases, the kinetic energy terms and radiation at the wall can be neglected in comparison to other terms. Also neglecting the enthalpy increase of the entrained liquid inside the control volume,

$$\begin{aligned} (\Phi_{c,l})_i + (\Phi_{c,v})_i - (\Phi_{c,l})_1 &\approx (\dot{m_{c,v}})_i \, h_{fg,c} + (\dot{m_{c,v}})_i \, (T_{sat,c} - T_{c,1}) c_c \\ &\approx (\dot{m_{c,v}})_i h^*_{fg}, \qquad (5.3) \\ where, h^*_{fg} &= h_{fg,c} + (T_{sat,c} - T_{c,1}) c_c \qquad (5.4) \end{aligned}$$

Therefore (5.2) becomes

$$(\dot{m}_{c,v})_i = \frac{1}{h^*_{fg}} \times \left(\dot{Q}_{conv,i} + \dot{Q}_{rad,i} - \dot{Q}_{conv,w}\right) \tag{5.5}$$

The coolant liquid is injected at a temperature below its saturation temperature. Therefore, low temperature gradients will exist at the wall surafec as long as the coolant film is present. Coolant velocity is very low compared to the velocity of the core gas flow resulting in lower convective heat transfer coefficients near the wall. The convective heat transfer to the wall $\dot{Q}_{conv,w}$ is neglected due to the reasons cited above.

Estimation for convective and radiative heat transfer, transpiration effects, gas-liquid interface characteristics and entrainment, and free stream turbulence are explained in the succeeding sections.

5.2.1 Determination of convective heat transfer coefficient

In the previous analyses (Shembharkar and Pai, 1986; Grisson, 1991), flat plate correlations were used to determine the convective heat transfer coefficient. It may be noted that the flow inside the combustion chamber is almost like that of turbulent flow through a pipe. Recently, a new debate has started regarding the nature of the mean velocity profile of canonical turbulent wall bounded flows. The existence of a universal log law for turbulent pipe and channel flows and turbulent wall bounded flows are being questioned by Wosnik et al. (2000) and George (2007). Experiments were conducted by Monty et al. (2009) at matched measurement resolution and friction Reynolds number (Kármán number) in all the shear flows (pipes, channels and wall boundary layers). Their result suggests that all three flows might be of a similar structure. However there are obvious important differences between them, not only in the outer region, but right down to the wall. The difference is in the largest energetic scales, which are much longer in pipes. The observed large scale differences will be more obvious at high Reynolds numbers as Hutchines and Marusic (2007) have shown that the magnitude of the energy contribution of superstructures increases with Reynolds number. Hence, from literature, it is concluded that internal and external

flows have similarities as well as important differences especially at high Reynolds number. For the gas flow in a combustion chamber, Reynolds number is very often up to 10^7 or even higher. Friction factor relationship proposed by Mckeon et al. (2005) for fully developed pipe flow, which is given below, is used in this analysis.

$$\frac{1}{\sqrt{\lambda}} = 1.930\, log\left(Re\sqrt{\lambda}\right) - 0.537 \tag{5.6}$$

$$for \quad 300 \times 10^3 \leq Re \leq 18 \times 10^6$$

Analogy between heat and momentum transfer using friction factor relationship is used to calculate the heat transfer coefficient. Many models have been proposed in the past for turbulent flow through tubes and circular conduits. Aravinth (2000) compared the various correlations using experimental data points and found that Friend and Metzner equation (Friend and Metzner, 1958) represents the data better than others at low Prandtl numbers. This equation is used in the present analysis. The equation for Pr/Sc in the range 0.5 to 3000 and Re in the range 10^4 to 10^6 is given as:

$$St = \frac{\frac{f}{2}}{1.20 + 11.8\sqrt{\frac{f}{2}}(Pr-1)(Pr)^{-1/3}} \tag{5.7}$$

5.2.2 Transpiration effects

The transport of the vapour resulting from the evaporation of liquid coolant has two-fold effect of acting as a heat sink and of altering the heat transfer characteristics in the boundary layer. The vapour flowing away from the liquid film is similar to injecting cooling gas to the hot core gas. This method of cooling a surface is called transpiration cooling. Transpiration of gas into turbulent boundary layer has a strong influence on boundary layer characteristics, particularly skin friction, including flow separation and heat transfer (Meinert and Huhn, 2001). The most important factors affecting these processes are (i) the coolant mass flow density $\rho_{c,v}v_{c,v}$ described by the blowing ratio, $(\rho_{c,v}v_{c,v})\,/\,(\rho_g u_g)$, (ii) the properties of coolant and hot gas (main

flow) expressed in terms of the molecular weights $\mathcal{M}_c$ and $\mathcal{M}_g$, (iii) the ratio between the wall temperature T_w and the static hot-gas temperature T_g, and (iv) the flow and geometrical conditions described by the Reynolds number (Re) (Meinert and Huhn, 2001). Keener et al. (1995) measured experimentally a 14% reduction in the heat transfer coefficient for a blowing ratio of 0.51% in a two-dimensional contoured nozzle. Jiang et al.'s (Jiang et al., 2004) numerical results showed a 50% reduction in heat transfer coefficient for a blowing ratio of 1%. Transpiration affects the structure of boundary layer and the sublayer thickness. Aproximate closed-form algebriac solutions are available to provide quick and easy solutions. The Couette flow solution proposed by Kays and Crawford (2005) had predicted experimental data well and is used in the present analysis. From the simplified one-dimensional thermal energy balance, Kays and Crawford (2005) gave a relation for the Stanton numbers with and without transpiration as shown below.

$$\frac{St}{St_o} = \frac{F/St_o}{exp\left(F/St_o\right) - 1} \tag{5.8}$$

F is the blowing ratio and is given by, $F = \frac{\dot{m}_{film}}{\dot{G}}$, where $\dot{m}_{film}$ is the coolant film evaporation rate per unit area and $\dot{G}$ is the core gas mass flux rate.

Meinert and Huhn (2001) proposed a correlation by adding two correction factors k_M^* and k_T^*,

$$\frac{St}{St_o} = \frac{\left(F/St_o\right) k_M^* k_T^*}{exp\left[\left(F/St_o\right) k_M^* k_T^*\right] - 1} \tag{5.9}$$

where in k_T^* is a correction factor for temperature ratio and k_M^*, the correction factor for molecular weight ratio. Meinert further states that heat transfer coefficient has very small dependence on the temperature ratio and considerable effect on cooling gas properties. He proposes the property correction factor $k_M^* = \left(\mathcal{M}_g/\mathcal{M}_c\right)^{0.6}$ and neglects the temperature correction factor k_T^*. Equation (5.9) can be rewritten as

$$\frac{St}{St_o} = \frac{ln\left[1 + \left(F/St\right)\left(\mathcal{M}_g/\mathcal{M}_c\right)^{0.6}\right]}{\left(F/St\right)\left(\mathcal{M}_g/\mathcal{M}_c\right)^{0.6}} \tag{5.10}$$

The total heat flux due to both convection and radiation, $\dot{Q}_{tot}$ is absorbed in the liquid film. The evaporation of the coolant film is caused by this heat flux. The evaporation rate per unit area is

$$\dot{m}_{film} = \frac{\dot{q}_{conv} + \dot{q}_{rad}}{h^*_{fg}} \tag{5.11}$$

Therefore blowing ratio F is

$$F = \frac{\dot{m}_{film}}{\dot{G}} = \frac{\dot{q}_{conv} + \dot{q}_{rad}}{h^*_{fg}\dot{G}} \tag{5.12}$$

$$and, \quad \frac{F}{St} = \frac{c_g}{h^*_{fg}}\left[(T_g - T_{c,sat}) + \frac{\dot{q}_{rad}}{h}\right] \tag{5.13}$$

5.2.3 Gas-liquid interface characteristics

The specification of the physical characteristics of the gas-liquid interface is also very important in the analysis of liquid film cooling. Available experimental data show that the interfacial structure has considerable influence on the flow rate of film coolant required for establishing a specified liquid-film-cooled length (Kinney et al., 1952; Knuth, 1954; Graham, 1958; Sellers, 1958). The interfacial structure characterized by its "pebbled" appearance is quite common. The small disturbances on the surface of the liquid film are apparently a consequence of turbulent velocity fluctuations in the gas phase flowing past the liquid film; the turbulence scale of the gas phase decreases with increasing gas mass flow rate. Photographic studies show that the length scales of these disturbances decrease at higher velocities Knuth (1954). As the gas velocities are very high in a rocket combustion chamber the effects of such a phenomenon is neglected.

Film instability is characterized by the existence of large-scale disturbances which are turbulent in nature, and is superimposed on a "pebbled" interfacial structure (Taylor et al., 1963). A large degree of liquid entrainment is known to occur when large-scale disturbances appear on the surface of a liquid film. The disturbance waves transverses the liquid film interface and causes the droplet entrainment. Knuth (1954) from his liquid-film stability experiments confirmed that longer wavelength disturbances

appeared only after some critical flow rates of coolant is reached. Knuth was able to correlate both his data and that of Kinney et al. (1952). Knuth's correlation for the critical liquid mass flow per circumference when $\frac{\mu_{c,v}}{\mu_{c,l}} > 0.03$ is,

$$\Gamma_{cr} = 1.01 \times 10^5 \frac{\mu_{c,v}^2}{\mu_{c,l}} \tag{5.14}$$

Similar phenomenon is observed in annular two phase flow which is characterized by the presence of liquid film on the tube wall and gas phase flowing through the tube core. A number of correlations are available for annular flow for predicting the entrainment fraction E, the fraction of the total liquid flow flowing in the form of droplets through the central gas core. However, these studies are conducted at lower momentum flux conditions compared to film cooling applications. Correlations proposed by Sawant et al. (2008) are valid up to a momentum flux of 200,000 Pa and is used in the present analysis. Even though the correlation is developed for vertical flow, it can be used for horizontal flow also as the asymmetric distribution of drops due to gravity disappears at large velocities. The correlation proposed by Sawant et al. (2008) for the prediction of entrainment fraction is,

$$E = E_m tanh(aWe^{1.25}) \tag{5.15}$$

$$where, a = 2.31 \times 10^{-4} Re_c^{-0.35} \tag{5.16}$$

$$E_m = 1 - \frac{Re_{cfilm}}{Re_c} \tag{5.17}$$

$$Re_{cfilm} = 250ln(Re_c) - 1265 \tag{5.18}$$

$$We = \rho_g u_g^2 D/\sigma \left(\Delta\rho/\rho_g\right)^{1/4} \tag{5.19}$$

5.2.4 Free-stream turbulence

Pletcher (1988) noted that convective heat flux increases by a factor $K_t = 1 + 4e_t$ in the presence of an RMS turbulence fraction, e_t, in the core gas flow. Hersh (1961) and Talmor (1966) measured the turbulence intensities in rocket engines. Their results are presented in section 3.3.7. The effect of free-stream turbulence has been taken into account in the present analysis for calculating the heat transfer coefficient and is described in section 5.3.

5.2.5 Radiative heat transfer

Calculation of radiative heat transfer or combined convection and radiation heat transfer at high temperature gas flows requires both the knowledge of spectral radiative properties of the gases and efficient methods for solving radiative transfer equations (Viskanta, 1998). Models for determining the spectral radiative properties of the gases include, (i) the line-by-line approach based on a direct numerical calculation of all the lines or of all radiating species in the gas, and (ii) the molecular band models, where in the spectrum is subdivided into narrow bands and radiative characteristics averaged over each band, are calculated from the absorption spectrum or from the statistical properties of the lines. In view of the complexities of the theory and the associated uncertainty in the calculated gas emissivity, correlations prepared by Leckner (1972) for total emissivity are used in the present analysis. These correlations have a maximum error of 5% for water vapour and 10% for CO_2 compared to his charts based on the integration of spectral data (Modest, 1990). Leckner's data also shows that the results obtained from extrapolation of experimental data of Hottel are seriously in error (Modest, 1990). The radiative heat transfer from combustion products is mainly due to the heteropolar gases present, the most common of which are CO_2, H_2O, CO, NH_3 and SO_2 out of which the major contribution is from water vapour and carbon dioxide. Symmetrical molecules such as H_2, O_2 and N_2 do not show absorption bands at the wavelengths encountered and hence these are transparent to radiation and have negligible emissivity (Mehrotra et al., 1995).

5.2.6 Calculation of properties of gases

Values of specific heat for component gases are calculated from Table A-9 of Norton (2005). The specific heats are weighted by the mass fractions of species to obtain mixture specific heat. The viscosities are calculated from the Chapman-Enskog correlation, using the values in Appendix C of Reid et al. (1977). The mixture viscosity is then calculated using the Wilke's approximation (Wilke, 1950). Thermal conductivities of individual gases are calculated using Stiel and Thodos (1964) correlations.

Then specific heat and viscosity values calculated above, are used for calculating the Prandtl number.

5.3 Solution Methodology

The liquid film cooled length, L_c is calculated for different experimental conditions. The solution procedure can be summarized as follows.

1. Obtain the test data required for calculations from the experimental values. The values required are $\dot{m}_g$, $\dot{m}_c$, P_{cc}, and D_{cc}. The free stream gas composition is calculated from the experiment details. The data required are the composition of fuel and oxidizer, and fuel-oxidizer ratio.

2. The free stream gas composition is calculated based on the oxidant/fuel ratio (O/F). Calculate the properties of the free stream gas c_{p_g}, μ_g, Pr_g and ρ_g as per the procedure mentioned in section 5.2.6.

3. Obtain the liquid coolant properties such as $c_{c,l}$, h_{fg}, $T_{c,sat}$ and $\rho_{c,l}$ corresponding to average combustion chamber pressure.

4. Calculate Re_g. Note that Re_g is calculated from the velocity corrected free stream mass flux, G_{mean}. This is to account for the velocity of the liquid coolant u_c. The procedure is shown below.

$$\begin{aligned} G_g &= \rho_g \times u_g \\ G_{mean} &= G_g \times (u_g - u_c)/u_g \\ Re_g &= G_{mean} \times D_{cc}/\mu_g \end{aligned}$$

5. Calculate Darcy friction factor (λ) using Equation (5.6) and St_o using Equation (5.7).

6. Obtain the value of free-stream turbulence (e_t) from the test data. Obtain K_t as $K_t = 1 + 4e_t$. Calculate, h_o using the following equation, $h_o = G_{mean} \times c_g \times St_o \times K_t$.

Table 5.1: Comparison of experiments by Knuth (1954) and Morrell (1951)

Parameter	Knuth (1954)	Morrell (1951)
Re_g	0.5 - 5 $\times$ 10^5	$\approx$ 2.5 $\times$ 10^5
Gas Momentum Flux (Pa)	40,000 - 200,000	$\approx$ 40,000
D_{cc} (m)	0.07366	0.1016
P_{cc} (bar)	$\approx$ 1	$\approx$ 17-18
T_g (K)	600 - 1250	$\approx$ 2950

7. Calculate h^*_{fg} using Equation (5.4).

8. Obtain emissivity from Leckner's (Leckner, 1972) correlations and calculate $\dot{q}_{rad}$.

9. Obtain transpiration corrected St implicitly from (5.10) and (5.13). Calculate h from St.

10. Calculate $\dot{q}_{conv}$ as $\dot{q}_{conv} = h \times (T_g - T_{c,sat})$.

11. Calculate $\dot{q}_{tot}$ as $\dot{q}_{tot} = \dot{q}_{rad} + \dot{q}_{conv}$ and $\dot{m}_{film}$ as $\dot{m}_{film} = \frac{\dot{q}_{tot}}{h^*_{fg}}$.

12. Calculate the entrainment fraction using the correlations proposed by Sawant et al. (2008). The method is described in section 5.2.3. Obtain Γ_c, the coolant flow rate per circumference available for film cooling.
    Coolant flow per circumference available for film cooling,
    $\Gamma_c = \frac{\text{(Total coolant flow rate - Coolant loss due to entrainment)}}{\text{Circumferential length}}$

13. Calculate the liquid film cooled length, $L_c = \frac{\Gamma_c}{\dot{m}_{film}}$.

A complete set of calculations based on one set of Morrell's (1951) experimental data is given in Appendix B.

5.4 Results and Discussion

The model developed is tested extensively by comparing the results with film cooling experiments available in literature. Experimental results reported by Knuth (1954)

Table 5.2: Comparisons of model predictions with Knuth (1954) experimental data

Case No	T_g (K)	Gas flow, $\dot{m}_g$ (kg s^{-1})	P_{cc} (bar)	Film cooled length (m) Knuth (1954)	Present model	Grisson's model (1991)
1	612	0.77	1.08	1.18	1.07	1.66
2	900	0.4	1	1.17	1.19	1.25
3	1230	0.29	1	1.19	1.02	0.92

and Morrell (1951) have been used for the comparison. These two experiments are selected due to the following reasons. (i) Earlier models used these experiments for comparison. (ii) The test conditions are totally different for both the experiments. Table 5.1 illustrates the major parameters of these experiments. The following section compares the model predictions with the experimental data. The analytical model is used to study a mixed gas-water system under different operating conditions. The results from these studies are also presented in the subsequent sections.

5.4.1 Comparison with Knuth's experiment

Knuth (1954) conducted tests in a 7.36 cm diameter tube with fully developed flow. Hot exhaust gases were produced by burning fuel and air in a modified turbojet combustion can. Water was used as the liquid coolant. For calculations, the gas properties are taken as those of pure air. Emissivity value of 0.2 is assumed for the core gas, as exact gas composition details are not available from the published data. Comparison is done for relatively low gas temperature to minimize the error. K_t value of 0.2 is assumed in calculations. Grisson (1991) has calculated film cooled length for three test conditions at a coolant flow rate of 0.08 kg s^{-1} m^{-1}. Table 5.2 compares experimental values, values from the present model and Grisson's data. The relative deviation compared to the experimental values was 22%, 8% and 27% for Grisson's model whereas it is 9%, 1.7% and 14% for the present model.

Knuth has also conducted tests with different coolant flow rates. For these tests, other test conditions, viz., chamber pressure, core gas flow rate, and core gas temperature are kept constant. The result of two such experimental conditions is shown in Fig.

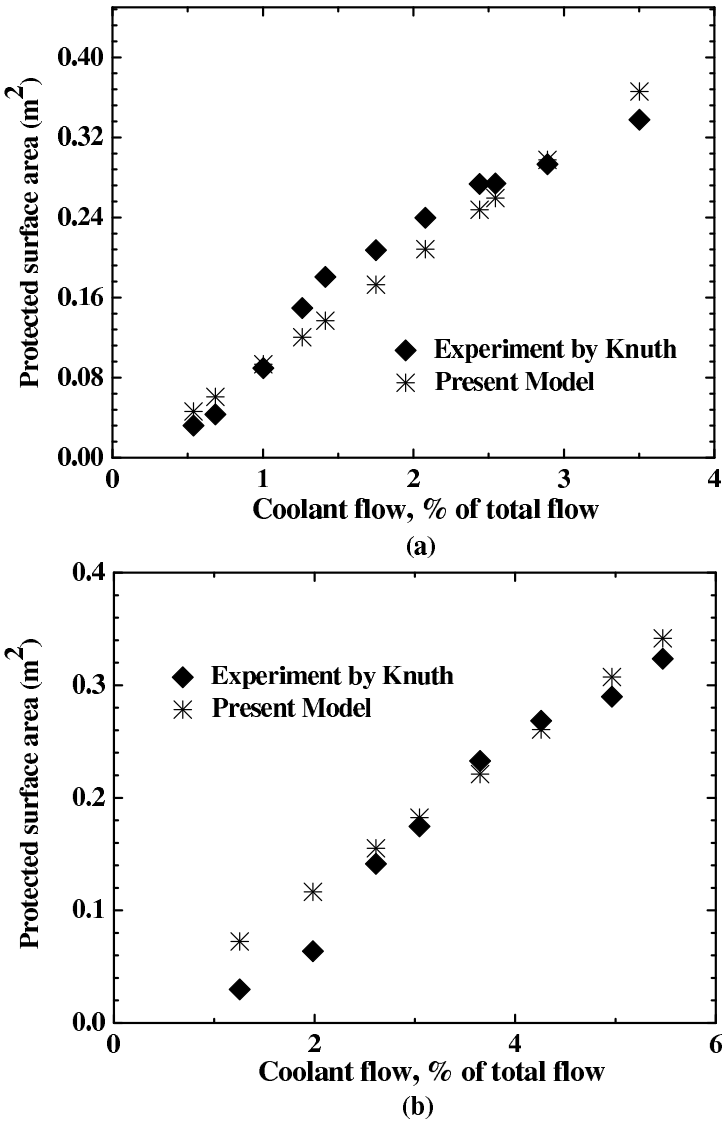

Figure 5.2: Comparison of protected surface area predictions with Knuth (1954) experimental data (a) at T_g = 612 K and $\dot{m}_g$ = 0.77 kg s^{-1}, (b) at T_g = 880 K and $\dot{m}_g$ = 0.39 kg s^{-1}

Table 5.3: Comparisons of model predictions with experimental data and recent models

Case No	T_g (K)	P_{cc} (bar)	Film cooled length (m)			
			Morrell (1951)	Grisson (1991) model	Zhang et al. (2006)	Present model
1	2950	17.6	0.212	0.249	0.190	0.208
2	2963	17.2	0.162	0.198	0.146	0.164
3	2935	17.72	0.099	0.117	0.08	0.08
4	2942	17.93	0.217	0.28	0.216	0.24
5	2960	18.06	0.194	0.23	–	0.18
6	2945	17.24	0.142	0.196	–	0.15
7	2978	17.66	0.146	0.189	–	0.138
8	2963	17.24	0.162	0.198	–	0.164

5.2. The trends of these cases show good agreement. The predicted data approach a value of within 15% of the test data at coolant flow rates higher than 2%.

5.4.2 Morrell's experiment

Morrell's (1951) tests were conducted in a 0.1016 m diameter rocket engine with liquid ammonia-liquid oxygen propellants. The three film coolants studied were water, ethyl alcohol and liquid ammonia. The analysis with liquid ammonia is neglected due to the super critical conditions existed. The core gas composition for each run was calculated based on oxident/fuel ratio (O/F) and lean mixture conditions. An average chamber pressure of 17.6 bar was assumed for calculating liquid coolant properties. Linear extrapolation of test data showed a positive coolant flow (0.73% of the main stream flow) at zero film cooled length indicating coolant loss at injection point. K_t value of 0.1 is assumed in calculations as the coolant injector was 10.9 cm away from the fuel injector.

Table 5.3 shows the variation of film cooled length at different test conditions for the water coolant. The present predictions are compared with the experimental results of Morrell and results from other recent studies. Calculated film lengths showed an

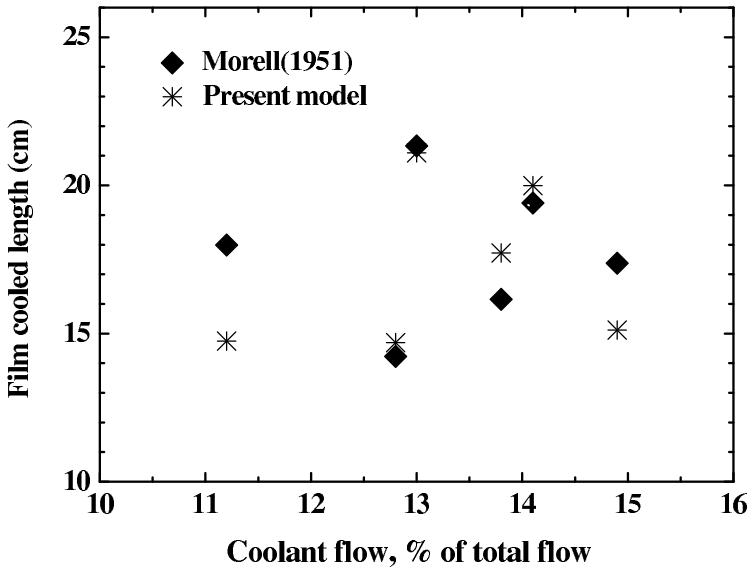

Figure 5.3: Comparison with Morrell's experiment for ethyl alcohol

average deviation of 25% with respect to the experimental values for the Grisson's model, whereas it is 9% for the present model. Zhang's results are available for only four points and the relative deviation ranged from 0.5% to 18%.

Ethyl alcohol tests were conducted with liquid coolant flow rate much higher than the Knuth's (1954) critical value for the formation of large waves. Entrainment calculations showed values as high as 90%. A comparison of calculated and experimental values is given in Fig. 5.3. The model predicts the film cooled length within 1 cm error with a single exception. The global tendency is well predicted and results are better than the Grisson's model. For ethyl alcohol, the experimental values were an average of 2.75 times shorter than that predicted by Grisson. Present model shows an average deviation of 8% in this case.

It is seen that the present model predicts the film cooled length very close to the measured data. The deviations are mainly attributed to the following. The model considers the flow of coolant as continuous wall-jet around the circumference. In actual experimental conditions, the coolant is injected through discrete orifices around the circumference. Therefore the coolant is exposed to the mainstream as a jet and causes increased entrainment. This results in a lower film cooled length in actual experimental conditions. Another reason for the discrepancy can be due to the energy

interactions to the liquid film which is neglected in the present model. Mainly two energy interactions are neglected in the present analysis. (i) the convective heat transfer to the wall. (ii) the energy carried away by the coolant entrained into the gas flow. In test conditions, both these energy interactions contribute and the film cooled length will be different from the predicted values. Noting the approximations in the model proposed and the accuracy range of the test instrumentation used, the predicted data compare well with the test data. It can also be concluded that the present approach can contribute to the improvement of prediction method of liquid film cooled length in rocket combustion chambers operating at subcritical conditions.

5.4.3 Heat flux distributions

The distribution of convective, radiative and total (sum of convective and radiative) heat flux at the gas-liquid interface in the liquid film cooling region for various core gas temperatures is illustrated in Fig. 5.4(a). The calculations are done for Morrell's experimental conditions with a coolant flow of 5% of the gas flow. The radiant heat flux gradually increases as a direct consequence of the increased gas temperature. The convective heat flux increases very slowly and after 2500 K, it almost levels off. This is due to the increase in transpired vapour at high radiant flux conditions. At 2500 K, the convective heat flux is 63% of the total heat flux and is 56% at 3000 K. The radiant heat flux is 58.7% of convective heat flux at 2500 K whereas the ratio is 78% at 3000 K. At temperatures below 1000 K, radiant heat flux is less than 10% of the total flux. The average heat transfer coefficient at a particular core gas temperature is calculated from the total heat flux value. The variation of convective heat transfer coefficient and a representative radiation heat transfer coefficient defined by $\dot{Q}_{rad}/\Delta T$ is shown in Fig. 5.4(b).

5.4.4 Effect of gas Reynolds number

Two conditions considered for analysis are (i) constant coolant flow rate, and (ii) constant mass flow ratio of the coolant and core gas. The variation of (L_c/D), E and

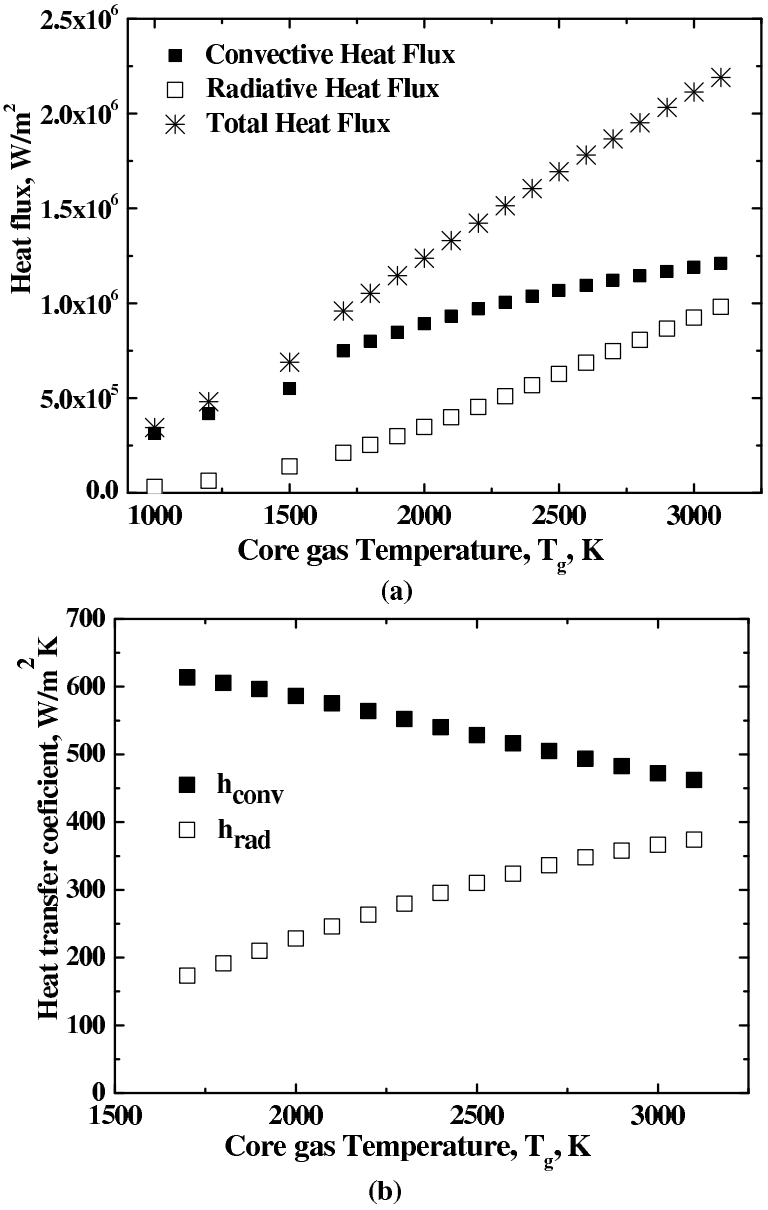

Figure 5.4: Heat flux distributions (a) Distribution of convective, radiant and total heat flux at various core gas temperatures for constant coolant flow rate, (b) Variation of heat transfer coefficients vs core gas temperature.

Nu at different gas Reynolds number for different T_g is obtained. Figure 5.5 shows the variations at constant coolant flow rate. At high gas Reynolds numbers, axial velocity of gas increases causing enhancement of convective heat transfer. It is clearly observed that Nusselt number Nu increases with Re_g as shown in Fig. 5.5 (a). An increase in the liquid entrainment rate is also observed at high Re_g [Fig. 5.5(b)]. The increase of convective heat transfer accelerates the liquid film evaporation and high entrainment causes loss of more coolant available for film cooling. The liquid film length decreases with increase of Re_g due to these effects [Fig. 5.5(c)]. Figure 5.6 shows the variations at constant mass flow ratio. At constant mass flow ratio conditions, the coolant flow rate increases along with Re_g, causing an increase in liquid film length initially. But the increase in convective heat transfer [Fig.5.6(a)] and a nonlinear increase of entrainment [Fig.5.6(b)] causes a decrease in liquid film length at high Re_g. This transition occurs at low Re_g when the gas temperature is high as illustrated in Fig. 5.6(c).

5.4.5 Effect of coolant inlet temperature on liquid film cooled length

Figure 5.7 demonstrates the effect of inlet coolant temperature on film cooled length. As expected, as the inlet coolant temperature increases, energy required to heat the coolant to its saturation temperature decreases and more energy is available in vaporizing the film, leading to shorter liquid film length. The trend is same at various combustion chamber pressures as demonstrated in the figure.

5.4.6 Effect of combustion chamber pressure on liquid film cooled length

Figure 5.8 (a) shows the effect of combustion chamber pressure on the liquid film length. The result indicates that the liquid film length increases gradually with increase of pressure and then almost levels off. At high pressures, the energy required to vaporise the liquid increases marginally. The radiative heat transfer increases due to

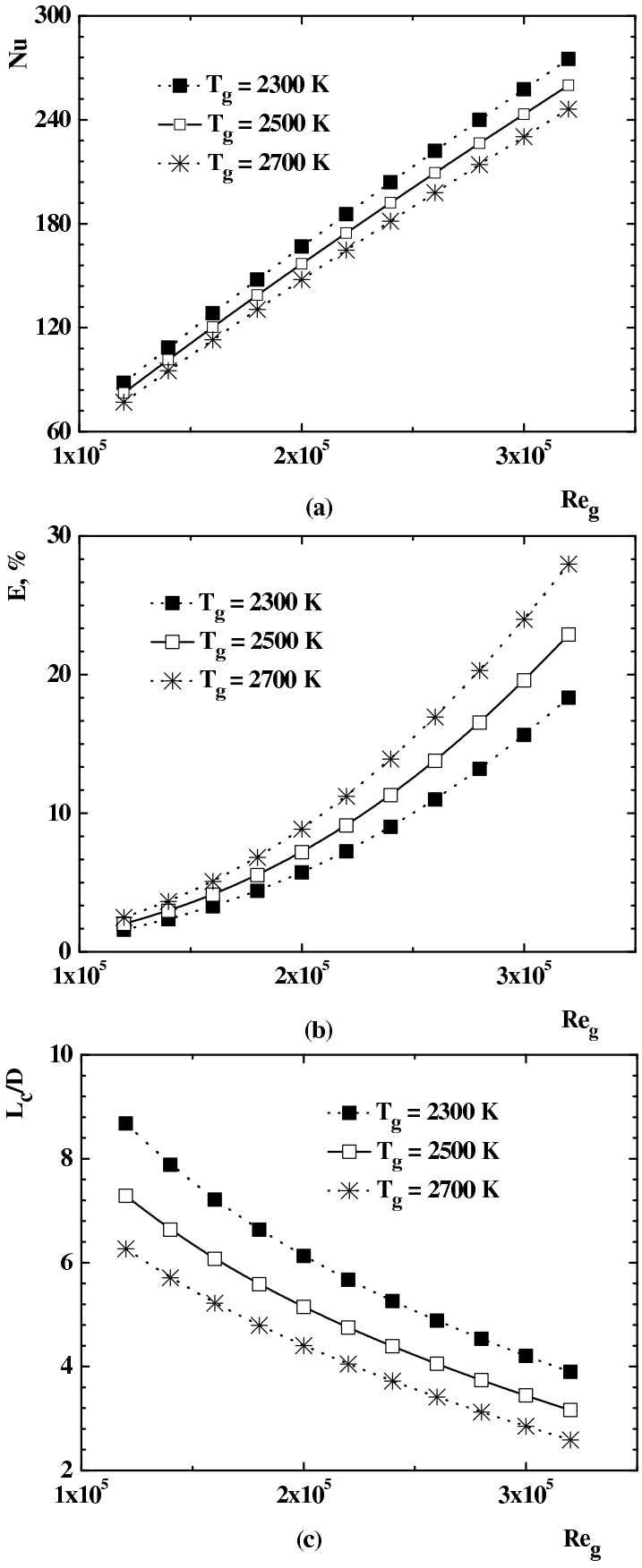

Figure 5.5: Effect of Re_g for constant coolant flow rate. (a) variation of L_c, (b) variation of entrainment fraction, (c) variation of Nu

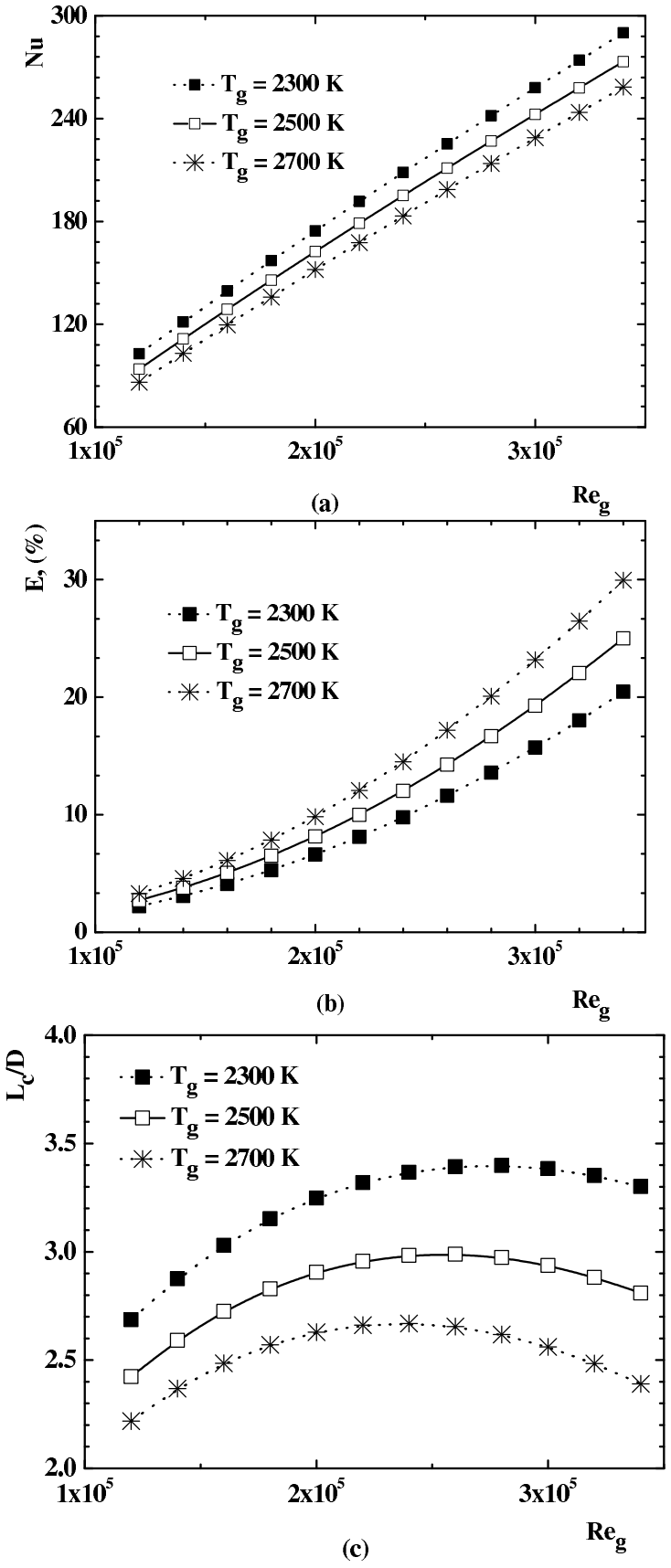

Figure 5.6: Effect of Re_g for constant mass flow ratio (a) variation of L_c, (b) variation of entrainment fraction, (c) variation of Nu

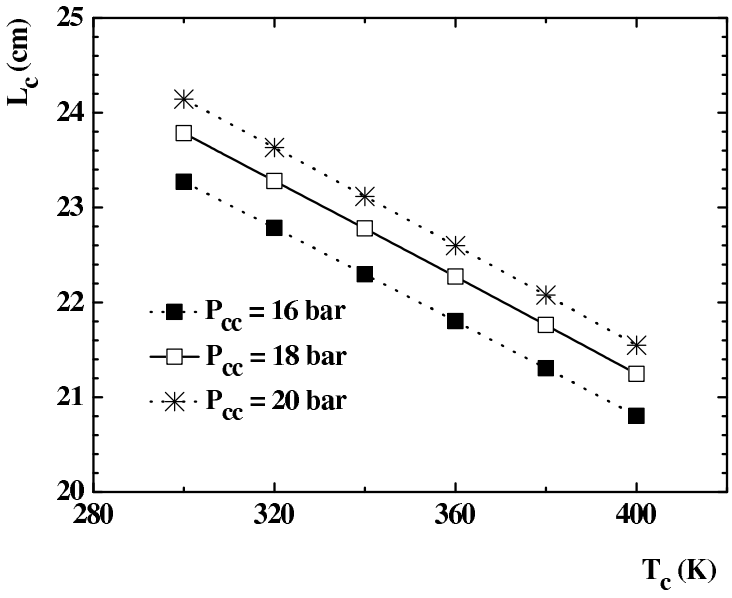

Figure 5.7: Effects of coolant inlet temperature on liquid film length at various combustion chamber pressures

increase in emissivity with pressure as shown in Fig. 5.8 (b). These effects favours the reduction in the film length. More liquid evaporation causes an increase in transpired vapour which in turn reduces the convective heat transfer coefficient [Fig. 5.8(c)]. The entrainment rate decreases with increase in pressure as shown in Fig. 5.8(b). The combined effect of all is an increase in film cooled length.

5.4.7 Effect of mass flow ratio

Figure 5.9 shows the effects of mass flow ratio of liquid coolant to the free stream gas. Relative variation of h_c, E and L_c with respect to the respective values at a mass flow ratio of 1.5% is plotted. The increase in film length is mainly due to the increase in film coolant flow at higher mass flow ratio. Marginal decrease in convective heat transfer coefficient is noted. This is due to the increase in velocity of coolant, resulting in a decrease in relative velocity of the free stream with respect to the liquid surface. A decrease in entrainment is observed and is due to the increase in coolant Reynolds number.

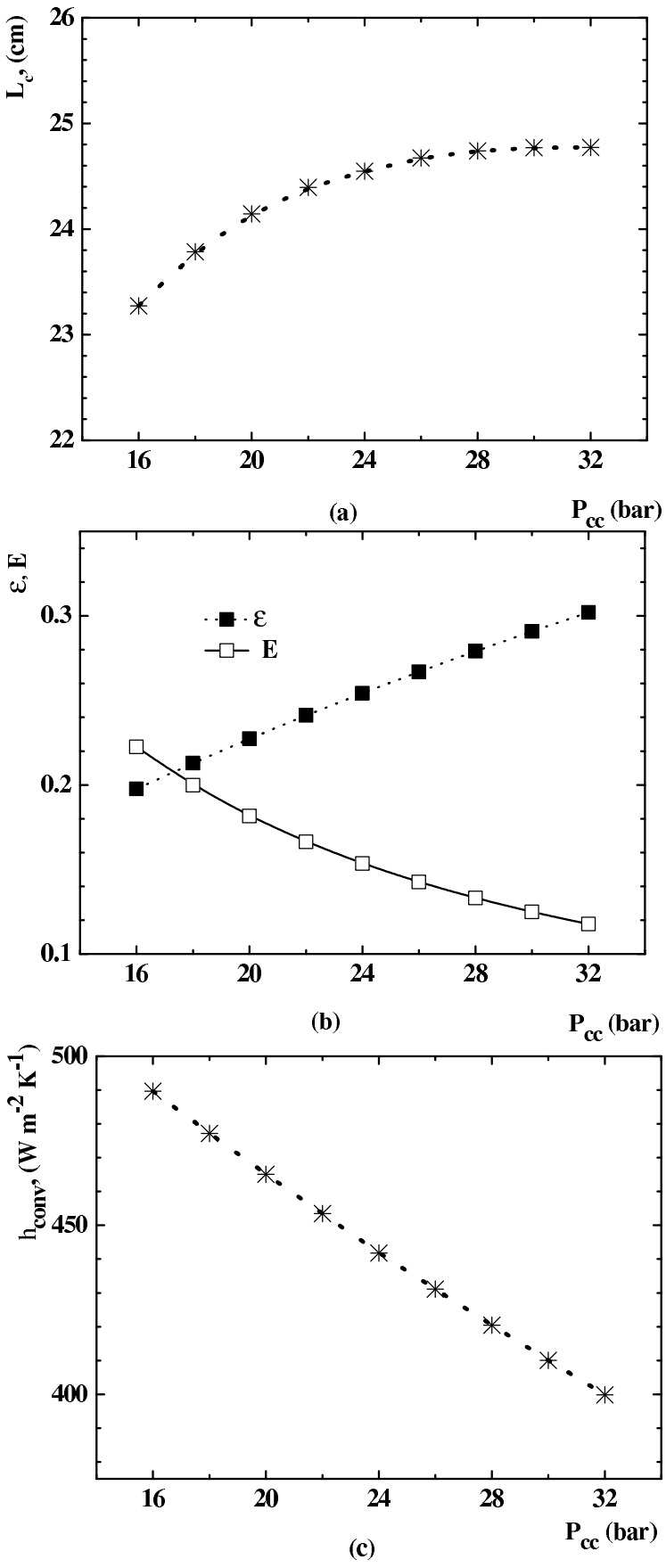

Figure 5.8: Variation of properties with combustion chamber pressure, (a) $\epsilon \& E$, (b) L_c,(c) h_{conv}

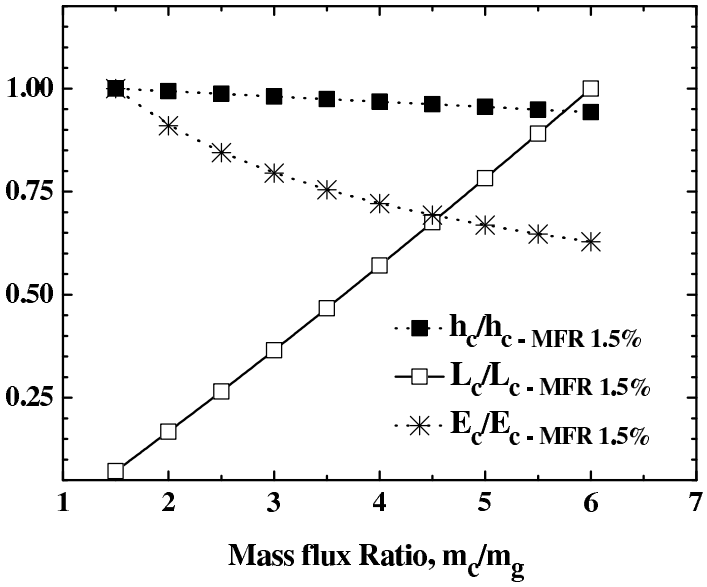

Figure 5.9: Effect of mass flow ratio(MFR) on L_c, E and h_c

5.5 Conclusions

A one dimensional analytical model of liquid film cooling in rocket combustion chambers operating at subcritical conditions is proposed. The model is based on a control volume approach and a fundamental energy balance concept. Reliable correlations are adapted from literature for calculating these energy interactions. Key assumptions such as steady one-dimensional flow, adiabatic film-wall interface, non reactive coolant and constant core gas temperature had to be made in order to develop this fundamental model. Entrainment model of annular two phase flow is extended for predicting entrainment rate. Model is tested against experimental data for liquid film cooling in rocket combustion chambers available in literature. The method predicts protected surface area within 15% in the case of Knuth (1954)'s experiment , and is within 9% for liquid film length in the case of Morrell (1951). It may be noted that the accuracy of film cooled length predicted by existing models vary up to 27% compared to the 15% seen with the present model. The results of this study show that the effects of radiation and coolant entrainment are significant.

CHAPTER 6

SIMULATION III: PROPERTIES OF DISTURBANCE WAVES IN LIQUID FILM COOLING FLOWS

In this chapter, liquid-gas interface characteristics associated with liquid film cooling flows are analysed using a two-dimensional multiphase computational model. Geometry and flow parameters used in this study are derived from the work of Kinney et al. (1952). Details of numerical simulation and the most relevant results obtained from the study are discussed in detail. Note that the contents of this chapter is based on Shine et al. (2013b).

6.1 Introduction

The analytical model developed in Chapter 5 showed that film coolant entrainment results in significant reduction of liquid film cooled length. Mass transfer via entrainment process causes loss of the film coolant and it is therefore important to understand the pertinent liquid-gas interface characteristics associated with the liquid film cooling flow field. The study aims to bring out the features relating to the development of waves, its deformation under the action of high momentum core gas flow and the associated liquid entrainment phenomenon. The objective is to develop a numerical model to predict the interface characteristics for a variety of imposed parameters and momentum flux ratios. The model is expected to have the capability to analyse the parameters related to the liquid-gas interface waves, namely, wave velocity, frequency, amplitude and wave length.

6.2 Experiments Used for Validation

The computational simulations are validated by comparison to experimental work by Kinney et al. (1952). Kinney used transparent test sections of 50.8 mm and 101.6 mm diameter for conducting experiments to observe liquid film flows. Porous-surface and jet-type injectors were used to inject the film coolant. The injectors provided uniform distribution of coolant around the circumference. Observations of the liquid film were made by using a transparent tube illuminated by a stroboscopic light. Shadowgraph pictures of the liquid film were obtained using a microscopic light source, condensing lenses and a camera. Pictures of the liquid film were obtained using a camera with a speed of 2000 frames per second. Experiments were conducted with the core gas flow Reynolds numbers from 2.2 to 29×10^5. Flows of water, water-detergent solutions and aqueous ethylene glycol solutions (which varied viscosity and surface tension) were investigated. Coolant flows varied from 0.3 to 21 % of the core gas flow.

6.3 Details of Numerical Simulation

A 2-dimensional axi-symmetric numerical model, developed using the finite-volume formulation, is used in the present study. The details of geometry, boundary conditions and the grid are described below, followed by the governing equations and solution methodology.

6.3.1 Geometry, boundary conditions and grid

The geometry of the present computational model is based on the Kinney's test set up. The computational domain with the dimensions for the 50.8 mm diameter pipe is shown in Fig. 6.1. Simulations are also carried out for the 101.6 mm diameter pipe with similar coolant inlet slot width. The tube length is set to 500 mm as this will satisfy the simulation objective with a minimum computational time. Because the flow is expected to be axi-symmetric, a two-dimensional axi-symmetric model is

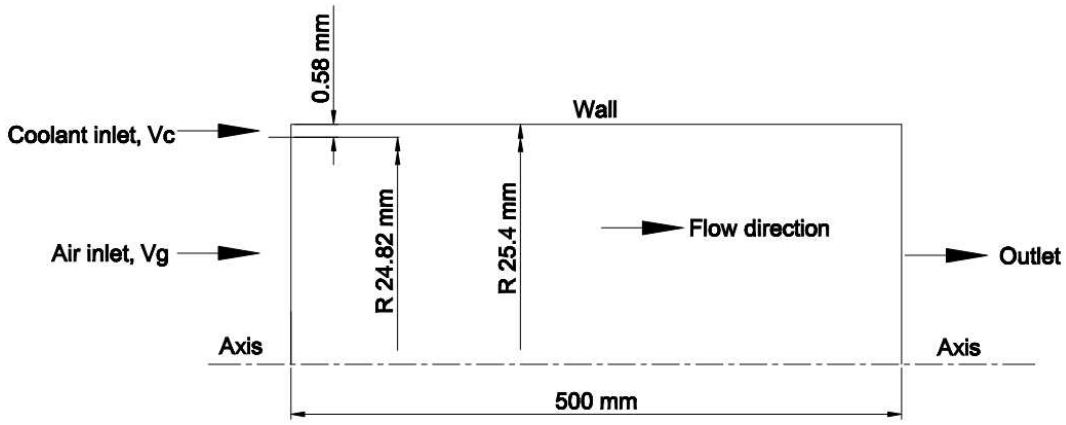

Figure 6.1: Schematic of the computational domain

considered for computations. The simulation domain is bounded by the coolant and air inlet, outlet, tube wall, and tube axis.

Coolant velocity varied from 0.1 m/s to 6 m/s which correspond to measured flow rates. Air is supplied through the gas portion of the inlet section at constant flow rates. Pressure inlet condition with static pressures ranging from 1.42 to 2.5 bars absolute is applied for core gas flow. Volume fraction of water at this portion of the inlet was set to 0, meaning no water flow. Turbulence intensity and hydraulic diameter are used to specify the turbulence parameters. The turbulence intensity levels were not measured in the experiment. Approximation for the computational model is based on the equation, $Tu = 0.16 \times Re^{-1/8}$. The hydraulic diameter for coolant is kept same as two times the width of the coolant inlet annulus. A no-slip boundary condition is assumed at the tube wall. An outflow boundary condition is applied at the tube outlet. Initial conditions in the simulation are selected based on the experimental conditions. At t = 0 s, the tube is full of air. As far as the velocities, both radial and axial velocities in the tube are set to 0 m/s at t =0 s. Temperature of both phases are assumed as 300 K for all computations. Air is set as primary phase and water as secondary phase for the simulations. However, the results are not affected by the selection of air as primary phase. Air and water properties are listed in Table 6.1.

Table 6.1: Properties of air and water

Phase	Density, kg m^{-3}	Viscosity, kg m^{-1} s^{-1}
Air	1.225	1.7894×10^{-5}
Water	998	1.003×10^{-3}

6.3.2 Governing equations with solution methodology

Continuity, momentum, and RNG k-ϵ turbulence model are solved to predict the velocity fields. Details of the turbulence model equations are described below.

Turbulence modeling

Variants with superior performance over the standard k-ϵ model have been proposed by researchers for turbulence modelling. The RNG k-ϵ model and realizable k-ϵ model are two types of its variants used in situations where the flow features include strong streamline curvature, vortices, and rotation.

The realizable k-ϵ model is a relatively new model that was proposed by Shih et al. (1995). It differs from the standard k-ϵ model in two important ways: (i) it contains a new formula for μ_t; and (ii) a new form of transport equation for ϵ is derived. The second feature makes it more capable of accurately predicting the spreading rate of both planar and round jets. This type of k-ϵ model, by its nature, is also a high Reynolds number turbulence model. Initial studies by Shih et al. (1995) and Kim et al. (1997) showed that it provides best performance in separated flows and flows with complex secondary flow.

Yakhot and Orszag (1986) proposed the RNG k-ϵ model. This was derived from the instantaneous N-S equations using the "renormalisation group" method. The main difference between this and the standard model are: (i) it contains a new term in its ϵ equation which greatly improves the accuracy of simulating rapidly strained flows; (ii) the RNG model uses an analytical formula to calculate turbulent Prandtl numbers; and (iii) it uses an analytically derived differential equation for the effective viscosity that

accounts for low-Reynolds-number effects. Due to these features, the RNG k-ϵ model is selected for the current simulation work since the liquid coolant flow is similar to the flow in the near wall region. The RANS equations for all the turbulent models are given in section 3.2.2. The additional transport equations for the turbulent kinetic energy 'k' and dissipation rate 'ϵ' used in the RNG model for the present study are

$$\frac{\partial}{\partial t}(\rho k) + \frac{\partial}{\partial x_i}(\rho U_i k) = \frac{\partial}{\partial x_j}\left(\alpha_k \mu_{eff} \frac{\partial k}{\partial x_j}\right) + G_k - \rho\epsilon \tag{6.1}$$

and

$$\frac{\partial}{\partial t}(\rho \epsilon) + \frac{\partial}{\partial x_i}(\rho U_i \epsilon) = \frac{\partial}{\partial x_j}\left(\alpha_\epsilon \mu_{eff} \frac{\partial \epsilon}{\partial x_j}\right) + C_{1\epsilon}\frac{\epsilon}{k}G_k - C_{2\epsilon}\rho\frac{\epsilon^2}{k} + R_\epsilon \tag{6.2}$$

G_k is the production of turbulent kinetic energy and is calculated as

$$G_k = -\rho\overline{u_i' u_j'}\frac{\partial U_j}{\partial x_i}, \text{ and} \tag{6.3}$$

α_k and α_ϵ are the inverse effective Prandtl numbers for k and ϵ. They are computed using the following formula derived analytically from the RNG theory

$$\left|\frac{\alpha - 0.3929}{\alpha_0 - 1.3929}\right|^{0.6321}\left|\frac{\alpha - 2.3929}{\alpha_0 - 2.3929}\right|^{0.3679} = \frac{\mu}{\mu_{eff}}, \tag{6.4}$$

where $\alpha_0 = 1.0$, and μ_{eff} and μ are the effective viscosity and fluid physical viscosity, respectively. R_ϵ is an additional term that makes the RNG model different from the standard k-ϵ model. It is given by

$$R_\epsilon = \frac{C_\mu \rho \eta^3 (1 - \eta/\eta_0)\epsilon^2}{(1 + \beta\eta^3)k} \tag{6.5}$$

where $\eta = sk/\epsilon$ (S is the modulus of strain rate tensor), $\eta_0 = 4.38$, and $\beta = 0.012$. $C_\mu, C_{1\epsilon} and C_{2\epsilon}$ are constants. The values of $C_\mu, C_{1\epsilon}$ and $C_{2\epsilon}$ are 0.0845, 1.42 and 1.68, respectively. A differential equation is used to calculate the turbulent viscosity,μ_t

where

$$\frac{d\left(\rho^2 k/\sqrt{\epsilon\mu}\right)^{'}}{d\nu} = 1.72\frac{\nu^{'}}{\sqrt{\nu^{'3}-1+C_\nu}} \tag{6.6}$$

and $\nu^{'} = \mu_{eff}/\mu$ (turbulent kinematic viscosity),C_ν = 100, and $\mu_{eff} = \mu + \mu_t$.

VOF Model

Volume of Fluid (VOF) method is used to track the volume fraction of each of the fluids throughout the domain. This model has been successfully employed to a wide range of multiphase flow cases. The VOF methods are designed for modelling two or more immiscible fluids by solving a single set of momentum equations and tracking the volume fraction of each of the fluids throughout the domain. These methods do not directly track the interface; instead they reconstruct the interface. Geometric reconstruction scheme is adopted to reconstruct the gas-liquid interface. This scheme represents the interface between fluids using a piecewise-linear approach. The PLIC (piecewise linear interface calculation) VOF methods are devised by Youngs (1982) and are the most successful and "have proven to be robust and reasonably accurate... " Benson (2002). It assumes that the interface between two fluids has a linear slope within each cell, and uses this linear shape for calculation of the advection of fluid through the cell faces.

In two-phase flows, surface tension will shape the waves on the interface and hence the effects of this force are included in the VOF model adopted in this work. The surface tension scheme used for the VOF model is the continuum surface force (CSF) model proposed by Brackbill et al. (1992). With this model, the surface tension is treated as a source term in the momentum equations. A value of 0.072 N/m (Kinney et al., 1952) is set to the air-water interface surface tension.

Pressure based solver, wherein a pressure (pressure correction) equation is used to achieve the constraint of mass conservation of the velocity field, is used along with a segregated algorithm. The model used implicit discretization schemes for the momentum, k, and ϵ transport equations and first-order explicit time-marching scheme

Table 6.2: Summary of the model configuration

Item		Model configuration
Phases in VOF model	Air	Primary phase
	Water	Secondary phase
Discretization schemes of convective governing equations	Pressure	Body force weighted
	Pressure-velocity coupling	PISO
	Momentum equation	Second order upwind
	Turbulent kinetic energy	Second order upwind
	Turbulence dissipation rate	Second order upwind
Relaxation factors for all variables		1.0

to solve the time dependent continuity equations for the volume of fractions. More model configuration details are presented in Table 6.2. Computation of the flow variables with the model converged for every grid and coolant flow regimes tested with scaled residuals less than 10^{-3}, where a residual represents an average imbalance in a cell for each flow variable. The core gas velocities are very high and the mesh size are smaller. Therefore, very small time steps are required in the simulations. The initial time step is taken as 10^{-7}. Time steps are refined further during the simulation as the core gas velocity increase due to the contraction of the gas core near the wave peak region.

6.4 Results and Discussions

6.4.1 Waves on the liquid-gas interface

Liquid-gas interface surface appeared smooth at low coolant flow rates and constant core gas conditions. Disturbances having the appearance of waves are noticed at higher coolant flows. Fig. 6.2 shows disturbance waves present at the liquid-gas interface. The disturbance waves started appearing on the liquid-gas interface after a finite distance (w_l) from the coolant injection location. Film thickness is almost constant up to the wave inception point indicating no entrainment of the liquid till that point. In

the simulation, the wave inception point is located based on the variation in film thickness. The point where the film thickness varied more than 10% of the average value in the near injection region (x/D < 0.5) is located and is identified as wave inception point. These waves are found propagating downstream in the axial direction. Wave is relatively steep on the leeward side whereas it is relatively smooth on the windward side. It is also observed that the waves are dynamic and is continuously developing over time. The wave length and wave amplitude are found to be changing during their progress in the flow. Simulations have been carried out to predict the wave characteristics for a variety of imposed parameters and momentum flux ratios and the results are described in the succeeding sections.

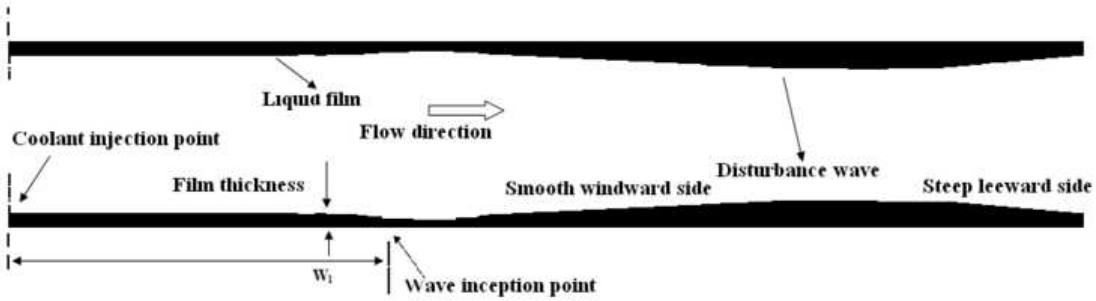

Figure 6.2: Waves at the liquid-gas interface

6.4.2 Grid independence study

Structured grids of quadrilateral type are employed in the study to provide the highest grid quality. Intensive and high quality grids are used to capture the interaction and jet characteristics. Simulations are done with different types of grids varying with the resolution by a factor of about 2 between each other. Grid independence study is conducted with a core gas Reynolds number of 4.3×10^5 and a coolant velocity of 1 m/s (I = 0.05). The wave parameters, wavelength and the distance toward the first wave center have been compared for different meshes. Table 6.3 shows the number of cells for different meshes and the wave parameters for the 50.8 mm diameter pipe. The results obtained for medium and fine grids are similar and solution becomes grid

Table 6.3: Comparison of wave parameters: Location of wave and wave height for the 50.8 mm diameter pipe

Mesh type	No. of cells	Distance of first wave center from injection point, mm	Wave height, mm
Coarse	4400	≈25	≈ 0.43
Medium	8400	≈22	≈ 0.30
	16960	≈22	≈ 0.30
Fine	32560	≈22	≈ 0.30

Table 6.4: Computational model validation:- Comparison between the experiment and simulation

Pipe diameter	Core gas Re_g	Blowing ratio, M for the transition flow, $V_c\rho_c/V_g\rho_g$	
mm		Data from Kinney et al. (1952)	Results from current simulation
101.6	4.1×10^5	0.89-1.08	≈1.1
101.6	5.9×10^5	0.61-0.8	≈0.8
50.8	2.2×10^5	0.66-0.95	≈0.9
50.8	3.1×10^5	0.66-0.96	≈0.9

independent after medium grid. Therefore medium grid is used for CFD simulation and has a total size of 8400 cells.

6.4.3 Comparisons to Experimental Work

Kinney et al.'s (1952) experiments with different coolant flow rates revealed changes in the interface surface pattern. He observed disturbances appearing at high coolant flows. Kinney termed these flow rates as transition region from smooth flow to highly disturbed flow. Table 6.4 compares the values, from the current simulation and the experiment, of the blowing ratio defining the transition region for the different flow conditions. It shows good agreement between both experimental data sets and the present computations for the transition region at various core gas flow conditions. The wide range in experimental values are attributed to the experimental uncertainties existing as the experimental results are based on the visualisation of a thin film of liquid (of the order of ≈ 0.1 mm) with the help of stroboscopic light.

Table 6.5: Effect of liquid surface tension on liquid flow transition:- Comparison between the experiment and simulation

σ, surface tension	Blowing ratio, M for the transition flow, $V_c\rho_c/V_g\rho_g$	
Nm^{-1}	Values from Kinney et al. (1952)	Results from current simulation
0.072	0.61-0.8	≈0.8
0.055	0.67-0.96	≈0.95
0.045	0.74-1.05	≈1.1

Kinney has observed an increase in the magnitude of the transition flow region with decrease in surface tension. Table 6.5 demonstrates that the result of the numerical simulation is consistent with the experiments. The simulations are done for the 0.101 m diameter pipe with the mainstream Reynolds number of 5.9×10^5. The global tendency is well predicted in all the cases.

6.4.4 Effect of coolant flow rates

Simulations are conducted with various coolant flow rates with velocities ranging from 0.25 m/s to 6 m/s for the 50.8 mm diameter pipe. Changes in flow field configurations are noticed for different coolant flow rates. These changes occurred gradually along the length of the tube at higher flow rates. The length at which disturbance first occurred (length where the film thickness varied more than 10% of the average value in the near injection region, w_l) is noted for various coolant flow rates and is plotted in Fig. 6.3. Figure shows the logarithmic variation of the non-dimensional distance (w_l/D) with the momentum flux ratio (I) between the coolant and the core gas. It is observed that the non dimensional distance w_l initially increases with the momentum flux ratio and asymptotically approaches a constant value at higher momentum flux ratios. Disturbances are present on the liquid film surface for all coolant flow rates above a critical value, and for lower coolant flow rates it started appearing very near to the injection point. However, the wave length and wave height are smaller at low coolant flow rates as demonstrated in Fig. 6.4. The appearance of the waves at different coolant flow rates are shown in Fig. 6.4.

The wave height increased from 0.4 mm to 0.9 mm for the coolant velocities ranging from 0.25 to 6 m/s. The waves propagated downstream in the axial direction after generation. The waves appeared to be regular and less chaotic than observed from annular flow experiments by Andreussi et al. (1985). This may be due to the use of time averaged k-ϵ equations in the simulation as time averaging of the turbulent quantities make it difficult to model the unsteady phenomenon that occur within the timescales of the same order as those of the turbulent fluctuations.

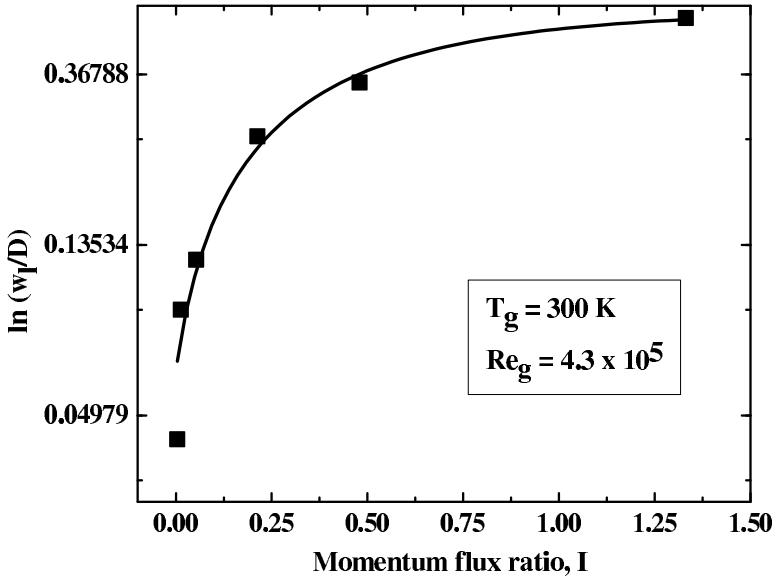

Figure 6.3: Location of wave inception point with momentum flux ratio

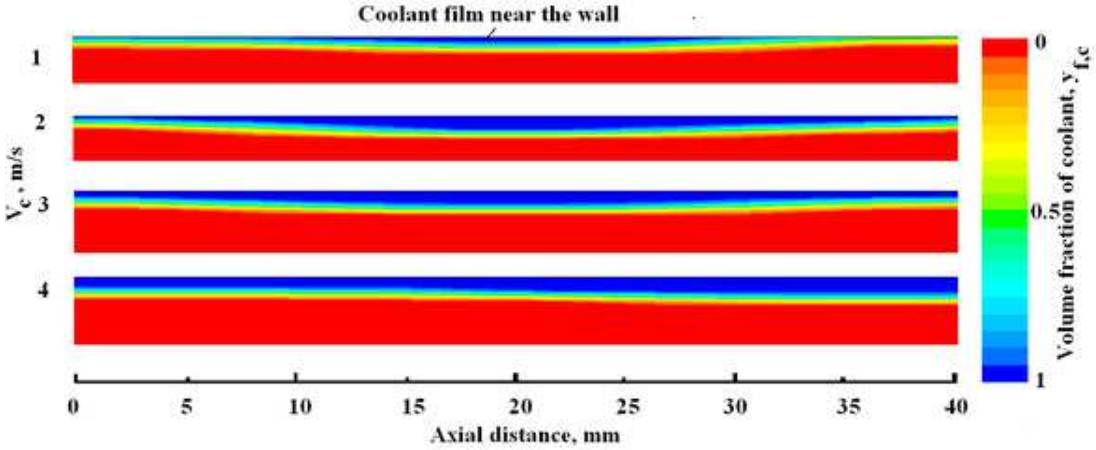

Figure 6.4: Shape of the liquid-gas interface at various coolant flow rates

6.4.5 Effect of core gas velocity

The behavior of liquid-gas interface is observed for various core gas velocities. The coolant flow conditions are kept constant for all the simulations. Simulations are carried out for the 50.8 mm diameter pipe. The momentum flux ratios (I) are kept at 3.62, 0.9, 0.23 and 0.05. At low momentum flux ratios, the interface showed similar characteristics as described in the previous section. The region of inception of disturbance waves shifted away from the coolant injection point as 'I' increased from 0.05 to 0.9. However, the disturbances have different appearances at various momentum flux ratios. Figure 6.5 shows waves at four different momentum flux ratios at the same location and at the same time step. In all the cases, the waves resemble the characteristics of a disturbance wave. The upstream side of the wave is short whereas the downstream side has started protruding into the gas core. It is observed that the protruding part continues to grow as 'I' increases. The protrusion of the downstream wave has clearly moved towards the tube axis and is being stretched in the flow direction for the case I = 3.2. This indicates higher entrainment at higher momentum flux ratios. It is to be noted that similar entrainment mechanism was noticed by Han and Gabriel (2007) at higher gas velocities. It can also be seen that the film thickness decreases significantly with the increase in gas flow rate for the same liquid flow rate.

The different flow conditions obtained by changing the coolant flow rate and core gas velocity have resulted in a variety of momentum flux ratio conditions. It is observed that in both cases, as momentum flux ratio increases, longer wavelength disturbances started appearing on the surface of the film. It is attributed to the increase in film thickness at high momentum flux ratios. The longer wavelength disturbances will result in regions with relatively large quantities of liquid collected. Such regions will cause higher entrainment of liquid droplets as seen in Fig. 6.5.

6.4.6 Comparison of pipe sizes

Previous studies have reported pipe diameters to have significant effect on the periodic structures of the two-phase flow in the vicinity of the film (Robert, 1990; Kaji and

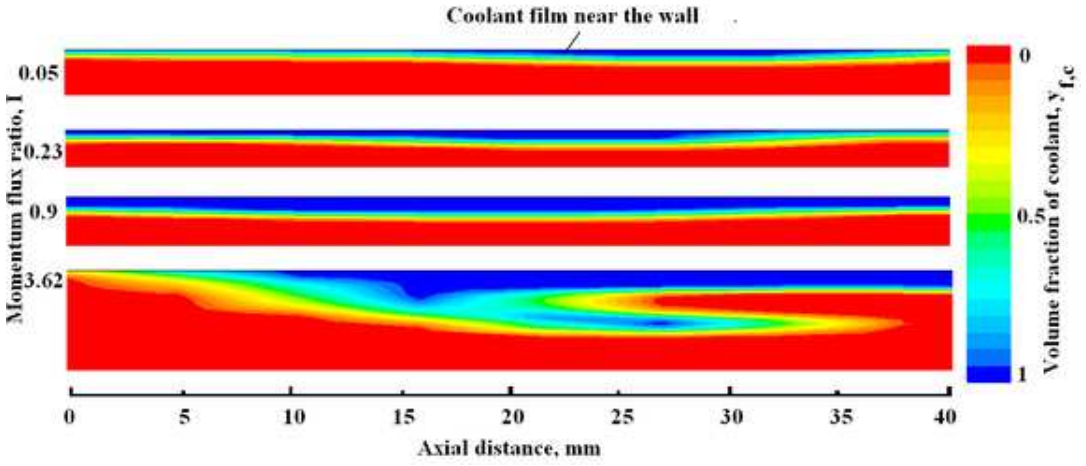

Figure 6.5: Shape of the liquid-gas interface at different momentum flux ratios

Azzopardi, 2010). Therefore, simulation results from the two pipe sizes are compared to determine the effect of diameter on the liquid-gas interface characteristics of film cooling flows. Computations are done at various momentum flux ratios for the two pipe diameters of d = 50.8 mm and 101.6 mm. Simulations are carried out for these pipe sizes only due to the availability of experimental results (Kinney et al., 1952). The film thickness at a location 50 mm away from the coolant injection, for different pipe diameters are shown in Table 6.6. This location is selected for comparison based on the fact that the inception of disturbance waves are found to exist only beyond this point for all cases investigated. The data shows two distinct trends. viz; (i) The variation of film thickness at different momentum flux ratios; higher momentum flux ratios resulted in thicker film irrespective of the pipe diameter which is attributed to the presence of more coolant near the wall, (ii) The variation of thickness at different pipe diameters. The film thickness appears to have a much lower dependence on pipe diameter as marginal increase in film thickness is observed for large diameter pipe for various momentum flux ratios. It was reported that entrainment correlation developed based on the experiments in small diameter pipes tend to over predict in the case of large diameter pipes (Robert, 1990). This was attributed to the increasing asymmetric film distribution at large diameters. In film cooling applications, the coolant flow is uniformly distributed around the circumference. Therefore, no appreciable difference is expected for different diameters. It is observed that the disturbances have the same

Table 6.6: Effect of pipe diameter on film thickness

			Film thickness, mm	
V_c	V_g	Momentum flux ratio, I	Pipe dia = 50.8 mm	Pipe dia = 101.6 mm
1	60	0.23	0.4	0.5
1	30	0.9	0.64	0.7
1	15	3.6	0.9	0.92

appearance for corresponding momentum flux ratios at all diameters. The region of inception of disturbance waves shifted slightly away from the injection point at higher diameters. It may be attributed to the changes in film thickness observed at higher pipe diameters. However, it may be noted that a thorough experimental and numerical investigation of various pipe diameters are required to confirm the above findings.

6.4.7 Wavelength of disturbance wave

Figure 6.6 shows the analysis of computational data on wave length of disturbance wave for the 50.8 mm diameter pipe. The variation of wavelength at different core gas velocities and at coolant velocities is obtained and plotted. Disturbance wavelength represents the average distance between two consecutive waves. In the present analysis, the average value is calculated considering the first three successive waves present at the liquid-gas interface. It is observed that the variation is less at higher gas velocity. At higher gas velocities, disturbance waves are more regular and closer without coalescence of successive waves. Therefore, the wavelengths are almost constant at higher gas velocities.

Variation of wavelength of disturbance wave with coolant velocity is also shown in Fig. 6.6. As the coolant velocity increases for a given gas velocity, the liquid film thickness increases which in turn causes an increase in wave wavelength. However the curve show an asymptotic behaviour indicating a limiting value for wavelength at higher coolant flow rates. It is observed that the variation in wavelength is more dependent on the coolant velocity compared to the core gas velocities. However, at higher coolant velocities, the wave properties are not affected too much. It indicates

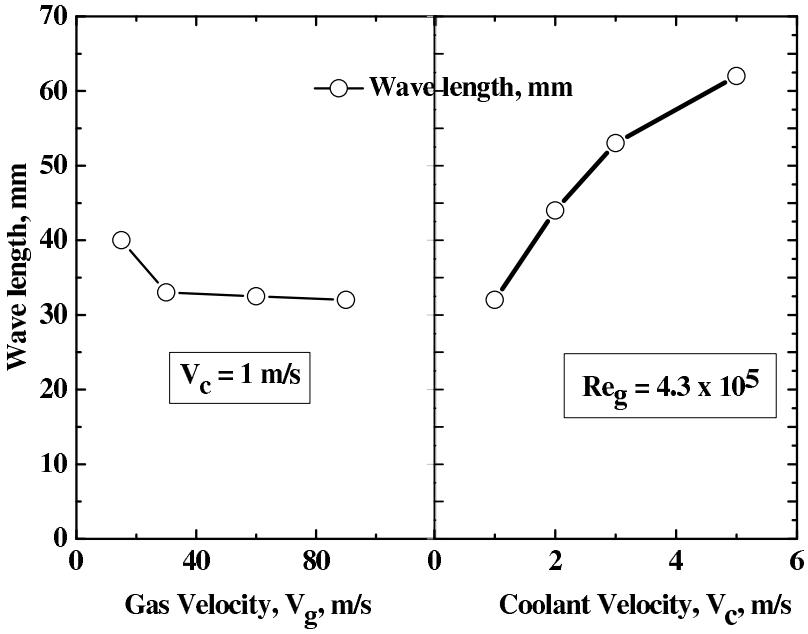

Figure 6.6: Variation of wave amplitude and wave velocity with core gas velocity

the presence of a second transition coolant flow rate beyond which there is no appreciable change in wave properties.

6.4.8 Free-stream turbulence effects

In order to study the effect of higher free-stream turbulence, simulations are carried out at high free-stream turbulence values viz., 8, 14 and 20%. Simulations are carried out for a gas Reynolds number of 4.3×10^5 and at V_c = 0.12 m/s. Figure 6.7 shows the coolant film developed near the wall for the three turbulence intensity levels. The liquid-gas interface appears to be of similar nature. This is expected as the simulations are conducted at a flow rate less than the coolant flow rate required for producing the disturbed flow. A decrease in liquid film length is noticed at higher free stream turbulence levels. This is due to the increased mixing of the coolant at the interface and the associated coolant loss. However, the interface images are regular and much less chaotic. This is due to the time averaged or ensemble-averaged results produced by k-ϵ model. Moreover, the interface surface in figure is created with cells having a mass fraction of 0.5 and above. Therefore, mixing of the coolant and the associated entrainment at small levels is not visible.

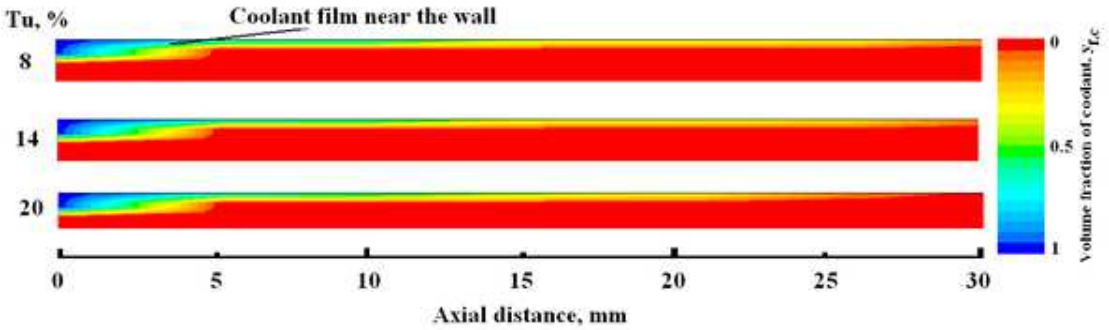

Figure 6.7: Coolant film developed near the wall at various turbulence intensity levels

6.4.9 Roll wave flow parameters

Roll wave frequency is defined as the number of roll waves passing through a given point per second. Roll wave frequency is obtained from the present computational model by a monitoring surface defined at a distance of 75 mm from the coolant injection location. The film thickness at this location is recorded for every time step of 0.001 s and the wave frequency is obtained by inversing period of thickness peak as shown in Fig. 6.8. Table 6.7 illustrates the wave frequency obtained for the three cases investigated. It can be noted that the wave frequency mainly depends on the core gas Reynolds number. Figure 6.9 shows the non-dimensional film thickness variation for two air flow rates, $\mathrm{Re}_g = 4.3\times10^5$ and 2.1×10^5. The coolant velocity is kept constant at 1 m/s. The influence of core gas velocity on wave frequency and film thickness is apparent. The following observations can be made from the figure; (i) The film thickness is more at low core gas flow rates (or at high momentum flux ratios). (ii) The wave frequency increases with the increase in core gas flow rate. (ii) Rapid variation in film thickness in the axial direction at high core gas flows. (iv) The waves are dynamic at higher core gas flows and are continually changing their shapes under the action of the gas flow. Figure 6.10 shows the non-dimensional film thickness variation at two different coolant flow rates. As expected higher film thickness is noted for the higher coolant flow. The wave features are almost similar in both the cases. Therefore it can be concluded that the interface characteristics are mainly influenced by the changes in core gas flow.

Roll wave velocity is calculated from two film thickness curves drawn from two

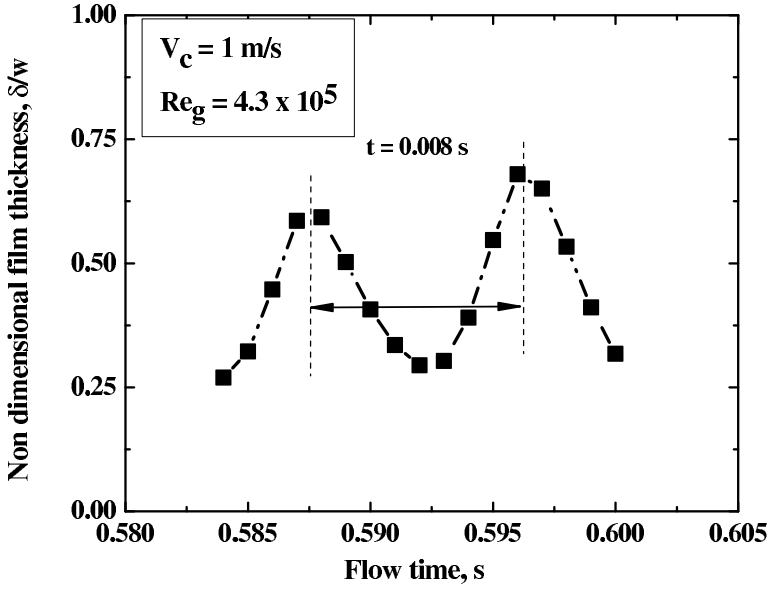

Figure 6.8: Film thickness variation with time at the monitoring surface

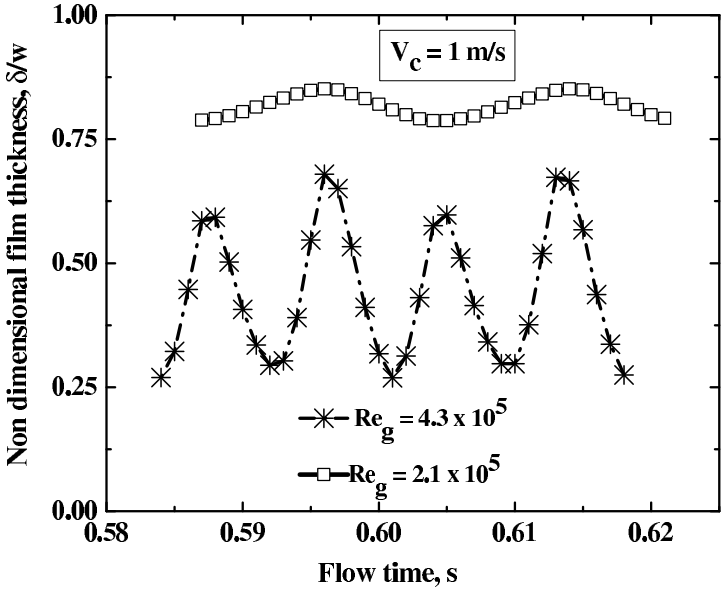

Figure 6.9: Film thickness variation with time at the monitoring surface for different core gas velocities

nearby monitoring surfaces. Two monitoring surfaces placed at 40 mm apart are used in the present study. It is observed that the two monitoring surfaces witness almost identical film thickness variations. The time gap for the roll wave to travel from one surface to the other can be used for calculating the wave velocity. Figure 6.11 shows non-dimensional film thickness curves at the two locations for the core gas Reynolds number $\mathrm{Re}_g = 4.3\times10^5$. The wave velocity is then calculated as $\mathrm{V}_{wave} = \Delta l/\Delta t$

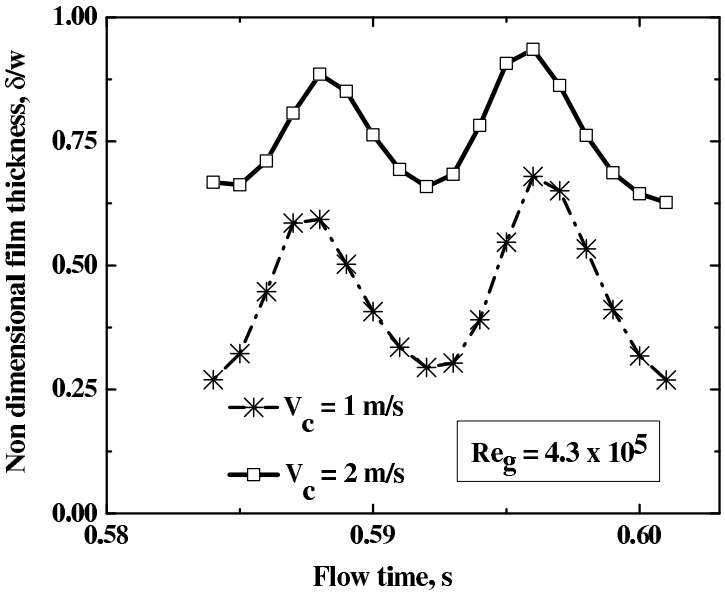

Figure 6.10: Film thickness variation with time at the monitoring surface

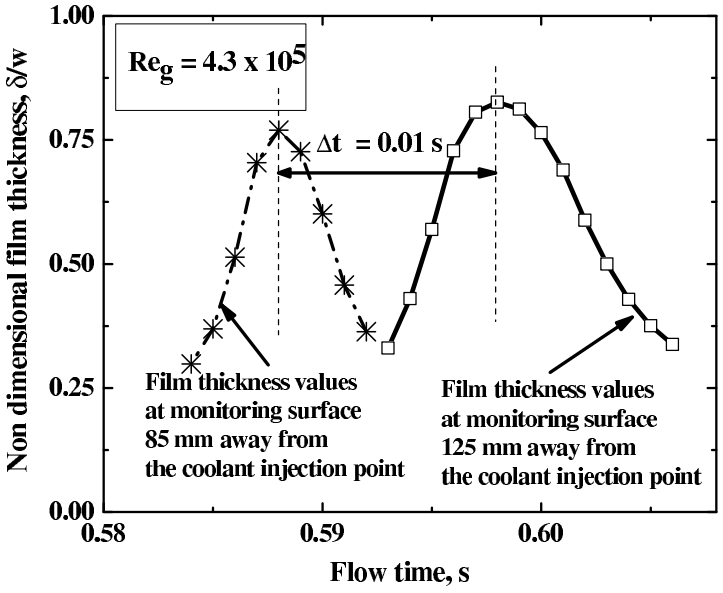

Figure 6.11: Roll wave velocity calculation method

= 40 mm/0.01 = 4 m/s. Table 6.7 illustrates the wave parameters obtained for the three cases investigated. It can be observed that the roll wave velocity is affected by both momentum flux ratio and the core gas Reynolds number. The wave velocity is higher than the average coolant velocity indicating momentum transfer by the highly energetic gas core to the liquid film. It can be noted that film thickness is a strong function of the momentum flux ratio.

Table 6.7: Roll wave parameters at different flow conditions at a distance of 75 mm from the coolant injection location

I	Re_g	V_c	Wave velocity, m/s	Wave frequency, Hz	Average film thickness, mm
0.05	4.3×10^5	1	4	125	0.24
0.21	4.3×10^5	2	10	125	0.44
0.226	2.1×10^5	1	8	55	0.47

6.4.10 Entrainment mechanism

The appearance of the disturbance wave are observed along the length of the tube to study the possible entrainment process. As the disturbance waves travel along the tube, a protruding part is formed at the wave front. This is due to the extra momentum imparted by the high velocity core gas flow. This protruding part grows by absorbing coolant from the wave crest. Finally this portion gets entrained into the gas core. This entrainment mechanism was first proposed by Han and Gabriel (2007). Figure 6.12 shows the protrusion of the wave and the entrainment process. Experiments using high-speed laser-induced fluorescence technique by Alekseenko et al. (2010) also showed shearing of the disturbance wave crest by the gas shear. The present simulation confirms this to be the predominant liquid entrainment mechanism of the liquid film cooling flows.

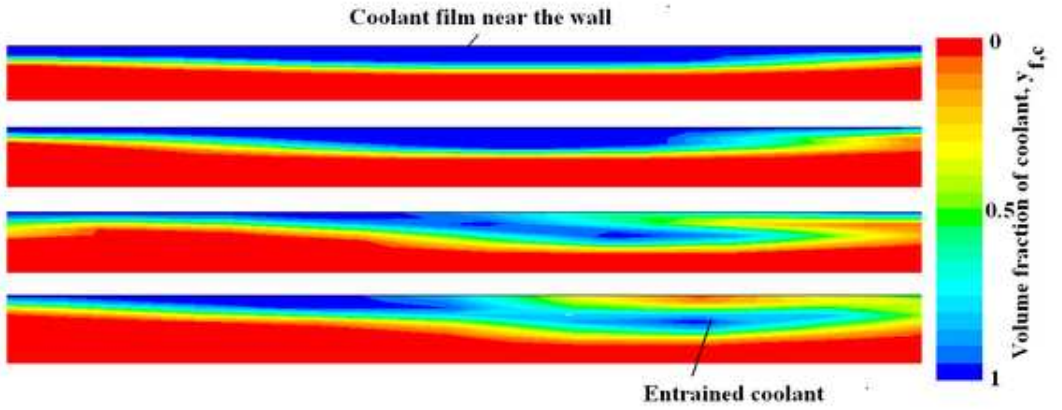

Figure 6.12: Wave evolution and liquid entrainment; case I = 0.94, V_c = 1 ms^{-1}

6.5 Conclusions

The liquid-gas interface characteristics of liquid film cooling flows inside a cylindrical section is investigated using a two-dimensional axis-symmetric transient computational model developed using the finite volume based CFD code ANSYS FLUENT 13.0.0. A transient renormalization group (RNG) k-ϵ model along with an enhanced wall treatment is employed for modelling turbulence. The two phase interface was constructed using the volume of fluid (VOF) geometric reconstruction scheme. Comparison of the model to the film cooling experimental data available in literature shows that the model is capable of predicting the main features of the flow fairly accurately. Important observations from the study are summarized below.

- For liquid film cooling flows, wave like disturbances started appearing at the liquid-gas interface at coolant flows above a critical value. For low coolant flow rates, the liquid-gas interface is undisturbed for a fairly short distance, of the order of diameter of the tube. This undisturbed distance increased with the increase in momentum flux ratio (I). Thereafter the interface showed wave like disturbances.

- The film thickness is mainly affected by the changes in momentum flux ratio (I). Higher film thickness is observed at higher momentum flux ratios.

- The coolant film thickness and the disturbance wave characteristics are not much affected by the changes in pipe diameter.

- Appreciable changes in wave properties are observed only up to certain values of momentum flux ratio. Therefore, based on the interface disturbance characteristics and the associated momentum flux ratios, three different regions of coolant flow can be defined; (i) a region where there is no disturbance wave, (ii) a region where appreciable changes in wave properties, and (iii) a region where wave properties are not affected much.

- Higher free stream turbulence in the core gas flow has resulted in lower liquid film length.

- It is observed that the disturbance wave frequency mainly depends on the core gas velocity,whereas the wave velocity is affected by both the coolant and core gas velocities.

- The flow field results showed that the disturbance waves continue to develop under the action of high momentum core gas flow, until the wave crest is sheared off. This seems to the predominant entrainment mechanism of liquid film cooling flows.

CHAPTER 7

CONCLUSIONS AND FUTURE WORK

The thesis has presented experimental, analytical and computational investigations that shed insight into the complex problem of film cooling in rocket combustion chambers. The combined knowledge is useful in understanding many important mechanisms which are previously only conjectured through educated guesses. In this chapter the final conclusions drawn from this study are summarised. Further work is also proposed, in order to improve and expand the knowledge of film cooling flows applicable to rocket combustion chambers.

7.1 Experimental Setup and Methods

Film cooling measurements were carried for different blowing ratios and temperature ratios between the coolant and hot air. The comprehensive experimental database obtained provides valuable detailed information on the performance of various film coolant injector configurations, viz., (i) straight and compound angle holes for the gaseous coolant and (ii) tangential and compound angle holes for the liquid coolant. The data can be used to estimate the performance of various injectors tested and to validate numerical models developed using CFD. The experimental facility and instrumentation developed as part of the current research would find further use in continuing the work towards testing of novel designs of coolant injectors.

7.2 Gaseous Injector Configurations

Straight and compound angle gaseous film configurations showed similar film cooling effectiveness at low momentum flux ratios. But at relatively high momentum flux

ratio, compound angle holes had significantly higher effectiveness than the straight injector. Higher film cooling effectiveness prevailed for the compound injection orifice of 30°-10° compared to other configurations including that of 45°-10° suggests that an optimum compound injection angle does exist maximizing the film cooling effectiveness.

Vorticity appeared to be a predominant flow feature that caused mixing and coolant spread in the circumferential direction. Symmetric counter rotating vortices were noticed with straight cylindrical coolant holes whereas compound angle coolant holes showed shrinking of one vortex leg. Secondary recirculation zones developed adjacent to the jet exit in regions close to the wall and the centre. These flow structures were also responsible for mixing of the coolant and mainstream. This produced higher heat transfer coefficients immediately downstream of injection and a local maximum value near the reverse flow regions. Relatively lower stream-wise momentum and higher asymmetric vorticity levels caused further mixing of coolant and mainstream at higher tangential angle of the coolant injector. It can be concluded that increasing the tangential angle does not necessarily provide improvement in the film cooling performance. For the straight injector, the advantage of more coolant availability at high momentum flux ratio is offset by the higher mixing of coolant with the mainstream due to high turbulence and vorticity levels. This results in an optimum blowing ratio for the straight injector.

Numerical simulations were also carried out for different geometrical configurations of the straight injector: three different D/d ratios of 60, 80 and 120, three expansion ratios of 1.1, 1.8 and 1.25 and three β of 6°, 7.2° and 8°. Higher film cooling effectiveness was observed for higher coolant diameters due to the presence of large amount of coolant near the hole. Strong vortices and high levels of turbulence further reduced the effectiveness for small coolant diameters. Higher expansion ratio of the duct caused increase in turbulence and heat transfer coefficient and results in lower effectiveness. Simulations showed variation of about 1% in spatially averaged effectiveness parameters for every 0.1 deg change in the included angle between two coolant holes compared with β = 8 deg case. It was also noted that increase in free-stream turbulence reduces the film cooling effectiveness and this effect is significant

at low blowing ratios.

In short, higher expansion ratios, lower coolant diameters and larger spacing between the coolant holes offer virtually no advantage in film cooling performance and should not be considered. It is also recommended to have higher blowing ratios when the free-stream turbulence is higher. However, gaseous coolant injection beyond a blowing ratio of 3.5 is not recommended due to drop in overall effectiveness across the test section.

7.3 Effect of Conjugate Wall

The conjugate heat transfer model predicted the film cooling effectiveness more accurately and showed significant difference with the adiabatic model. Higher effectiveness persisted far downstream of the injection point for all conjugate cases investigated compared with the adiabatic case. The wall conduction effects tend to reduce the effectiveness near the coolant injection point. The heat transfer through the solid wall from the hotter downstream to the cooler upstream region was noted. This resulted in a negative heat transfer condition near the coolant jet exit, i.e., heat transfer from the wall to the coolant. The analysis shows that highly conductive wall is not a proper choice for film cooling applications. The study reinforces the importance of considering conjugate wall in numerical modelling of film cooling.

7.4 Liquid Injector Configurations

In the case of liquid film injection, adding a compound angle produced no improvement in effectiveness compared to tangential injection. Longer liquid film length for tangential injector was seen compared to the compound angle injector. Compound angle injector failed to maintain the film uniformity away from the injection point compared to the tangential injector. It was also noted that higher injection pressure is required to keep the liquid film uniformly near the wall.

Experiments with compound angle injection showed significant variation in temperature around the circumference compared to tangential injection. The compound injection caused the jet to hit the wall surface and thereafter failed to maintain uniform distribution. Thus, tangential coolant injection is a good choice for liquid film cooling process wherein higher effectiveness and film uniformity is of concern.

7.5 1-D model for Liquid Film Cooling

A new one dimensional analytical model of liquid film cooling in rocket combustion chambers operating at subcritical conditions is proposed. Simplifying assumptions such as steady one-dimensional flow, adiabatic film-wall interface, non-reactive coolant and constant core gas temperature were made to develop this fundamental model. The model predictions compared favourably with the experimental data available in open literature. The results showed that the effects of radiation and coolant entrainment are significant. It was confirmed that the liquid film length decreases with increase in gas Reynolds number, coolant inlet temperature and free-stream turbulence. The effect of combustion chamber pressure was also investigated and found to be insignificant at higher pressures.

7.6 Disturbance Waves at Liquid-Gas Interface

The liquid-gas interface characteristics of liquid film cooling were investigated using a two-dimensional axi-symmetric computational model. It was observed that the disturbance waves started appearing at the liquid-gas interface at coolant flows above a critical value. The liquid-gas interface remained undisturbed for a fairly short distance of the order of diameter of the tube at low coolant flow rates. This undisturbed distance increased with the increase in momentum flux ratio (I). Thereafter the interface showed wave like disturbances. Appreciable changes in wave properties were observed only up to a certain value of momentum flux ratio. Therefore, based on the interface disturbance characteristics and the associated momentum flux ratios, three

different regions of coolant flow could be defined: (i) a region where there is no disturbance wave, (ii) a region where appreciable changes in wave properties and (iii) a region where wave properties are not affected much. It was observed that the disturbance wave frequency mainly depended on the core gas velocity, whereas the film thickness was a strong function of the momentum flux ratio. Higher free-stream turbulence in the core gas flow resulted in lower liquid film length.

The flow field results show that the disturbance waves continue to develop under the action of high momentum core gas flow, until the wave crest is sheared off. In the process, the wave drew the liquid from the liquid film to sustain its evolution. This seems to be the predominant entrainment mechanism of liquid film cooling flows. The results confirm the role of disturbance waves in the liquid entrainment process.

7.7 Conclusive Summary

The research objective envisaged in this work was to develop improved understanding of film cooling flows applicable to rocket combustion chambers. The measurement of film cooling performance data associated with various coolant injector configurations and operating conditions was one of the major aims of the research. This also provided quality experimental data for computational model development and validation. A closer understanding of the fluid dynamics and the heat transfer aspects of the problem was achieved through computational simulations. This has provided insights useful for design and development of advanced film cooling injector configurations. Simulation of liquid film cooling flows revealed important characteristics of disturbance waves present at the liquid-gas interface. The one-dimensional analytical model developed for the liquid film cooling process has the potential for use in the design of rocket combustion chamber cooling systems.

7.8 Future Work

Experimental investigations of various coolant injector configurations for liquid and gaseous coolants have been successfully carried out in the present study. Further in-

vestigations may be directed towards implementation of a subscale combustion chamber. Tests on a subscale combustion chamber at real engine conditions would be a reasonable extension of the current study.

Data obtained from this study suggest that an optimum compound angle configuration exists maximizing the film cooling effectiveness. Therefore, further studies and systematic exploration on geometric configuration would be beneficial.

The cooling mechanism of liquid film at high pressure would be different from that at low pressure. In the supercritical regime, the flow is similar to single-phase flow and all the thermal energy transferred from the hot gases is devoted to heating up the film. Many rocket engines are operating at supercritical conditions and therefore, research on film cooling under supercritical conditions would be beneficial.

Since the coolants used in this studies are nonreactive, better understanding of a reactive coolant injection requires further work.

REFERENCES

1. Abramson, A. E. (1952). *Investigation of internal film cooling of exhaust nozzle of a 1000-pound thrust liquid ammonia-liquid oxygen rocket*. Technical Report, NACA RME52C26.

2. Abu-Mulaweh, H. I., Chen, T. S., and Armaly, B. F. (2002). Turbulent mixed convection flow over a backward-facing step–the effect of the step heights. *International Journal of Heat and Fluid Flow*, *23*, 758–765.

3. Al-Hamadi, A. K., Jurban, B. A., and Theodoridis, G. (1998). Turbulence intensity effects on film cooling and heat transfer from compound angle holes with particular application to gas turbine blades. *Energy Convers. Mgmt*, *39*, 1449–57.

4. Alekseenko, S., Cherdantsev, A., Cherdantsev, M., Isaenkov, S., Kharlamov, S., and Markovich, D. (2010). Application of high-speed laser induced fluorescence technique for studying annular gas-liquid flows. In *15th Int Symp on Applications of Laser Techniques to Fluid Mechanics, Lisbon, Portugal*.

5. Andreussi, P., Asali, J. C., and Hanratty, T. J. (1985). Initiation of roll waves in gas-liquid flows. *AIChE J.*, *31*, 119–126.

6. Aravinth, S. (2000). Prediction of heat and mass transfer for fully developed turbulent fluid flow through tubes. *Int.J.Heat and Mass Transfer*, *43*, 1399–1408.

7. Arnold, R., Suslov, D., and Haidn, O. J. (2009a). Circumferential film cooling effectiveness in a LOX/H2 subscale combustion chamber. *Journal of Propulsion and Power*, *25*, 760–770.

8. Arnold, R., Suslov, D., and Haidn, O. J. (2009b). Film cooling of accelerated flow in a subscale combustion chamber. *Journal of Propulsion and Power*, *25*, 443–451.

9. Arnold, R., Suslov, D., and Haidn, O. J. (2010). Film cooling in a high-pressure subscale combustion chamber. *Journal of Propulsion and Power*, *26*, 428–438.

10. Baheri, S., Tabrizi, S. P. A., and Jubran, B. A. (2008). Film cooling effectiveness from trenched shaped and compound holes. *Heat and mass transfer*, *44*, 989–998.

11. Baldauf, S., Scheurlen, M., Schulz, A., and Wittig, S. (2002). Correlation of film-cooling effectiveness from thermographic measurements at engine-like conditions. *Journal of Turbomachinery*, *124*, 686–698.

12. Bartz, D. R. (1957). A simple equation for rapid estimation of rocket nozzle convective heat transfer coefficients. *Jet Propulsion -ARS Tournal*, *27*, 49–51.

13. Bell, C. M., Hamakawa, H., and Ligrani, P. M. (2000). Film cooling from shaped holes. *ASME Journal of Heat Transfer*, *122*, 224–232.

14. Benson, D. J. (2002). Volume of fluid interface reconstruction methods for multi-material problems. *Applied Mechanics Reviews*, *55*, 151–165.

15. Boden, R. H. (1951). Heat transfer in rocket motors and application of film and sweat cooling. *ASME Transactions*, *73*, 385–390.

16. Bogard, D. G., and Thole, K. A. (2006). Gas turbine film cooling. *Journal of Propulsion and power*, *22*, 249–270.

17. Brackbill, J. U., Kothe, D. B., and Zemach, C. (1992). A continuum method for modeling surface tension. journal of computational physics. *Journal of Computational Physics*, *100*, 335–54.

18. Brittingham, R. A., and Leylek, L. H. (2000). A detailed analysis of film cooling physics: Part iv-compound-angle injection with shaped holes. *ASME J. Turbomach.*, *122*, 133–145.

19. Campbell, J. G., Batha, D. R., Carey, M. D., Nagy, A. R., and Stechman, R. C. (1963). *Thrust chamber cooling techniques for spacecraft engines*. Marquardt Corp. Rept. 5981, Vol. II of Contract NAS7-103.

20. Chen, Y. T., Nie, J., Armaly, B. F., and Hsieh, H. T. (2006). Turbulent separated convection flow adjacent to backward-facing step – effects of step height. *International Journal of Heat and Mass Transfer*, *49*, 3670–3680.

21. Cho, H. H., Rhee, D. H., and Kim, B. G. (1999). Film cooling effectiveness and heat/mass transfer coefficient measurement around a conical-shaped hole with a compound angle injection. *ASME Paper No.99-GT-38*, .

22. Cook, R. T., and Quentmeyer, R. J. (1980). Advanced cooling techniques for high pressure hydrocarbon fueled rocket engines. In *AIAA Joint Propulsion Conference*. AIAA.

23. Coulbert, C. D. (1964). Selecting cooling techniques for liquid rockets for spacecraft. *Journal of Spacecraft and rockets*, *1*, 129–139.

24. Coy, E. B., Schumaker, S. A., and Lightfoot, M. A. (2009). Film cooling of liquid hydrocarbon engines for operationally-responsive space access. *JANNAF 5th Liquid Propulsion Subcommittee Meeting,Colorado Springs, CO*, .

25. Crooco, L. (1952). An approximate theory of porous, sweat, or film cooling with reactive fluids. *Journal American Rocket Society*, *22*, 331–338.

26. Dellimore, K. H., Cruz, C., Marshall, A. W., and Cadou, C. P. (2009). Influence of a stream-wise pressure gradient on film-cooling effectiveness. *Journal of Thermophysics and Heat transfer*, *23*, 120–128.

27. Dittmar, J., Schulz, A., and Wittig, S. (2003). Assessment of various film-cooling configurations including shaped and compound angle holes based on large-scale experiments. *ASME Journal of Turbomachinery*, *125*, 57–64.

28. Ekkad, S. V., Zapata, D., and Han, J. C. (1997). Heat transfer coefficients over a flat surface with air and co_2 injection through compound angle holes using transient liquid crystal image method. *ASME J. Turbomech*, *119*, 580–587.

29. Emmons, D. L. (1962). *Effects of selected gas stream parameters and coolant physical properties on film cooling a rocket motor*. Technical Report, Report No.TM-62-5, Purdue University.

30. Friend, W. L., and Metzner, A. B. (1958). Turbulent heat transfer inside tubes and the analogy among heat, mass and momentum transfer. *AIChE J*, *4*, 393–402.

31. Gater, R. A., LŠecuyer, M. R., and Warner, C. F. (1965). *Liquid-film cooling Its physical nature and theoretical analysis*. Technical Report, TM-65-6, Jet Propulsion Center, Purdue University, Lafayette.

32. Gau, C., Yihm, K. A., and Changm, S. S. (1991). Swirling flow effect on film cooling performance downstream of a sudden expansion. *J Thermophysics*, *5*, 89–95.

33. George, W. K. (2007). Is there a universal log law for turbulent wall-bounded flows? *Phil.Trans.R.Soc.*, *365*, 789–806.

34. Ghorab, M. G. (2011). Adiabatic and conjugate cooling effectiveness analysis of a new hybrid scheme. *International Journal of Thermal Sciences*, *50*, 965–983.

35. Goldstein, R. J., and Haji-Sheikh, A. (1967). *Prediction of Film Cooling Effectiveness*. Japan Society of Mechanical Engineers Paper 225.

36. Goldstein, R. J., Rask, R. B., and Eckert, E. R. G. (1966). Film cooling with helium injection into an incompressible air flow. *Int. J. Heat and Mass Transfer*, *9*, 1341–1350.

37. Graham, A. K. (1958). *Film Cooling of Rocket Motors Part I An Experimental and Theoretical Investigation of Film Cooling of Rocket Motors*. Ph.d. thesis Jet Propulsion Center, Purdue University, Lafayette.

38. Grisson, W. M. (1991). *Liquid Film cooling in Rocket Engines*. Technical Report AEDC–TR–91–1, DTIC.

39. Han, H., and Gabriel, K. (2007). A numerical study of entrainment mechanism in axisymmetric annular gas-liquid flow. *ASME Journal of Fluids Engineering*, *129*, 293–301.

40. Hersh, M. (1961). Experimental method of measuring intensity of turbulence in a rocket chamber. *ARS Journal*, *31*, 39–45.

41. Heufer, K. A., and Olivier, H. (2008). Experimental and numerical study of cooling gas injection in laminar supersonic flow. *AIAA Journal*, *11*, 2741–2751.

42. Hung, M., Ding, P., and Chen, P. (2009). Effects of injection angle orientation on concave and convex surfaces film cooling. *Experimental Thermal and Fluid Science*, *33*, 292–305.

43. Hutchines, N., and Marusic, I. (2007). Evidence of very long meandering features in the logarithmic region of turbulent boundary layers. *J.Fluid.Mech*, *579*, 1–28.

44. Huzel, D. K., and Hwang, D. H. (1992). *Modern Engineering for Design of Liquid Rocket Engines*. American Institute of Aeronautics and Astronautics.

45. Hyams, D. G., and Leylek, J. H. (2000). A detailed analysis of film cooling physics: Part iii–streamwise injection with shaped holes. *ASME J. Turbomach.*, *122*, 122–132.

46. Jiang, P. X., Yu, L., Sun, J., and Wang, J. (2004). Experimental and numerical investigation of convection heat transfer in transpiration cooling. *Applied thermal engineering*, *24*, 1271–1289.

47. Jubran, B. A., Al-Hamadi, A. K., and Theodoridis, G. (1997). Film cooling and heat transfer with air injection through two sets of compound angle holes. *Heat and mass transfer*, *33*, 93–100.

48. Kaji, R., and Azzopardi, B. J. (2010). The effect of pipe diameter on the structure of gas/liquid flow in vertical pipes. *International Journal of Multiphase Flow*, *36*, 303–313.

49. Kays, W. M., and Crawford, M. E. (2005). *Convective heat and mass transfer, Second edition*. (4th ed.). McGraw-Hill Book company.

50. Keener, D., Lenertz, J., Bowersox, R., and Bowman, J. (1995). Transpiration cooling effects on nozzle heat transfer and performance. *J. Spacecraft Rockets*, *32*, 981–985.

51. Kesselring, R. C., Knight, R. M., McFarland, B. L., and Gurnitz, R. N. (1972). *Boundary cooled rocket engines for space storable proplellants*. Technical Report, Rocketdyne Report No. R-8766.

52. Kim, S. (1991). Numerical study of high area ratio H2/O2 rocket nozzles. In *24th AIAA/SAE/ASME/ASEE, Joint Propulsion Conference*. AIAA.

53. Kim, S. E., Choudhury, D., and Patel, B. (1997). Computations of complex turbulent flows using the commercial code fluent. In *ICASE/LaRC/AFOSR Symposium on Modeling Complex Turbulent Flows, Hampton, Virginia, U.S.A*.

54. Kinney, G. R., Abramson, A., and Sloop, J. L. (1952). *Internal film cooling experiments with 2 and 4 inch smooth surface tubes and gas temperatures to 2000- F in 2 and 4 inch diameter horizontal tubes*. Technical Report, NACA report 1087.

55. Kirchberger, C., Schlieben, G., Hupfer, A., Kau, H., Martin, P., and Soller, S. (2009). Investigation on film cooling in a kerosene/gox combustion chamber. In *45th AIAA/ASME/SAE/ASEE Joint Propulsion Conference and Exhibit*. AIAA.

56. Kline, S. J., and McClintock, F. A. (1953). Describing uncertainties in single-sample experiments. *J. Mech. Eng.*, *75*, 3–8.

57. Knuth, E. L. (1954). *The mechanism of film cooling*. Ph.D. thesis California Institute of Technology.

58. Koc, I., Parmaksizoglu, C., and Cakan, C. M. (2006). Numerical investigation of film cooling effectiveness on the curved surface. *Energy Conversion and Management*, *47*, 1231–46.

59. Kuo, S. L., Zhangt, N. L., and Yangt, W. J. (1996). Role of mainstream flow velocity in film cooling in a duct. *J Thermophysics*, *10*, 382–384.

60. Kutateladze, S. S., and Leontev, A. I. (1963). The heat curtain in the turbulent boundary layer of a gas. *Thermal Physics of High Temperature*, *1*, 281–290.

61. Lamb, H. (1982). *Hydrodynamics*. Cambridge University Press.

62. Lan, H., Armaly, B. F., and Drallmeier, J. A. (2009). Three-dimensional simulation of turbulent forced convection in a duct with backward-facing step. *International Journal of Heat and Mass Transfer*, *52*, 1690–1700.

63. Launder, B. E., and Spalding, D. B. (1972). *Lectures in mathematical models of turbulence.*. Academic Press, London.

64. Launder, B. E., and Spalding, D. B. (1974). The numerical computation of turbulent flows. *Computer Methods in Applied Mechanics and Engineering*, *3*, 269–289.

65. Leckner, B. (1972). Spectral and total emissivity of water vapor and carbondioxide. *Combustion and Flame*, *19*, 33–48.

66. Lee, H. W., Park, J. J., and Lee, J. S. (2002). Film cooling with helium injection into an incompressible air flow. *Int. J. Heat and Mass Transfer*, *45*, 142–156.

67. Li, X., Meng, J., and Guo, Z. (2009). Turbulent flow and heat transfer in discrete double inclined ribs tube. *Int. J. Heat and Mass Transfer*, *52*, 962–970.

68. Li, X., and Wang, T. (2008). Computational analysis of surface curvature effect on mist film-cooling performance. *Journal of Heat Transfer*, *130*, 121901–10.

69. Ligrani, P. M., Wigle, J., Ciriello, S., and Jackson, S. W. (1994). Film cooling from holes with compound angle orientations: Part 1. results downstream of two staggered rows of holes with 3d span wise spacing. *ASME J. Heat transfer*, *116*, 341–352.

70. Lucas, J. G., and Golladay, R. L. (1963). *An experimental investigation of gaseous film cooling of a rocket motor*. NASA TN 0-1988.

71. Maiteh, B. Y., and Jubran, B. A. (1999). Effect of compound angle injection on flat surface film cooling with large stream wise injection angle. *Int. J. Heat and Fluid flow*, *20*, 158–165.

72. Marek, C. J., and Tacina, R. R. (1975). *Effects of Free-Stream Turbulence on Film Cooling*. NASA TN D-7985.

73. Martelli, E., Nasuti, F., and Onofri, M. (2009). Numerical analysis of film cooling in advanced rocket nozzles. *AIAA Journal*, *47*, 2558–2566.

74. McGovern, K. T., and Leylek, J. H. (2000). A detailed analysis of film cooling physics: Part ii–compound-angle injection with cylindrical holes. *ASME J. Turbomach.*, *122*, 113–121.

75. McGrath, E. L., and Leylek, J. H. (1998). Physics of hot flow ingestion in film cooling. *ASME Paper No.98-GT-191*, .

76. Mckeon, B. J., Zagarola, M. V., and J.Smits, A. (2005). A new friction factor relationship for fully developed flow. *J.Fluid.Mech*, *538*, 429–443.

77. Mehrotra, A. K., Karan, K., and Behie, L. A. (1995). Estimate gas emissivities for equipment and process design. *Chemical Engineering Progress*, *September*, 70–77.

78. Meinert, J., and Huhn, J. (2001). Turbulent boundary layers with foreign gas transpiration. *Journal of Spacecraft and rockets*, *38*, 191–198.

79. Michel, B., Gajan, P., Strzelecki, A., Savary, N., Kourta, A., and Boisson, H. (2009). Full coverage film cooling using compound angle. *C. R. Mecanique*, *337*, 562–572.

80. Miller, R. P., and Coy, E. B. (2011). Studies in optimizing the film flow rate for liquid film cooling. In *47th AIAA Joint Propulsion Conference, San Diego,*. AIAA.

81. Modest, M. F. (1990). *Radiative heat transfer*. (2nd ed.). Academic Press.

82. Moffat, R. J. (1985). Describing the uncertainties in experimental results. *Exp Therm Fluid Sci*, *1*, 3–17.

83. Monty, J. P., Hutchins, N., Ng, H. C. H., Marusic, I., and Chong, M. S. (2009). A comparison of turbulant pipe, channel and boundary layers. *J.Fluid.Mech*, *632*, 431–442.

84. Morrell, G. (1951). *Investigation of internal film cooling of a 1000-pound thrust liquid ammonia liquid oxygen rocket*. Technical Report, NACA RME51E04.

85. Nasir, H., Srinath, S. V., and Acharya, S. (2001). Effect of compound angle injection on flat surface film cooling with large stream wise injection angle. *Experimental Thermal and Fluid Science*, *25*, 23–29.

86. Norton, P. (2005). *Appendices, in: F.Kreith, D.Y.Goswami (Eds.), The CRC Handbook of Mechanical Engineering*. CRC Press.

87. Nuefeld, P. D., Janzen, A. R., and Aziz, R. A. (1972). Empirical equations to calculate 16 of the transport collision integrals for the lennard-jones (12-6) potential. *J.Chem.Phys.*, *57*, 1100–11.

88. O'Connor, J. P., and Haji-Sheikhf, A. (1992). Numerical study of film cooling in supersonic flow. *AIAA Journal*, *30*, 2426–2433.

89. Pedersen, D. R., Eckert, E., and Goldstein, R. (1977). Film cooling with large density differences between the mainstream and the secondary fluid measured by the heat-mass transfer analogy. *Journal of Heat Transfer*, *99*, 620–627.

90. Pletcher, R. H. (1988). Progress in turbulent forced convection. *Trans of ASME-Journal of Heat Transfer*, *110*, 1129–1144.

91. Rannie, W. D. (1956). Heat transfer in turbulent shear flow. *Journal of the Aeronautical Sciences*, *25*, 485–489.

92. Reid, R. C., Prausnitiz, J. M., and Sherwood, T. K. (1977). *The properties of gases and mixtures*. (3rd ed.). McGraw-Hill Book Company, New York.

93. Reynolds, O. (1876). On the resistance encountered by vortex rings and the relation between the vortex rings and the streamlines of a disc. *Nature*, *14*, 477–479.

94. Robert, W. L. (1990). *Effect of pipe diameter on horizontal annular two phase flows*. Ph.D. thesis University of Illinois at Urbana-Champaign, Urbana.

95. Sawant, P., Ishii, M., and Mori, M. (2008). Droplet entrainment correlation in vertical upward co-current annular two-phase flow. *Nuclear Engineering and design*, *238*, 1342–1352.

96. Schmidt, D. L., Sen, B., and Bogard, D. G. (1996). Film cooling with compound angle holes: Adiabatic effectiveness. *ASME J. Turbomach.*, *118*, 807–813.

97. Sellers, J. P. (1958). *Experimental and Theoretical Study of the Application of FIm-Cooling to a Cylindrical Rocket Thrust Chamber*. Ph.d. thesis Jet Propulsion Center, Purdue University, Lafayette.

98. Sen, B., Schmidt, D. L., and Bogard, B. G. (1996). Film cooling with compound angle holes:heat transfer. *ASME J. Turbomech*, *118*, 806–807.

99. Shembharkar, T. R., and Pai, B. R. (1986). Prediction of film cooling with a liquid coolant. *Int.J.Heat and Mass Transfer*, *29*, 899–908.

100. Shih, T. H., Liou, W. W., Shabbir, A., Yang, Z., and Zhu, J. (1995). A new k-ϵ eddy-viscosity model for high reynolds number turbulent flows-model development and validation. *Computers and Fluids*, *24*, 227–238.

101. Shine, S. R., Kumar, S. S., and Suresh, B. N. (2012a). Influence of coolant injector configuration on film cooling effectiveness for gaseous and liquid film coolants. *Heat and Mass Transfer*, *48*, 849–861.

102. Shine, S. R., Kumar, S. S., and Suresh, B. N. (2012b). Internal wall-jet film cooling with straight cylindrical holes. *AIAA Journal of Thermophysics and Heat Transfer*, *26*, 439–449.

103. Shine, S. R., Kumar, S. S., and Suresh, B. N. (2012c). A new generalised model for liquid film cooling in rocket combustion chambers. *International Journal of Heat and Mass Transfer*, *55*, 5065–5075.

104. Shine, S. R., Kumar, S. S., and Suresh, B. N. (2013a). Internal wall-jet film cooling with compound angle cylindrical holes. *Energy Conversion and Management*, *68*, 54–62.

105. Shine, S. R., Kumar, S. S., and Suresh, B. N. (2013b). Properties of disturbance waves in liquid film cooling flows. *Propulsion and Power Research*, .

106. Silieti, M., Kassab, A. J., and Divo, E. (2009). Film cooling effectiveness: Comparison of adiabatic and conjugate heat transfer CFD models. *International Journal of Thermal Sciences*, *48*, 2237–2248.

107. Simon, F. (1986). *Jet Model for Slot Film Cooling with Effect of Free-Stream and Coolant Turbulence*. NASA TP-2655.

108. Sinha, A., Bogard, D., and Crawford, M. (1991). Film cooling effectiveness downstream of a single row of holes with variable density ratio. *Journal of Turbomachinery*, *113*, 442–449.

109. Sivrioglu, M. (1991). An analysis of the effects of pressure gradient and streamline curvature on film cooling effectiveness. *Heat and mass transfer*, *26*, 103–107.

110. Stechman, R. C., Oberstone, J., and Howell, J. C. (1969). Design criteria for film cooling for small liquid-propellant rocket engines. *Journal of Spacecraft and rockets*, *6*, 97–102.

111. Stiel, L. I., and Thodos, G. (1964). The thermal conductivity of nonpolar substances in the dense gaseous and liquid regions. *AIChE J.*, *10*, 26–30.

112. Talmor, E. (1966). Turbulence determination and blockage correction for immersed cylinder heat transfer at high reynolds numbers. *A.I.Ch.E. Journal*, *12*, 1092–1097.

113. Taslim, M. E., and Khanicheh, A. (2005). Film effectiveness downstream of a row of compound angle film holes. *ASME Journal of Heat Transfer*, *127*, 434–444.

114. Taylor, N. H., Hewitt, G. F., and Lacey, P. (1963). The motion and frequency of large disturbance waves in annular two-phase flow of air-water mixtures. *Chemical Engineering Science*, *18*, 537–552.

115. Turcotte, D. L. (1960). A sublayer theory for fluid injection into the incompressible turbulent boundary layer. *Journal of the Aeronautical Sciences*, *27*, 675–678.

116. Vilja, J. O., Briley, G. L., and Murphy, T. H. (1993). J-2s rocket engine. In *29th AIAA/SAE/ASME/ASEE Joint Propulsion Conference and Exhibit*. AIAA.

117. Viskanta, R. (1998). Overview of convection and radiation in high temperature gas flows. *International Journal of Engineering Science*, *36*, 1677–1699.

118. Volkman, J. C., Tuegel, L. M., and McLeod, J. M. (1990). Gas side heat flux and film coolant investigation for advanced lox/hydrocarbon thrust chambers. In *AIAA/SAE/ASME/ASEE 26 th Joint Propulsion Conference*. AIAA.

119. Walters, D. K., and Leylek, J. H. (2000). A detailed analysis of film-cooling physics: Part i–streamwise injection with cylindrical holes. *ASME J. Turbomach.*, *122*, 102–112.

120. Wang, T. S., and Luong, V. (1994). Hot-gas-side and coolant-side heat transfer in liquid rocket engine combustors. *Journal of Thermophysics and Heat Transfer*, *8*, 524–530.

121. Warner, C. F., and Emmons, D. L. (1964). Effects of selected gas stream parameters and coolant properties on liquid film cooling. *Trans ASME Journal of Heat Transfer*, *1*, 271–278.

122. Warren, D., and Langer, C. (1989). History in the making-the mighty f-1 rocket engine. In *25th AIAA/ASME/SAE/ASEE Joint Propulsion Conference*. AIAA.

123. Waye, S. K., and Bogard, D. G. (2007). High-resolution film cooling effectiveness comparison of axial and compound angle holes on the suction side of a turbine vane. *ASME Journal of Turbomachinery*, *129*, 202–211.

124. Weiguo, A., Murray, N., Fletcher, T. H., Harding, S., and Bons, J. P. (2012). Effect of hole spacing on deposition of fine coal flyash near film cooling holes. *ASME Journal of Turbomachinery*, *134*, 041021–1–9.

125. Welsh, J. W. E. (1961). *Review of results of an early rocket engine film-cooling investigation at the Jet Propulsion laboratory.*. Technical Report TM-32-58, Jet propusion center, California Institute of Technology.

126. Wieghardt, K. (1944). *On the Blowing of Warm Air for De-Icing Devices*. FB.1900, Reports and Translations No.315.

127. Wilke, C. R. (1950). A viscocity equation for gas mixtures. *Journal Chem. Phys.*, *18*, 517–519.

128. Wosnik, M., Castillo, L., and George, W. (2000). A theory for turbulent pipe and channel flows. *J.Fluid.Mech*, *421*, 115–145.

129. Yakhot, V., and Orszag, S. A. (1986). Renormalization group analysis of turbulence: I. basic theory. *Journal of Scientific Computing*, *1*, 1–51.

130. Yang, C. S., Kung, T. C., and Gau, C. (2007). Heat transfer process under a film-cooled surface with presence of weak swirling flow in the mainstream. *Experimental Thermal and Fluid Science*, *32*, 632–640.

131. Yimer, I., Campbell, I., and Jiang, L. Y. (2002). Estimation of the turbulent schmidt number from experimental profiles of axial velocity and concentration for high-reynolds-number jet flows. *Canadian Aeronautics and Space Journal*, *48*, 195–200.

132. Youngs, D. L. (1982). *Time dependent multi-material flow with large fluid distortion, Numerical Methods for Fluid Dynamics*. K. W. Morton and M. J. Baines(editors), Academic Press, U.S.A.

133. Yu, Y. C., Schuff, R. Z., and Anderson, W. E. (2004). Liquid film cooling using swirl in rocket combustors. In *0thAIAA/ASME/SAE/ASEE Joint Propulsion Conference and Exhibit*. AIAA.

134. Zhang, H. W., Tao, W. Q., He, Y. L., and Zhang, W. (2006). Numerical study of liquid film cooling in a rocket combustion chamber. *Int.J.Heat and Mass Transfer*, *49*, 349–358.

APPENDIX A

PROPERTY CALCULATIONS

A.1 Properties of Air

The properties of air are calculated as a function of temperature (K).

$$\begin{aligned} c_p(Jkg^{-1}K^{-1}) &= 1.12295 \times 10^{-10}T^4 - 5.35621 \times 10^{-7}T^3 \\ &\quad + 8.27169 \times 10^{-4}T^2 - 0.295423T + 1032.1 \end{aligned} \tag{A.1}$$

$$\begin{aligned} \mu(kgm^{-1}s^{-1}) &= 5.41836 \times 10^{-15}T^3 - 2.52496 \times 10^{-11}T^2 \\ &\quad + 5.87333 \times 10^{-8}T - 2.80339 \times 10^{-6} \end{aligned} \tag{A.2}$$

$$\begin{aligned} k(Wm^{-1}K^{-1}) &= 6.5667 \times 10^{-12}T^3 - 3.38667 \times 10^{-8}T^2 \\ &\quad + 9.42622 \times 10^{-5}T - 7.50556 \times 10^{-4} \end{aligned} \tag{A.3}$$

A.2 Properties of Nitrogen

The specific heat is calculated from the following polynomial.

$$\begin{aligned} c_p(Jkg^{-1}K^{-1}) &= 3.42738 \times 10^{-11}T^4 - 4.61538 \times 10^{-7}T^3 \\ &\quad + 9.52776 \times 10^{-4}T^2 - 0.464T + 1106.325 \end{aligned} \tag{A.4}$$

A.3 Diffusion Coefficient Calculations

The diffusion coeficient is calculated using Chapman Enskog equation A.5.

$$D_{AB} = \frac{1.858 \times 10^{-3} \times T^{\frac{3}{2}} \times \left[\frac{\mathcal{M}_A + \mathcal{M}_B}{\mathcal{M}_A \mathcal{M}_B}\right]^{\frac{1}{2}}}{P\sigma_{AB}^2 \Omega_S} \tag{A.5}$$

where, D_{AB} = diffusion coefficient, cm^2 from species A to B.

T = temperature,K

P = pressure, atm

σ_{AB} is the characteristic length in A°.

σ_{AB} is given by $\sigma_{AB} = \frac{\sigma_A + \sigma_B}{2}$.

σ_A and σ_B is taken from Appendix C of Reid et al. (1977).

Ω_S is the collision integral and is calculated using the relation of Nuefeld et al. (1972).

$$\Omega_S = \frac{A}{T^{*B}} + \frac{C}{expDT^*} + \frac{E}{expFT^*} + \frac{G}{expHT^*} \tag{A.6}$$

A, B, C, D, E, F, G and H are empirical constants.

The values are A = 1.06036; B = 0.15610; C = 0.19300; D = 0.47635;

E = 1.03587; F = 1.52996; G = 1.76474 and H = 3.89411.

T* is calculated as follows.

$$T^* = T \times \frac{k}{\epsilon}; T = (T_A + T_B)/2. \tag{A.7}$$

$\frac{k}{\epsilon}$ values are available in Appendix C of Reid et al. (1977).

APPENDIX B

CALCULATIONS BASED ON ANALYTICAL MODEL

B.1 Liquid Film Length Calculations

Morrell (1951) had conducted internal film cooling experiments in a 4448 N thrust liquid ammonia-liquid oxygen rocket engine at chamber pressures from about 15.2 to 18.6 bar absolute and oxidant- fuel ratios from 0.8 to 2.0. Three coolants were studied: water, 2 to 7.5% of the total flow; ethyl alcohol, 5 to 15%; and anhydrous liquid ammonia, 3 to 21%. A complete set of calculations based on one set of Morrell's (1951) experimental data for the water coolant is given below.

$$
\begin{aligned}
\text{Coolant inlet temperature, } T_{c,in} &= 300 \text{ K} \\
\text{Freestream gas temperature, } T_g &= 2935 \text{ K} \\
\text{Coolant saturation temperature, } T_{c,sat} &= 480 \text{ K} \\
\text{Mean temperature, } T_m &= (T_{c,sat} + T_g)/2 \\
&= (480 + 2935)/2 \\
&= 2935 \text{ K} \\
\text{Oxident-Fuel ratio, } OF &= 1.72
\end{aligned}
$$

Molecular weight of combustion products are calculated based on the combustion reaction shown below

$x_1\ NH_3 + x_2\ O_2 \rightarrow 1.5\ x_1\ H_2O + 0.5\ x_1\ N_2 + (x_2\text{-}0.75\ x_1)O_2$

$$
\begin{aligned}
\text{Molecular wt of free stream gas, } \mathcal{M}_g &= 544 + (1 + OF)\,/\,(40 + 17 \times OF) \\
&= 544 + (1 + 1.72)\,/\,(40 + 17 \times 1.72) \\
&= 21.37 \\
\text{Chamber Pressure, } P &= 17.72 \text{ bar} \\
\text{Density of freestream, } \rho_g &= P \times \mathcal{M}/\bar{R} \times T_g \\
&= 17.72 \times 10^5 \times 21.37/8314 \times 2935 \\
&= 1.551 \text{ kg m}^{-3}
\end{aligned}
$$

Diameter of the test section, $D = 0.1016$ m

Flow area of gases, $A_g = (\pi/4)\, D^2$

$= (\pi/4)\, 0.1016^2$

$= 0.0081$ m^2

Main gas flow rate, $m_g = 1.778$ kg s^{-1}

Velocity of gases, $V_g = m_g/\rho_g \times A_g$

$= 1.778/0.0081 \times 1.551$

$= 141.33$ m s^{-1}

Density of coolant, $\rho_c = 857$ kg m^{-3}

Coolant flow rate, $m_c = 0.041$kg s^{-1}

Flow area of coolant, $A_c = 60 \times 0.00031$ in^2

Velocity of coolant, $V_c = m_c/\rho_c \times A_c$

$= 0.041/60 \times 0.00031 \times 0.0254^2 \times 857$

$= 4$ m s^{-1}

Mass flux of main gas, $G_g = m_g/A_g$

$= 1.778/0.0081$

$= 215.32$ kg m^{-2} s^{-1}

Velocity corrected mass flux, $G_{g,cor} = G_g \times (V_g - V_c)\,/V_g$

$= 215.32 \times (141.33 - 4)\,/141.33$

$= 213.16$ kg m^{-2} s^{-1}

Viscocity of gases, $\mu_g = 8.71 \times 10^{-5}$ kg m^{-1} s^{-1} [Section $B.2.1$]

Gas Reynolds number, $Re_g = G_{g,cor} \times D/\mu_g$

$= 213.16 \times 0.1016/8.71 \times 10^{-5}$

$= 248523$

Implicit Darcy friction factor,λ relationship

$$1/\lambda = 1.930 \times log_{10}\left(Re\sqrt{\lambda}\right) - 0.537$$

$$1/\lambda = 1.930 \times log_{10}\left(248523\sqrt{\lambda}\right) - 0.537$$

Solving implicitily, $\lambda = 0.015$

$$
\begin{aligned}
\text{fanny's friction factor, } f &= \lambda/4 \\
&= 0.015/4 \\
&= 0.0038 \\
\text{Prandtl number of gases, } Pr_g &= 0.7676 \text{ [Section } B.2.2] \\
\text{Stanton number for} & \\
\text{dry wall conditions, } St_o &= \frac{f/2}{1.20 + 11.8 \times (Pr - 1) \times Pr^{-1/3} \times \sqrt{\frac{f}{2}}} \\
&= \frac{0.0038/2}{1.20 + 11.8 \times (0.767 - 1) \times 0.767^{-1/3} \times \sqrt{\frac{0.0038}{2}}} \\
&= 0.00177 \\
\text{Free stream turbulence factor, } e_t &= 0.1 \\
\text{Specific heat of main gases, } c_g &= 2342.8 \text{ J kg}^{-1} \text{ K}^{-1} \text{ [Section } B.2.3] \\
\text{Heat transfer coefficient for} & \\
\text{dry wall conditions, } h_o &= St_o \times G_{g,cor} \times cp_g \times (1 + 4e_t) \\
&= 0.00177 \times 213.16 \times 2342.8 \times (1 + 4 \times 0.1) \\
&= 1239.064 \text{ W.m}^{-2}\text{.K}^{-1} \\
\text{Specific heat of coolant, } c_c &= 4530 \text{ J kg}^{-1} \text{ K}^{-1} \\
\text{Latent heat of coolant, } h_{fg_c} &= 1910000 \text{ J kg}^{-1} \\
h^*_{fg} &= h_{fg} + cp_c \left(T_{c,i} - T_{c,sat}\right) \\
&= 1910000 + 4530 \left(480 - 300\right) \\
&= 2725400 \text{ J kg}^{-1} \\
\text{Molecular weight of coolant, } \mathcal{M}_c &= 18 \\
\text{Correction factor for transpiration, } K_M &= \left(\mathcal{M}_g/\mathcal{M}_c\right)^{0.6} \\
&= \left(21.37/18\right)^{0.6} \\
&= 1.1085 \\
\text{Emissivity of gases, } \epsilon &= 0.211 \text{ [Section } B.3] \\
\text{Heat flux due to radiation, } q_{rad} &= \epsilon \times \sigma \times \left(T_g^4 - T_{c,sat}^4\right) \\
&= 0.211 \times \sigma \times \left(2935^4 - 480^4\right) \\
&= 886373 \text{ W m}^{-2}
\end{aligned}
$$

Equations for calculating transpiration corrected h

$$
\begin{aligned}
h/h_o &= St/St_o \\
&= \frac{ln\left[1+\left(\frac{F}{St}\right)\left(\frac{\mathcal{M}_g}{\mathcal{M}_c}\right)^{0.6}\right]}{\left(\frac{F}{St}\right)\left(\frac{\mathcal{M}_g}{\mathcal{M}_c}\right)^{0.6}} \\
\text{where,} F/St &= \frac{cp_g}{hfg^*}\left[(T_g - T_{c,sat}) + \frac{q_{rad}}{h}\right]
\end{aligned}
$$

h can be implicitly determined from the above equations

$$
\begin{aligned}
&\text{Transpiration corrected} \\
&\text{convection heat transfer coefficient, } h = 495.91 \text{ W m}^{-2} \text{ K}^{-1} \\
&\text{Heat flux by convection, } q_{conv} = h \times (T_g - T_{c,sat}) \\
&\qquad = 495.91 \times (2935 - 480) \\
&\qquad = 1217449 \text{ W m}^{-2} \\
&\text{Coolant evaporation rate, } \dot{m}_{film} = \frac{(q_{rad} + q_{conv})}{h^*_{fg}} \\
&\qquad = (886376 + 1217449)/2725400 \\
&\qquad = 0.772 \text{ kg m}^{-2} \text{ s}^{-1} \\
&\text{Factor of entrainment, } E = 26.35\% \text{ [Section } B.4] \\
&\text{Mass lost due to entrainment} = E \times m_c/100 \\
&\qquad = 26.35 \times 0.041/100 \\
&\qquad = 0.011 \text{ kg s}^{-1} \\
&\text{Mass lost at injection} = 0.013 \text{ kg s}^{-1} \text{(Data from experiment)} \\
&\text{Coolant flow available for} \\
&\text{film cooling/circumference, } \Gamma_c = \frac{(m_c - \text{Entrainment loss - Mass lost at injection})}{\pi \times D} \\
&\qquad = (0.041 - 0.011 - 0.013)/\pi \times 0.1016 \\
&\qquad = 0.0526 \text{ kg m}^{-1} \text{ s}^{-1} \\
&\text{Liquid film cooled length, } L = \Gamma_c/\dot{m}_{film} \\
&\qquad = 0.0256/0.772 \\
&\qquad = 0.068 \text{ m}
\end{aligned}
$$

B.2 Core Gas Property Calculations

B.2.1 Calculation of viscosity

Calculation for component gases viscosities are done by using Chapman-Enskog correlation.

Calculation for H_2O

$$\begin{aligned}
\text{Molecular weight of } H_2O,\ \mathcal{M}_{H_2O} &= 18.015 \\
T^* &= \left(\frac{\text{Boltzman constant}}{\text{Charectiristic energy}}\right)_{H_2O} \times T \\
&= \left(\frac{1}{809.1}\right) \times 2935 \\
&= 3.63 \\
\text{Collision integral, } \Omega_v &= \frac{A}{T^{*B}} + \frac{C}{e^{DT^*}} + \frac{E}{e^{FT^*}} \\
&= \frac{1.16145}{T^{*0.14874}} + \frac{0.52487}{e^{0.7732\times T^*}} + \frac{2.16178}{e^{2.43787\times T^*}} \\
&= 0.99 \\
\text{Viscosity, } \mu_{H_2O} &= \frac{26.69 \times \sqrt{\mathcal{M} \times T}}{\text{hard sphere diameter in A}^{o^2} \times \Omega_v} \\
&= \frac{26.69 \times \sqrt{18.015 \times 2935}}{2.641^2 \times 0.99} \\
&= 887.9\ \mu\text{P} \\
&= 8.879 \times 10^{-5}\ \text{N s m}^{-2}
\end{aligned}$$

Calculation for O_2

$$\begin{aligned}
\text{Molecular weight of } O_2,\ \mathcal{M}_{O_2} &= 32 \\
T^* &= \left(\frac{\text{Boltzman constant}}{\text{Charectiristic energy}}\right)_{H_2O} \times T \\
&= \left(\frac{1}{106.7}\right) \times 2935 \\
&= 27.5 \\
\text{Collision integral, } \Omega_v &= \frac{A}{T^{*B}} + \frac{C}{e^{DT^*}} + \frac{E}{e^{FT^*}} \\
&= \frac{1.16145}{T^{*0.14874}} + \frac{0.52487}{e^{0.7732\times T^*}} + \frac{2.16178}{e^{2.43787\times T^*}} \\
&= 0.709
\end{aligned}$$

$$
\begin{aligned}
\text{Viscosity, } \mu_{O_2} &= \frac{26.69 \times \sqrt{\mathcal{M} \times T}}{\text{hard sphere diameter in A}^{o^2} \times \Omega_v} \\
&= \frac{26.69 \times \sqrt{32 \times 2935}}{3.467^2 \times 0.709} \\
&= 959.23 \ \mu\text{P} \\
&= 9.59 \times 10^{-5} \text{ N s m}^{-2}
\end{aligned}
$$

Calculation for N_2

$$
\begin{aligned}
\text{Molecular weight of N}_2, \mathcal{M}_{N_2} &= 28.013 \\
T^* &= \left(\frac{\text{Boltzman constant}}{\text{Charectiristic energy}} \right)_{H_2O} \times T \\
&= \left(\frac{1}{71.4} \right) \times 2935 \\
&= 41.106 \\
\text{Collision integral, } \Omega_v &= \frac{A}{T^{*B}} + \frac{C}{e^{DT^*}} + \frac{E}{e^{FT^*}} \\
&= \frac{1.16145}{T^{*0.14874}} + \frac{0.52487}{e^{0.7732 \times T^*}} + \frac{2.16178}{e^{2.43787 \times T^*}} \\
&= 0.668 \\
\text{Viscosity, } \mu_{O_2} &= \frac{26.69 \times \sqrt{\mathcal{M} \times T}}{\text{hard sphere diameter in A}^{o^2} \times \Omega_v} \\
&= \frac{26.69 \times \sqrt{28.013 \times 2935}}{3.798^2 \times 0.668} \\
&= 793.92 \ \mu\text{P} \\
&= 7.94 \times 10^{-5} \text{ N s m}^{-2}
\end{aligned}
$$

Calculation of mixture viscosity

Mixture viscosity is calculated using the Wilke's approximation

Mole fractions of combustion products are calculated based on the combustion reaction shown above

$$
\begin{aligned}
y_{H_2O} &= 0.693 \\
y_{N_2} &= 0.231 \\
y_{O_2} &= 0.076
\end{aligned}
$$

$$
\text{Core gas viscosity,} \mu_m = \sum_{i=1}^{n} \frac{y_i \times \mu_i}{\sum_{j=1}^{n} y_i \times \varphi_{ij}}
$$

The parameter φ_{ij} is calculated based on Wilke's approximation.

$$\varphi_{ij} = \frac{\left[1 + \left(\frac{\mu_i}{\mu_j}\right)^{0.5} \left(\frac{\mathcal{M}_j}{\mathcal{M}_i}\right)^{0.25}\right]^2}{\left[8\left(1 + \mathcal{M}_i/\mathcal{M}_j\right)\right]^{0.5}}$$

$$\mu_m = 8.71 \times 10^{-5} \text{ N s m}^{-2}$$

B.2.2 Calculation of Prandtl number

Calculation for component gases

Thermal conductivities of individual gases are calculated using Stiel and Thodos correlations. The correlation is given below.

$$\frac{k \times \mathcal{M}}{\mu} = 1.15 \times c_v + 4.04 \left[k \text{ in cal cm}^{-1} \text{ s}^{-1} \text{ K}^{-1}, \mu \text{ in poise and c}_v \text{ in cal gmol}^{-1} \text{ K}^{-1}\right]$$

Calculation for H_2O

$$\begin{aligned} cp(T_g) \text{ of } H_2O &= 3087.05 \text{ J kg}^{-1} \text{ K}^{-1} \\ &= 13.28 \text{ cal gmol}^{-1} \text{ K}^{-1} \\ c_v &= c_p - R \\ &= 13.28 - (8.314/4.18) \\ &= 11.28 \text{ cal gmol}^{-1} \text{ K}^{-1} \\ \mu_{H_2O} &= 793.92 \ \mu\text{P} \\ k &= 0.00084 \text{ cal cm}^{-1} \text{ s}^{-1} \text{ K}^{-1} \\ &= 0.351 \text{ W m}^{-1} \text{ K}^{-1} \\ Pr &= \frac{\mu \times c_p}{k} \end{aligned}$$

$$\begin{aligned} &= \frac{887.7 \times 10^{-6} \times 3087.05}{0.351} \\ &= 0.78 \end{aligned}$$

Calculation for O_2

$$\begin{aligned} cp(T_g) \text{ of } O_2 &= 1241.644 \text{ J kg}^{-1} \text{ K}^{-1} \\ &= 9.5 \text{ cal gmol}^{-1} \text{ K}^{-1} \end{aligned}$$

$$
\begin{aligned}
c_v &= c_p - R \\
&= 9.5 - (8.314/4.18) \\
&= 7.51 \text{ cal gmol}^{-1} \text{ K}^{-1} \\
\mu_{O_2} &= 959.23 \ \mu\text{P} \\
k &= 0.00038 \text{ cal cm}^{-1} \text{ s}^{-1} \text{ K}^{-1} \\
&= 0.16 \text{ W m}^{-1} \text{ K}^{-1} \\
Pr &= \frac{\mu \times c_p}{k} \\
&= \frac{959.23 \times 10^{-6} \times 1241.644}{0.16} \\
&= 0.75
\end{aligned}
$$

Calculation for N_2

$$
\begin{aligned}
cp(T_g) \text{ of } N_2 &= 1319.69 \text{ J kg}^{-1} \text{ K}^{-1} \\
&= 8.875 \text{ cal gmol}^{-1} \text{ K}^{-1} \\
c_v &= c_p - R \\
&= 8.875 - (8.314/4.18) \\
&= 6.887 \text{ cal gmol}^{-1} \text{ K}^{-1} \\
\mu_{O_2} &= 793.92 \ \mu\text{P} \\
k &= 0.0003376 \text{ cal cm}^{-1} \text{ s}^{-1} \text{ K}^{-1} \\
&= 0.1412 \text{ W m}^{-1} \text{ K}^{-1} \\
Pr &= \frac{\mu \times c_p}{k} \\
&= \frac{793.92 \times 10^{-6} \times 1319.69}{0.1412} \\
&= 0.742
\end{aligned}
$$

Calculation for mixture

The individual values are weighted by the mass fractions of species to obtain mixture Prandtl number.

$$
\begin{aligned}
Pr_g &= \sum mf_i \times Pr_i \\
&= (0.584 \times 0.78) + (0.303 \times 0.75) + (0.113 \times 0.742) \\
&= 0.76
\end{aligned}
$$

B.2.3 Calculation of specific heat

Component gases : N_2, H_2O and O_2
Mass fractions of combustion products are calculated based on the combustion reaction shown

$$mf_{H_2O} = 0.584$$
$$mf_{N_2} = 0.303$$
$$mf_{O_2} = 0.113$$

c_p(T) of gases are calculated based on the equations of the nature

$$c_p/R = a + b \times T + c \times T^2 + d \times T^3 + e \times T^4$$

where a, b,c,d and e are equation coefficients.
The equation coefficients are

Species	a	b$\times 10^3$	c$\times 10^3$	d$\times 10^3$	e$\times 10^3$
H_2O	2.798	2.693	-0.5392	-0.01783	0.09027
N_2	2.469	2.467	-1.312	3.401	-0.3454
O_2	3.156	1.809	-1.052	3.190	-0.3629

$$c_p\,(T_g)\,of H_2O = 3087.05 \text{ J kg}^{-1} \text{ K}^{-1}$$
$$c_p\,(T_g)\,of N_2 = 1319.7 \text{ J kg}^{-1} \text{ K}^{-1}$$
$$c_p\,(T_g)\,of O_2 = 1241.6 \text{ J kg}^{-1} \text{ K}^{-1}$$

The specific heats are weighted by the mass fractions of species to obtain mixture specific heat.

$$\begin{aligned} c_{p_g} &= \sum mf_i \times c_{p_i} \\ &= (0.584 \times 3087.05) + (0.303 \times 1319.7) + (0.113 \times 1214.6) \\ &= 2342.83 \text{ J kg}^{-1} \text{ K}^{-1} \end{aligned}$$

B.3 Emissivity Calculations- Method by Leckner (1972)

The zero-partial-pressure emissivity is given by

$$\epsilon_0 \left(p_a L, p = 1 \text{ bar }, T_g\right) = exp\left[\sum_0^M \sum_0^N C_{ji} \left(\frac{T_g}{T_0}\right)^j \left(log_{10} \frac{p_a L}{(p_a L)_0}\right)^i\right]$$

where T_0 = 1000 K, ($p_a L_0$) = 1 bar cm and C_{ij}, correlation coeficients.
The emissivity for different pressure conditions is found from the following eqation.

$$\frac{\epsilon \left(p_a L, p, T_g\right)}{\epsilon_0 \left(p_a L, 1bar, T_g\right)} = 1 - \frac{(a-1)\left(1 - p_E\right)}{a + b - 1 + p_E} exp\left\{-c\left[log_{10} \frac{(p_a L)_m}{p_a L}\right]^2\right\}$$

where p_E is an effective pressure, a,b,c and $(paL)_m$ are correlation constants.
Since the mixture contains both carbon dioxide and water vapour, the bands partially overlap and another correction factor must be introduced. This correction factor is calculated as shown below.

$$\Delta\epsilon = \left[\frac{\xi}{10.7 + 101\xi} - 0.0089\xi^{10.4}\right]\left(log_{10} \frac{p_{H_2O} + p_{CO_2}}{(p_a L)_0}\right)^{2.76}$$
$$\text{where, } \xi = \frac{p_{H_2O}}{p_{H_2O} + p_{CO_2}}$$

The total emissivity of a mixture of gases containing CO2 and water vapour is

$$\epsilon_g = \epsilon_{H_2O} + \epsilon_{CO_2 -} - \Delta\epsilon$$

Correlation constants for the determination of the total emissivity of water vapour

	M,N			2,2	
C_{00}	.....	C_{N0}	-2.118	-1.1987	0.035596
.....	.....	.....	0.85667	0.93048	-0.14391
C_{0M}	.....	C_{NM}	-0.10838	-0.17156	0.045915

$$P_E = \left(p + 2.56\frac{p_a}{\sqrt{t}}\right)/p_0$$
$$\frac{(p_a L)_m}{(p_a L)_0} = 13.2 \times t^2$$

$$
\begin{aligned}
a &= 2.144, t < 0.75 \\
&= 1.88 - 2.053 \times \log_{10} t, t > 0.75 \\
b &= 1.10/t^{1.4} \\
c &= 0.5
\end{aligned}
$$

where T_0 = 1000 K, p_0 = 1 bar, t = T/T_0, $(p_aL)_0$ = 1 bar cm
Correlation constants for the determination of the total emissivity of carbon dioxide

	M,N			2,3		
C_{00}	.....	C_{N0}	-3.9893	2.7669	-2.1081	0.039163
.....	.....	.....	1.2710	-1.1090	1.0195	-0.21897
C_{0M}	.....	C_{NM}	-0.23678	0.19731	-0.19544	0.044644

$$
\begin{aligned}
P_E &= (p + 0.28 \times p_a)/p_0 \\
\frac{(p_aL)_m}{(p_aL)_0} &= 0.054/t^2, t < 0.7 \\
&= 0.255 \times t^2, t > 0.7 \\
a &= 1 + 0.1/t^{1.45} \\
b &= 0.23 \\
c &= 1.47
\end{aligned}
$$

where T_0 = 1000 K, p_0 = 1 bar, t = T/T_0, $(p_aL)_0$ = 1 bar cm
ϵ_g is calculated from the above equations and its value is 0.211.

B.4 Coolant Entrainment Calculations

Correlations proposed by Sawant et al. (2008) are used for calculating the entrainment fraction.

$$
\begin{aligned}
\text{Coolant Reynolds Number, } Re_c &= V_c \times D \times \rho_c/\mu_c \\
&= 3.96 \times 0.1016 \times 857/0.000129 \\
&= 2679365
\end{aligned}
$$

$$
\begin{aligned}
Re_{c,film} &= 250 \times \ln Re_c - 1265 \\
&= 250 \times \ln 267935 - 1265 \\
&= 2435.3 \\
E_m &= 1 - \frac{Re_{c,film}}{Re_c} \\
&= 1 - \frac{2435.3}{2679365} \\
&= 0.99 \\
a &= 2.31 \times 10^{-4} \times Re_c^{-0.35} \\
&= 1.3 \times 10^{-6}
\end{aligned}
$$

Surface tension of coolant, $\sigma_c = 0.0362$ N m^{-1}

$$
\begin{aligned}
We &= \frac{\rho_g \times V_g^2 \times D}{\sigma \left(\frac{\Delta\rho}{\rho_g}\right)^{0.25}} \\
&= \frac{1.55 \times 4^2 \times 0.1016}{0.0362 \left(\frac{857-1.55}{1.55}\right)^{0.25}} \\
&= 17954.7
\end{aligned}
$$

$$
\begin{aligned}
\text{Entrainment fraction, } E &= E_m \times tanh\left(a \times We^{1.25}\right) \times 100 \\
&= 0.99 \times tanh\left(1.3 \times 10^{-6} \times 17954.7^{1.25}\right) \times 100 \\
&= 26.3\%
\end{aligned}
$$

LIST OF PAPERS BASED ON THESIS

Papers in Refereed International Journals

1. **Shine, S. R.**, Sunil Kumar, S. and Suresh, B. N. (2012). Influence of coolant injector configuration on film cooling effectiveness for gaseous and liquid film coolants. ***Heat and Mass Transfer***, 48(5), 849-861.

2. **Shine, S. R.**, Sunil Kumar, S. and Suresh, B. N. (2012). Internal Wall-Jet Film Cooling with Straight Cylindrical Holes. ***AIAA Journal of Thermophysics and Heat Transfer***, 26(3), 439-449.

3. **Shine, S. R.**, Sunil Kumar, S. and Suresh, B. N. (2012). A new generalised model for liquid film cooling in rocket combustion chambers. ***International Journal of Heat and Mass Transfer***, 55, 5065-5075.

4. **Shine, S. R.**, Sunil Kumar, S. and Suresh, B. N. (2013). Internal wall-jet film cooling with compound angle cylindrical holes. ***Energy Conversion and Management***, 68, 54-62.

5. **Shine, S. R.**, Sunil Kumar, S. and Suresh, B. N. (2012). Properties of disturbance waves in liquid film cooling flows, ***Propulsion and Power Research***, Accepted for publication.

Presentations in Conferences

1. **Shine, S. R.**, Sunil Kumar, S. and Suresh, B. N. (2011). Analysis of film cooling performance of stream-wise injection with cylindrical holes, *Proceedings of the National conference on Space Transportation Systems: Opportunities and Challenges.* STS 2011, VSSC, Thiruvananthapuram, December 16-18, 2011.

2. **Shine, S. R.**, Sunil Kumar, S. and Suresh, B. N. (2012). Numerical investigation of gas-liquid interface characteristics in liquid film cooling flows, *ASME 2012 International Mechanical Engineering Congress & Exposition, IMECE2012*. Houston, Texas, USA, November 9-15, 2012. Paper accepted.

3. **Shine, S. R.**, Sunil Kumar, S. and Suresh, B. N. (2012). Internal wall-jet Film Cooling with Tangential Coolant Holes, *ASME 2012 Gas Turbine India Conference, GTIndia2012*. IIT, Mumbai, December, 1, 2012.